Cavitation-induced shear waves in soft solids

Dissertation

zur Erlangung des akademischen Grades

Doktoringenieur

(Dr.-Ing.)

von M. Sc. Saber Izak Ghasemian

geb. am 05.05.1991 in Ramsar

genehmigt durch die Fakultät für Electrotechnik und Informationstechnik

der Otto-von-Guericke-Universität Magdeburg

Gutachter:

Prof. Dr. rer. nat. Georg Rose

Prof. Dr. rer. nat. Claus-Dieter Ohl

Prof. Dr. Yoshiyuki Tagawa

Eingereicht am: 26.03.2025

Verteidigt am: 15.08.2025

Zusammenfassung

Kavitation spielt heute eine wichtige Rolle in verschiedenen medizinischen Anwendungen. Während die optische Hochgeschwindigkeitsbildgebung ein gängiges Werkzeug zur Untersuchung der Dynamik von Kavitationsblasen ist, stößt sie in biologischem Gewebe aufgrund eingeschränkter optischer Zugänglichkeit an ihre Grenzen. Diese Dissertation nutzt eine Hochbildraten-Plane-Wave-Ultraschalltechnik, die speziell darauf abgestimmt ist, die schnelle Dynamik von Kavitationsblasen in gewebeähnlichen Materialien zu erfassen und ein Echtzeit-Monitoring in biologischem Gewebe zu ermöglichen.

Ein weiterer bedeutender Beitrag dieser Arbeit ist die Untersuchung von kavitationsinduzierten Scherwellen in weichen Festkörpern. Es wird gezeigt, dass der nicht-sphärische Kollaps einer Kavitationsblase in einem weichen Material Scherwellen erzeugt, wobei die Wellenenergie und die Ausbreitungsrichtung erheblich von der Dynamik der Blase abhängen. Darüber hinaus wird demonstriert, dass das durch den Kollaps einer Kavitationsblase in ein weiches Material verursachte Jetting ebenfalls Scherwellen erzeugt, deren Energie von der Art des Jettings in das Material abhängt. Die Integration der Hochbildraten-Bildgebung der Blasendynamik mit der Erfassung von Scherwellen stellt einen vielversprechenden Ansatz für das Echtzeit-Monitoring thermischer Ablationsprozesse in biologischem Gewebe dar.

Darüber hinaus führt die Dissertation die kavitationsinduzierte Scherwellen-Rheometrie ein, eine neuartige Methode zur Bestimmung der elastischen Eigenschaften weicher Materialien. Durch die optische Verfolgung der durch Kavitation induzierten Scherwellenaus-

breitung bietet diese Technik einen minimalinvasiven Ansatz zur Untersuchung des Materialverhaltens. Die Methode zeigt vielversprechende Anwendungen in der Scherwellen-Elastographie und der Rheometrie und liefert wertvolle Erkenntnisse über die Elastizität und mechanischen Eigenschaften von Gewebe unter dynamischen Bedingungen.

Abstract

Cavitation plays an important role in various medical applications today. While optical high-speed imaging is a common tool for studying cavitation bubble dynamics, it faces challenges in biological tissues where optical access is limited. This thesis utilizes a high-frame-rate plane wave ultrasound technique, specifically tailored to capture the rapid dynamics of cavitation bubbles within tissue-mimicking materials, offering real-time monitoring potential in biological tissues.

Another significant contribution of this thesis is the investigation of cavitation-induced shear waves in soft solids. It shows that the non-spherical collapse of a cavitation bubble within a soft material generates shear waves, with significant differences in wave energy and propagation direction depending on the bubble dynamics. Additionally, it demonstrates that jetting caused by the collapse of a cavitation bubble into a soft solid also generates shear waves, where the energy of these waves is dependent on the type of jetting into the material. Integration of high-frame-rate imaging of bubble dynamics and shear wave capture presents a promising approach for real-time monitoring of thermal ablation processes in biological tissues.

Moreover, the thesis introduces cavitation induced shear wave rheometry, a novel method for assessing the elastic properties of soft materials. By optically tracking shear wave propagation induced by cavitation, this technique offers a minimally invasive approach to studying material behavior where the technique shows promise for applications in shear wave elastography and rheometry, providing valuable insights into tissue elasticity

and mechanical properties under dynamic conditions.

Contents

Zusammenfassung **iii**

Abstract **v**

Acknowledgments **vii**

List of Abbreviations **xiii**

1 Introduction **2**

1.1 Cavitation bubble formation 5

1.1.1 Laser-induced cavitation 5

1.2 The Rayleigh-Plesset equation 6

1.3 Cavitation in soft solids 7

1.4 Elastic waves in soft solids 9

1.5 Aims and objectives 12

1.6 Guide to this thesis 12

2 Ultrasound imaging of cavitation bubble dynamics **14**

2.1 Introduction 14

2.2 Conventional line-by-line ultrasound imaging 15

2.3 Plane wave ultrasound imaging 16

2.3.1 Plane wave compounding 18

2.4 Ultrasound beamforming 18

2.5 Experimental facility for ultrafast ultrasound imaging 21

2.6 Plane wave imaging of gas bubbles 25

2.7 Single plane wave imaging of transient cavitation bubbles 28

2.8 Cavitation bubble dynamics in water 29
2.9 Cavitation bubble dynamics in Gelatin 32
2.10 Conclusion 35

3 Shear wave by laser-induced cavitation bubble 38
3.1 Introduction 38
3.2 Experimental setup and methodology 39
3.2.1 Symmetry of shear wave generation 42
3.2.2 Assessing tracer particle behavior: following the shear 43
3.3 Bubble dynamics effect on shear wave generation 44
3.4 Shear origin 48
3.5 Shear wave propagation angle 52
3.6 Shear efficiency 52
3.7 Shear stress confinement 55
3.8 Conclusion 56

4 Ultrasound imaging of cavitation-induced shear waves 58
4.1 Introduction 58
4.2 Experimental setup and methodology: Shear wave generation from bubble collapse inside a soft solid 60
4.3 Shear wave visualization using graphite particles as trackers 61
4.4 Shear wave visualization using bubbles as trackers 64
4.5 Experimental setup and methodology: Shear wave generation from bubble jetting 68
4.6 Effect of different jets on shear wave propagation in soft solids 70
4.6.1 Shear wave generation from bullet jet 73
4.7 Conclusion 77

5 Cavitation Induced Shear Wave Rheometry 80
5.1 Introduction 80
5.2 Photoelastic imaging 81

5.2.1 The plane polariscope 82
5.2.2 The circular polariscope 82
5.3 Experimental Setup and Methodology 83
5.4 Shear waves induced by non-spherical collapse near a rigid boundary . . . 84
5.5 Conclusion 88

6 Conclusion and outlook **90**
6.1 Conclusions 90
6.2 Outlook and perspectives 92

References **94**

A Verasonics setup script for ultrafast ultrasound imaging **110**

List of Abbreviations

BLB Bulk Laser Bubbles. 68–70, 72, 73

CRT Cavitation Rheology Technique. 80

CSWR Cavitation-induced Shear Wave Rheometry. 81, 88, 89, 92, 93

DAS Delay And Sum. 19–21

DMAS Delay Multiply And Sum. 21, 27, 30

FFT Fast Fourier Transform. 42

HIFU High Intensity Focused Ultrasound. 9, 39, 93

IMR Inertial Microcavitation Rheometry. 8, 81

IQ In-phase and Quadrature. 59, 60

LPVI Local Phase Velocity-based Imaging. 88

PIV Particle Image Velocimetry. 13, 40–42, 46, 54, 61–63, 69, 70, 73, 74, 77, 81, 91

RF Radio Frequency. 29, 58–61

ROI Region Of Interest. 74, 77

SWE Shear Wave Elastography. 11, 38, 59

TBI Traumatic Brain Injury. 8

TMM Tissue Mimicking Material. 12, 13, 15, 32, 35, 56, 60, 81, 88, 91, 92

TMP Tissue Mimicking Phantom. 39, 40

USI Ultrasound Imaging. 58, 60, 61, 64, 65, 68–70, 74, 77

Chapter 1

Introduction

In fluid dynamics, bubbles—though appearing simple—exhibit complex and dynamic behaviors that have captivated scientists, engineers, and researchers across various fields. They come in different shapes and sizes, from ultra-small nanobubbles[1, 2] difficult to detect even with advanced imaging techniques, to large bubbles formed by the powerful forces beneath the oceans[3]. Whether they occur naturally or are intentionally generated in controlled environments, bubbles are central to numerous physical phenomena and understanding their dynamics and interactions with other bubbles and their surroundings is crucial for explaining a wide range of intriguing fluid behaviors.

One of these phenomena is boiling, where vapor bubbles form when the temperature rises above a certain value[4]. We have all seen them when we bring a pot of water to the boil. Another interesting phenomenon is cavitation, both of them are illustrated in the water phase diagram of Fig. 1.1. Boiling occurs when the liquid phase changes into the vapor phase due to a rise in temperature[4]. Conversely, cavitation occurs when the local liquid pressure falls below the vapor pressure and a phase transition from the liquid to the vapor phase takes place[5]. The latter is the main focus of this thesis.

The development of low-pressure regions within a liquid is a common phenomenon that occur in many different situations. A notable example happens in the fluid flow found in the Venturi nozzle that consist of a converging channel followed by a diverging

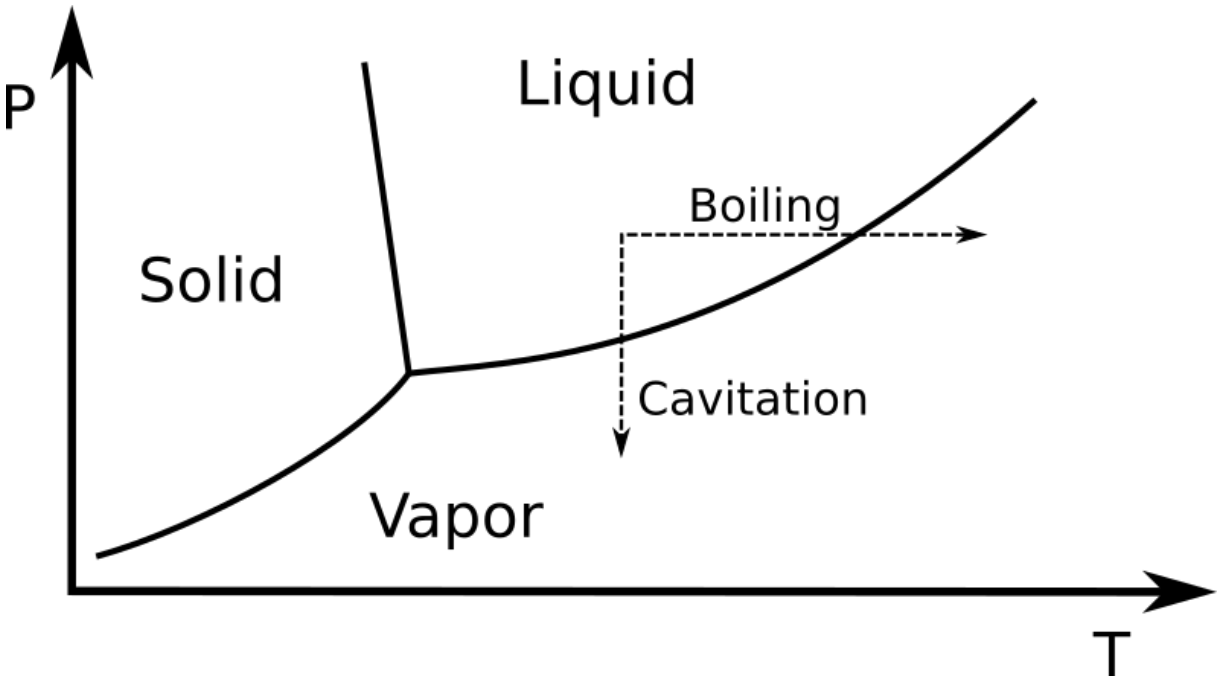

Figure 1.1: Water phase diagram for the phase transition in boiling and cavitation.

one. Due to mass conservation, the velocity is highest at the location where the cross-section is smallest. According to Bernoulli's equation, this specific location experiences the lowest pressure, thus may result in cavitation[6].

Another example where low pressures are found is the flow vortex[7], which are a very common flow structures. Due to their rotational dynamics and the resultant centrifugal forces, the pressure within the core of these structures reduces relative to the surrounding fluid, making them prone to cavitation in their core.

In addition to the aforementioned mechanisms of pressure reduction in fluid flows, another situation which can lead to formation of cavitation is during the negative pressure cycle of intense ultrasound irradiation [8, 9]. The phenomenon is known as acoustic cavitation, where the alternating low and high-pressure cycles create microscopic bubbles and compress them in the fluid[10], respectively.

Regardless of the mechanism that triggers cavitation, the subsequent dynamics of the cavitation bubble follow a common pattern[11]. After bubble formation due to a decrease in local fluid pressure, the bubble expands as the surrounding fluid pressure falls below the vapor pressure inside the bubble[11–13]. Inertia then causes the bubble to continue expanding beyond its equilibrium size, reaching a maximum volume. The bubble then

begins to shrink and collapses before rebounding[11–13].

The final stage of bubble shrinkage is termed collapse. The cavitation bubble collapse is associated with various phenomena that are based on the energy focusing, such as the generation of high-speed micro-jets[14] and the emission of strong pressure waves. If occurring sufficiently close to a boundary, these phenomena can potentially cause damage[15, 16] that poses a significant risk, particularly for rotating machinery such as ship propellers[17, 18], hydraulic turbines[19, 20] and pumps[21].

However, cavitation does not always lead to adverse effects. For example, and as outlined for the Venturi above, high pressure driven flow through nozzles in fuel injection systems are prone to cavitation that leads to a complex interplay of favorable and unfavorable results. While, cavitation is made responsible for erosion[22] and a reduction in the mass flow rate of the nozzle[23, 24], on the positive side, it plays a crucial role in facilitating primary jet breakup and fuel atomization[23, 25]. Here, cavitation, contributes significantly to improving combustion efficiency and reducing pollutant emissions.

There are numerous other examples where cavitation demonstrates its advantage: In the biomedical context, cavitation is important for kidney stone ablation and fragmentation[26]. There, single focused shock waves induce cavitation on the surface of the stone, assisting the break-up of renal stones. This extracorporeal shock wave lithotripsy named treatment method offers a non-invasive modality to the benefit of the patient. Moreover, in drug delivery[27], cavitation can enhance the permeability of cell membranes, facilitating the targeted uptake of therapeutic agents. Additionally, some of the needle-free injection systems use pressurized auto-injectors[28] based on cavitation to create a fine aerosol mist, enabling the efficient delivery of medications through the skin without the need for traditional needle-based methods. Also, emerging technologies like cavitation-based surface cleaning[29], micro-pumps in microfluidics[30], and water treatment[31] are some other applications, where cavitation has proven its benefits.

1.1 Cavitation bubble formation

While cavitation can naturally occur or be induced artificially in a liquid flow by creating adequate low-pressure regions, these mechanisms aren't always suitable for various engineering or research applications. Many situations demand a more controlled approach, requiring repeatable generation of a single bubble. To meet these specific requirements for precise control over size, time, and location, various techniques have been developed. For example, the discharge of underwater explosives generates relatively large bubbles[32] using electric currents to heat thin and submerged wires rapidly. Once the wires vaporize an explosively expanding cavitation bubble is formed [33]. Another commonly used technique is focused acoustic waves to generate acoustic cavitation[34]. There, ultrasound waves are utilized to expand pre-existing gaseous nuclei, or employing tensile waves to induce tension in the liquid, leading to the rupture and formation of bubbles[32].

1.1.1 Laser-induced cavitation

In contrast to conventional cavitation mechanisms driven by low-pressure regions within fluid flows, laser-induced cavitation offers a distinct and controlled approach to bubble formation. This technique, specially interesting for research applications, uses the energy deposition from short-duration pulsed lasers operating in the femto- to nanosecond range to generate well-controlled cavitation bubbles[35–37].

The process begins with the focused delivery of a high-intensity laser pulse to a specific focal volume. At these high laser intensities, the photon number density is sufficient to initiate multiphoton ionization within the liquid. The electric field of the laser induces an avalanche effect of initial free electrons, leading to the rapid amplification of the ionization events[38]. The resulting plasma, experiences a swift cooling phase after the laser pulse concludes. Following the cooling phase, the plasma recombines and the resulting high pressure, high temperature vapor explosively expands.

Laser-induced cavitation stands out from ultrasound-based methods by not only generating a shockwave during the bubble's collapse but also emitting a shockwave during bubble nucleation. Figure 1.2 shows an image sequence of a high-speed recording of a

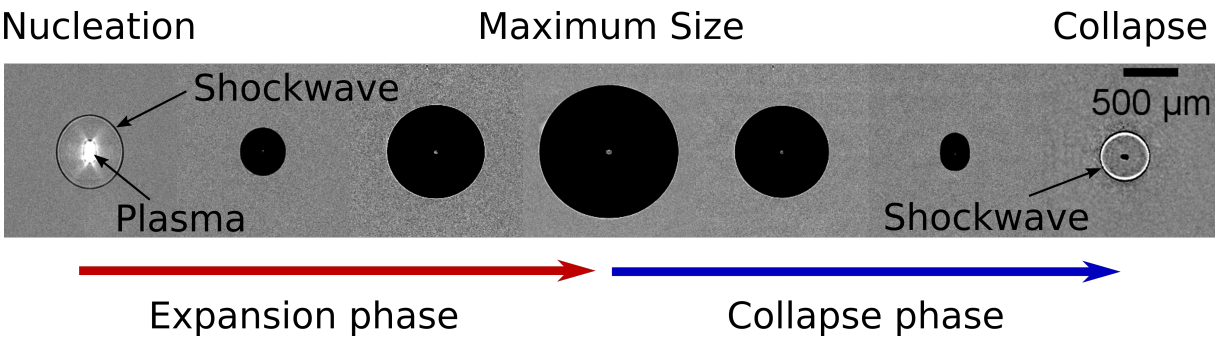

Figure 1.2: Selected frames from high-speed recording of the dynamics of a laser-induced cavitation bubble, generated after focusing a pulsed laser in water. The laser pulse propagates upward from below and the bright spot in the first frame shows the plasma region. A shockwave is emitted during bubble nucleation, a characteristics observed in certain types of cavitation such as explosion, spark, and laser-induced. The bubble expands to a maximum size and then collapses and rebounds again (not shown here). A shockwave is also emitted at collapse, which is characteristics of cavitation in general.

cavitation bubble from nucleation to the first collapse. The shockwaves emitted during both nucleation and collapse are visualized using shadowgraphy, which detects the density differences in the liquid caused by refractive index gradients induced by pressure changes[39].

Laser-induced cavitation offers a high repeatability and excellent control in time and space of single cavitation bubbles. By varying the laser energy, it is possible to precisely adjust the generated bubble size. Also, in the examination of cavitation bubble interactions with other dynamic elements, precise timing of bubble appearance becomes effortlessly achievable through a careful control of the laser timing. This capability is particularly advantageous when investigating the impact of cavitation on various dynamic phenomena, allowing for precise synchronization of bubble generation with specific events of interest.

1.2 The Rayleigh-Plesset equation

The spherical dynamics of a gas and vapor-filled bubble can be described with an ordinary differential equation. One of the commonly used equations is the Rayleigh-Plesset model, derived from the Navier-Stokes equation, see for example [13, 40]. The Rayleigh-Plesset model simplifies the intricate dynamics of a spherical gas bubble in an incompressible

liquid, providing a more accessible representation of the bubble's behavior. A common form of the Rayleigh-Plesset equation is indicated in Eq. 1.1:

$$R\ddot{R} + \frac{3}{2}\dot{R}^2 + \frac{p_\infty(t) - p_v}{\rho} + \frac{2\sigma}{\rho R} + 4\nu\frac{\dot{R}}{R} = 0 \quad , \tag{1.1}$$

Here R represents the bubble radius and $\dot{R}$ and $\ddot{R}$ denote its velocity and acceleration, respectively. ρ is the density of the liquid, p_v the vapor pressure inside the bubble, and $p_\infty(t)$ is the ambient time-dependent pressure acting as an external driving force. σ denotes the surface tension of the gas-liquid interface, and ν represents the kinematic viscosity of the liquid.

The Rayleigh-Plesset equation provides a rigorous mathematical framework for quantifying the radial dynamics of spherical gas bubbles within a liquid medium, explaining key aspects such as growth, collapse, and oscillations[6]. It has been widely utilized in numerical simulations to estimate the evolution of bubble radius over time, and serves as a fundamental tool for understanding cavitation phenomena across various disciplines, from the design of ultrasonic cleaning processes to biomedical ultrasound imaging and therapeutic applications. It is important to explicitly note that the equation is specifically applicable to spherical bubbles. In cases where bubbles are formed near a boundary and the bubbles deviate from spherical shape, the equation is not valid anymore.

1.3 Cavitation in soft solids

The investigation on cavitation has predominantly concentrated on cavitation occurring in Newtonian liquids - with particular emphasis on water - for a long time. Since Rayleigh's seminal work in 1917[41], which predicts that the maximum pressure occurring in a cavitating liquid is directly proportional to the far-field pressure, and inversely proportional to the size of the cavity, numerous researchers have explored cavitation phenomena in water across various flow conditions.

However, cavitation can occur in solids too. there, cavitation may occur within the solid structure itself or in liquid phases of the solid, like water within a hydrogel solution

or tissues[42]. Depending on the structural strength of the solid, the cavitation activities could lead to plastic deformation and damage to the solid[43]. For example, cavitation activities in the brain during sudden impacts on the skull can result in Traumatic Brain Injury (TBI)[44, 45]. Cavitation in solids has been documented and studied since the 1930s[46, 47]; nonetheless, this phenomena and its related damage mechanisms have received significantly less focus than cavitation in liquids[43].

Examining cavitation in soft solids holds significance not only due to its potential damage on material, but also because it offers a valuable tool for characterizing soft solids through a technique known as Inertial Microcavitation Rheometry (IMR)[48]. The essence of IMR lies in comparing experiments involving laser-induced inertial cavitation in a soft material, captured by a high-speed camera, with a theoretical-numerical cavitation model. Initially, a constitutive equation is selected, and subsequently, solutions from the cavitation model are adjusted to match the experimental data. This process enables the determination of important viscoelastic properties such as viscosity and shear modulus.[49]

To fit a constitutive equation on the experimental data, various models have been proposed. Initially, cavitation in tissue was modeled within the framework of a Maxwell-based viscoelastic fluid. This included both the Linear Maxwell model, representing the material as a series combination of a spring and a dashpot element, and the Nonlinear Oldroyd model, an extension incorporating nonlinear terms to better capture the intricate behavior of viscoelastic materials [50, 51]. Considering that soft tissue typically returns to its initial configuration after deformation, Kelvin-Voigt-based models such as Kelvin-Voigt [52] and Zener [53] were proposed. In the Kelvin-Voigt model, the material is represented as a parallel combination of spring and dashpot elements, allowing it to capture both the instantaneous elastic response and the time-dependent viscous response to applied stress. Conversely, in the Zener model, the material is represented by a series combination of spring and dashpot elements, each associated with a relaxation time characterizing the material's response to stress. This configuration enables the Zener model to more accurately capture the viscoelastic behavior of materials across a range of frequencies.

However, in biomedical applications where high-pressure amplitudes are employed, the

rapid and substantial oscillations of bubbles may give rise to considerable stress and strain rates. Consequently, it becomes important to consider the compressibility of the neighboring domain near the bubble and to account for nonlinear viscoelastic properties[54]. While the Kelvin-Voigt model addresses the compressibility of the domain[52], it falls short in considering nonlinear viscoelasticity. Gaudron *et al.*[54] addressed this limitation by developing a theoretical framework to model the dynamics of spherical bubbles formed directly in a viscoelastic medium. In their approach, they incorporated a viscoelastic model based on Kelvin–Voigt with nonlinear elasticity, utilizing common strain-energy functions such as neo-Hookean and Mooney–Rivlin. This integration enabled them to derive elastic forces acting on the bubble within Rayleigh–Plesset-like equations. Cohen and Molinari[55] also, provided analytical solutions for the expansion of a spherical void within a nonlinear viscoelastic medium. Other researchers have considered additional important factors in their work. Warnez and Johnsen[56] employed various equations to simulate single bubble dynamics in viscoelastic media with relaxation. Barajas and Johnsen[57] proposed a model that integrates the Kelvin–Voigt model and neo-Hookean formulation to describe bubbles in a viscoelastic medium, accounting for full thermal effects both inside and outside the bubble and Zilonova *et al.*[58] utilized a modified Gilmore-Akulichev model to investigate the bubble dynamics in soft tissue subjected to High Intensity Focused Ultrasound (HIFU).

1.4 Elastic waves in soft solids

The distinction between elastic solids, such as human tissues, and Newtonian fluids like water, is primarily rooted in their mechanical behavior, with elasticity playing a pivotal role. In the context of cavitation dynamics, this mechanical contrast results in differences in the behavior of cavitation bubbles within these materials. While Newtonian fluids exhibit fluid-like behavior, characterized by the absence of shear stress relaxation and the ability to flow under applied stress, elastic solids possess the capacity to deform reversibly under stress and return to their original shape upon stress removal[59]. Consequently, the constitutive models employed to describe cavitation phenomena in soft solids must

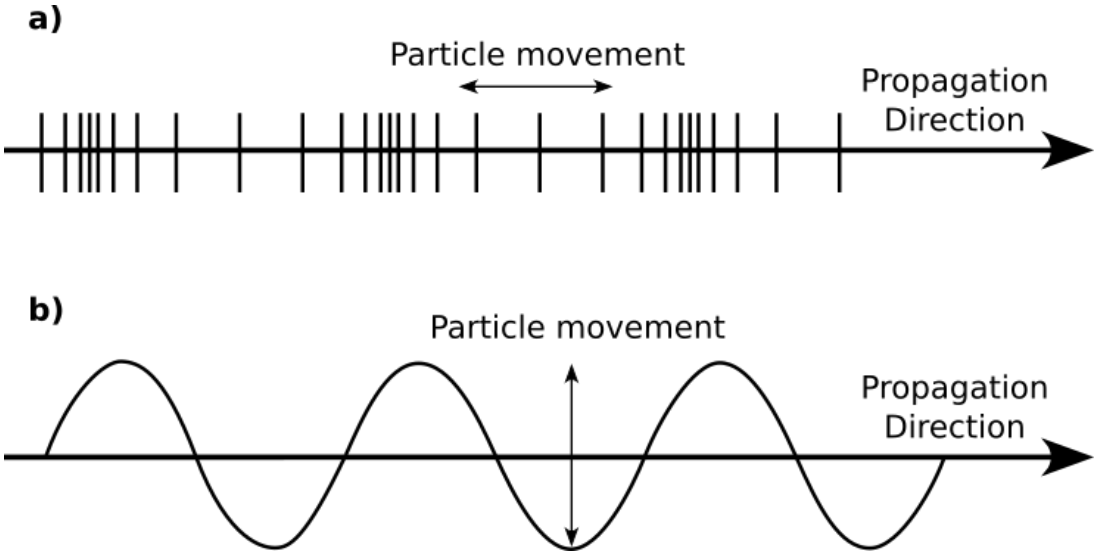

Figure 1.3: a) Schematic representation of longitudinal wave propagation. The direction of wave propagation aligns with the movement of particles. b) Schematic representation of transverse wave propagation, with the wave propagating perpendicular to the movement of particles.

incorporate additional elasticity forces acting on the bubble as described in Section 1.3.

Moreover, in addition to its role in influencing cavitation bubble dynamics, elasticity also manifests another crucial effect in soft solids: the ability to propagate elastic waves[60]. In Newtonian fluids like water, the propagation of waves is predominantly confined to longitudinal waves, which travel parallel to the direction of wave motion. However, in elastic materials like human tissues, elastic waves can propagate in both longitudinal and transverse directions[60]. Longitudinal waves consist of compressions and rarefactions of the medium in the direction of wave propagation, whereas transverse waves exhibit shearing motions that are perpendicular to the direction of wave propagation, as illustrated schematically in Fig 1.3.

The velocities of longitudinal (v_p) and transverse (v_s) waves in human tissue are significantly different. Longitudinal acoustic waves, for instance, propagate through tissue at a notably higher speed, typically around $v_p \approx 1500$m/s, whereas shear waves, representative of transverse motion, travel at slower velocities, typically ranging between 1m/s and 50 m/s in tissues [61].

Longitudinal acoustic waves, owing to their high propagation speed, are extensively utilized in medical ultrasound imaging where they provide detailed images of internal

body structures. These waves travel through tissues and reflect back to the ultrasound transducer, creating real-time visual representations of organs and blood flow. Despite its widespread use and advantages such as simplicity, affordability, and real-time imaging capabilities, conventional ultrasound imaging has limitations in assessing tissue mechanical properties, such as stiffness—a crucial factor in distinguishing between healthy and diseased tissues. To overcome this limitation, elastographic techniques have emerged as promising alternatives.

Elastography is a non-invasive imaging technique used to detect solid tumors, fibrosis, and cirrhosis related to chronic liver diseases, leveraging alterations in the viscoelastic properties of tissues due to particular pathological or physiological processes for diagnostic purposes[62]. The initiation of elastography in the early 1990s by Ophir *et al.* [63] signified the commencement of several qualitative and quantitative methodologies. These methodologies can be classified into four primary categories: Compression sonoelastography, transient elastography, tension elastography, and Shear Wave Elastography (SWE)[64]. The latter one, SWE, introduced by Sarvazyan *et al.* [65], have emerged as prominent quantitative techniques, garnering considerable attention. This technique involves initially generating a shear wave in the target tissue location, followed by measuring its propagation velocity. A spatial elasticity map of the tissue is then rebuilt using the established relationship between shear wave propagation velocity (V_s) and elasticity modulus (E) as described in Eq. 1.2:

$$E = 2\rho V_\mathrm{s}^2(1+\nu)\,. \tag{1.2}$$

Where ρ and ν represent mass density and Poisson's ratio, respectively [62]. The reconstructed elasticity maps provide quantitative insights into tissue stiffness variations and offer valuable diagnostic information, allowing clinicians to identify abnormalities in tissues. SWE techniques offer several advantages over traditional elastographic methods by providing real-time, quantitative assessments of tissue elasticity, enhancing diagnostic accuracy and enabling early detection of pathological changes. Additionally, these techniques are non-invasive, posing minimal risk to patients and reducing the need for invasive

procedures such as biopsies.

1.5 Aims and objectives

In this thesis, we pursue two main objectives to deepen our understanding of cavitation in tissues. The first objective involves employing high-frame-rate ultrasound imaging to study cavitation dynamics in soft materials. Traditional studies of cavitation bubble dynamics often rely on high-speed optical imaging, which faces limitations when applied to bubbles within tissues due to restricted optical access. To address this challenge, we develop an ultrasound technique based on plane wave ultrasound imaging, demonstrating its effectiveness in capturing bubble dynamics in a Tissue Mimicking Material (TMM).

The second objective aims to explore the generation of shear waves resulting from the non-spherical collapse of cavitation bubbles within a soft solid and near a solid wall. Emphasizing the importance of jetting in this process, our study seeks to establish a connection between the bubble dynamics and the resulting shear wave. This investigation contributes to our understanding of the impact of bubble distance to a solid wall on shear wave energy and propagation direction. Initially, to comprehend the physics of shear wave generation and propagation, we employ an optical method. Subsequently, we demonstrate the applicability of ultrasound imaging in tracking the generated shear waves, facilitating their observation in non-transparent media such as tissues. Additionally, we introduce a novel rheometry technique that utilizes the local propagation speed of the generated shear waves to construct an elasticity map of the medium.

1.6 Guide to this thesis

Chapter 2 presents the ultrasound imaging of cavitation phenomena both in water, and a TMM. There, we develop an ultra-fast ultrasound technique using plane wave imaging to capture fast cavitation bubble dynamics. An experimental setup is developed that combines high-speed optical and ultrasound imaging to capture bubble dynamics at sufficient frame rates simultaneously. We also discuss the potential and limits of our

proposed method.

In **Chapter 3**, we investigate shear wave generation from non-spherical bubble collapse in a TMM in vicinity of a solid wall. Connecting the distance of bubble from the solid wall with the bubble dynamics, we demonstrate the importance of jetting for shear wave generation. Specifically, we show that the stand-off distance affects the shear wave energy and propagation direction drastically. In this chapter we use a Particle Image Velocimetry (PIV) technique to visualize shear wave propagation.

Chapter 4 further investigates shear wave propagation using ultrasound techniques. Initially, we generated shear waves through the non-spherical collapse of cavitation bubbles within a soft solid. By utilizing both optical and ultrasound imaging, we effectively capture the shear wave dynamics. We then explore shear wave generation through bubble jetting, extending our study to include liquid jets impacting a TMM. Comparative analysis reveals that stronger jets, which penetrate deeper into the gelatin, produce higher amplitude shear waves and altered wavefront shapes.

Chapter 5 presents a new rheometry technique using shear wave generation from cavitation bubbles. There, the local propagation speed of the generated shear wave from non-spherical collapse of cavitation bubble is measured, from whom the elasticity map of the medium is build. We show that this technique can be used as a robust rheometry technique.

Chapter 6 summarizes the key findings of this thesis and discusses their implications for future research and practical applications. Additionally, we outline the limitations encountered during our research and propose future directions to overcome these challenges.

Chapter 2

Ultrasound imaging of cavitation bubble dynamics

The work presented in this chapter has been published in parts in S. Izak Ghasemian, F. Reuter, and C. D. Ohl, "High-speed ultrasound imaging of laser-induced cavitation bubbles," Applied Physics Letters, vol. 119, no. 11, p. 114101, 2021, see Ref. [66]. There I was the lead author. My contribution to the publication was conducting the experiments, performing the data analysis, and drafting the manuscript.

2.1 Introduction

Cavitation-based therapies have gained significant importance in various medical applications, including the opening of the blood-brain barriers for targeted drug delivery[67], breaking down kidney stones through kidney lithotripsy[68], and liquefying benign and malignant tissues using histotripsy techniques[69, 70]. The precise manipulation of cavitation dynamics in these applications minimizes damage to surrounding healthy tissues. However, controlling these dynamics through exposure parameters to enhance precision necessitates monitoring of bubble activity.

Traditionally, bubble dynamics in water or transparent TMMs are observed using optical methods. However, when it comes to studying bubbles within real biological tissues, optical recording poses significant challenges due to limitations in wavelength and imaging depth, and in many cases obtaining optical access is even unfeasible[71]. There, the monitoring of bubble activities is usually accomplished by assessing tissue echogenicity using conventional line-by-line B-mode ultrasound imaging.

However, there is still some limitations. While this method provides insights into the presence of residual bubbles, it falls short in capturing the dynamic aspects of bubbles, such as their maximum radius and after-bounce behavior due to the low frame rate of the traditional ultrasound imaging methods. This deficiency in imaging capabilities has served as the driving force behind our research presented in this chapter, motivating us to record the oscillations of individual bubbles within a TMM using a high frame rate ultrasound technique.

2.2 Conventional line-by-line ultrasound imaging

In Conventional line-by-line B-mode ultrasound imaging as shown in Fig. 2.1, the medium is subjected to ultrasound by employing a sequence of focused beams, and the resultant image is constructed by juxtaposing each scanning line. Neglecting any processing time considerations for image reconstruction or quality enhancement, this method enables the acquisition of a single frame after the transducer channels sequentially transmit the beams and receive the reflected echoes for reconstructing a line of the image. Therefore, the time requested to produce an entire image frame with N_{lines} scan lines is[72]:

$$T_{\text{frame}} = \frac{2\,z\,N_{\text{lines}}}{c}\,. \tag{2.1}$$

Where N_{lines} is the number of scan lines, z is the maximum imaging depth and c is the speed of sound in the medium. The limitation of this approach is quite obvious in reaching high frame rate ultrasound imaging. The ultrasound wave in this technique needs to scan the medium for N_{lines} times which takes relatively long time. For example for an imaging

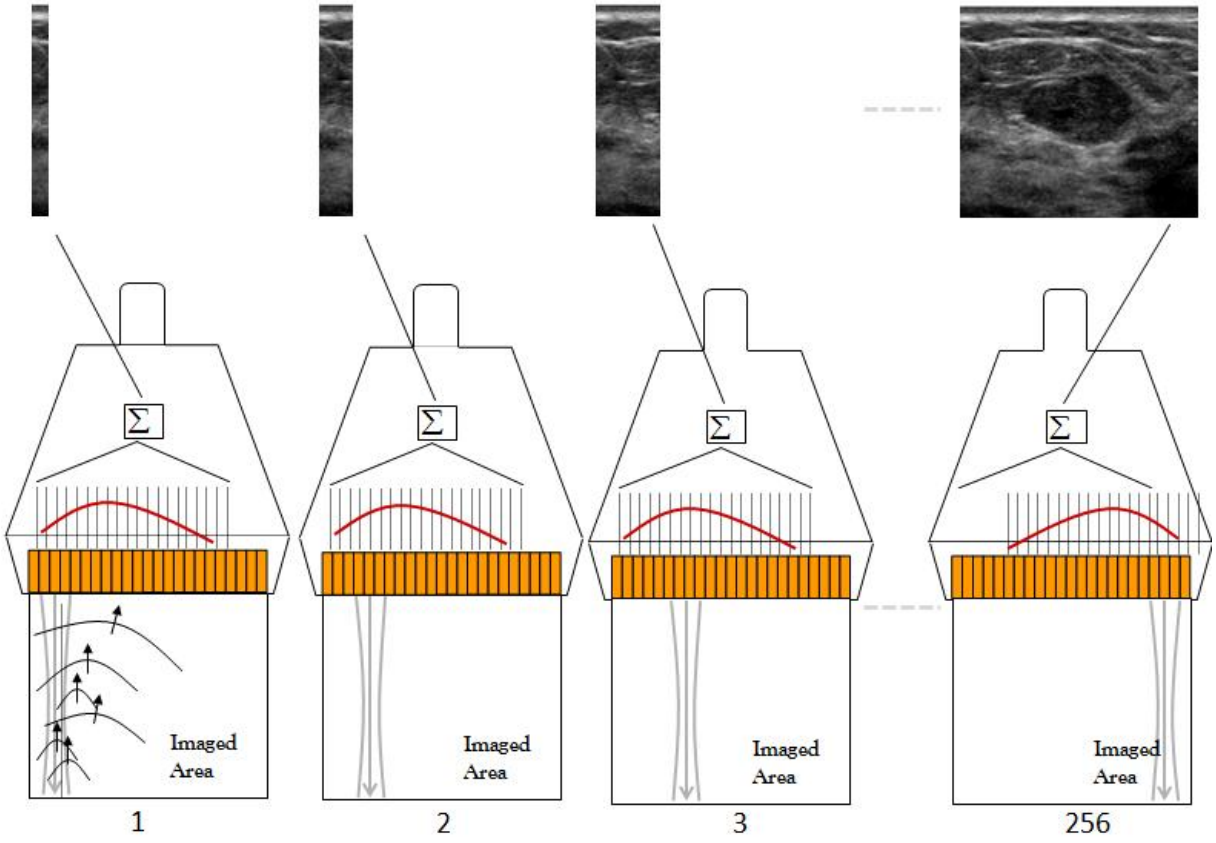

Figure 2.1: Conventional line-by-line ultrasound imaging, which involves sending a focused ultrasound beam into the imaging medium and receiving back echoes to form a line of image, adopted from Ref.[72]. The time it takes for the echoes to return is used to determine the distance to the scatterers in the domain. To create a complete 2D image, this process is repeated line-by-line, scanning across the area of interest in a systematic manner. Each line is reconstructed individually, and all the lines are then stitched together to form the full 2D image.

depth of $z = 5$cm with $N = 256$ lines in width, the maximum achievable frame rate is 60 Hz. These frame rates are too low in some applications where the quality of the resultant images are impaired by time constraints. The longer it takes to reconstruct an image, the more motion artifacts occur. In our case, where we want to capture the fast dynamics of cavitation bubbles, this is even more crucial, and much faster acquisition times are necessary.

2.3 Plane wave ultrasound imaging

To address the inherent limitation of low imaging frame rate of the conventional line-by-line ultrasound imaging, plane wave imaging was proposed[65]. As shown in Fig. 2.2,

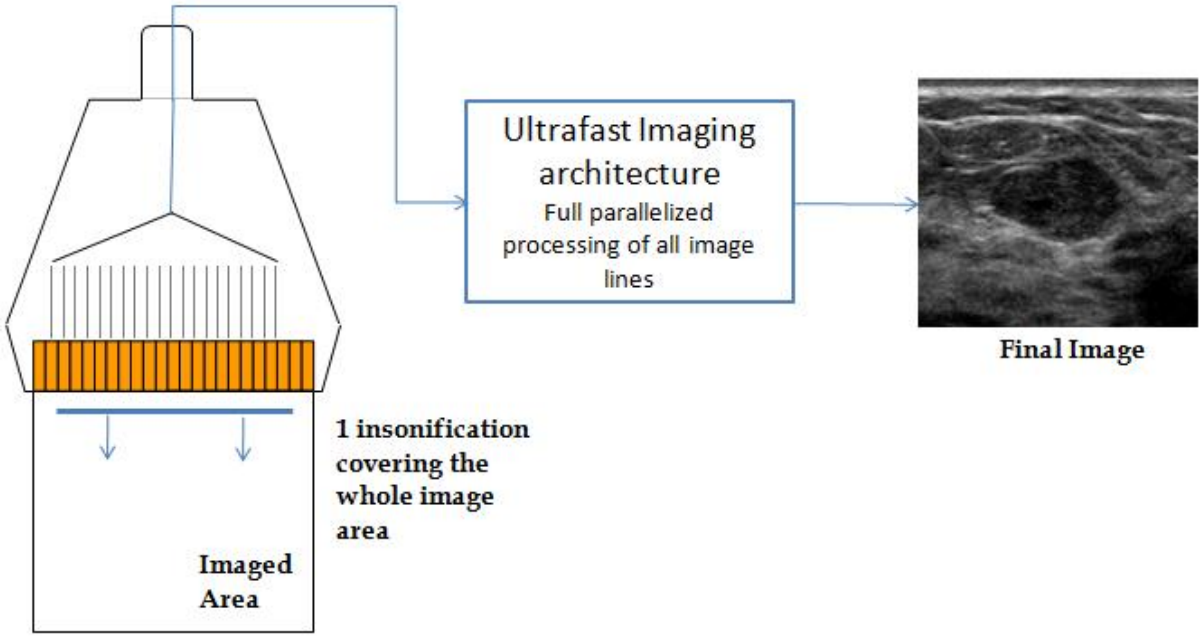

Figure 2.2: Single plane wave ultrasound imaging where multiple elements of an ultrasound transducer emit ultrasound waves simultaneously, effectively creating a plane of ultrasound energy that rapidly covers a wide area of the imaging region, adopted from Ref.[72]. The echoes from this plane are then received and processed simultaneously, allowing for the fastest possible ultrasound image acquisition, significantly improving the imaging frame rate.

instead of scanning the medium line by line, this approach allows multiple channels to transmit ultrasound waves simultaneously, creating unfocused plane waves[65, 72]. With this approach, the entire image area can be captured in the same timeframe required for only a single line scan and single plane wave imaging can reach to the maximum possible frame rate of ultrasound imaging which is only limited by imaging depth and speed of sound in the medium.

Nonetheless, like any engineering challenge, there is a trade-off: when one aspect improves, another inevitably degrades. In this case, using single plane wave imaging allows the frame rate to increase by several hundred times compared to traditional ultrasound techniques. However, the quality of individual images decreases in terms of spatial resolution and contrast[73], as the ultrasound energy is not focused on different lines of the image using an unfocused plane wave transmission. To restore the typical imaging quality found in conventional line-by-line imaging, Montaldo *et al.* introduced plane wave compounding to enhance the beamforming process by virtually establishing a focus[73].

2.3.1 Plane wave compounding

Plane wave compounding operates in a manner similar to the averaging techniques used in signal processing for noise reduction. The concept involves scanning the medium multiple times with plane waves, each time from different angles, with the aim of altering the speckle pattern on each scan as shown in Fig. 2.3. Afterwards, the resulting images are combined through averaging[74]. Objects that are consistently observed in multiple images are more likely to correspond to actual structures in the medium, while those that rarely appear across the images are likely noise components. Consequently, by summing the images, the real scatterers are enhanced, while the noise is suppressed. Increasing the number of angles in general increases the image quality. Studies have demonstrated that utilizing plane wave compounding with a sufficient number of angles can achieve image quality comparable to traditional line-by-line imaging in terms of contrast and signal to noise ratio[75], all while delivering a significantly higher frame rate compared to line-by-line imaging. This makes it suitable for capturing rapid dynamic events. However, it is important to note that in contrast to single plane wave, the imaging frame rate is reduced in proportion to the number of angles employed.

In all the ultrasound imaging techniques, such as conventional line-by-line, single plane wave, and plane wave compounding imaging, the received ultrasound signal undergoes further processing for the reconstruction of ultrasound images. The central element common to all these methods is ultrasound beamforming, a critical step that will be explored in the subsequent section.

2.4 Ultrasound beamforming

Beamforming is a signal processing technique where ultrasound signals received by transducer elements are combined and phased to generate a focused and coherent ultrasound beam. This process is fundamental for achieving high-resolution and detailed ultrasound images[76]. To create a focused and detailed image, beamforming involves delaying the signals received by each element of the transducer array based on the time it takes for the

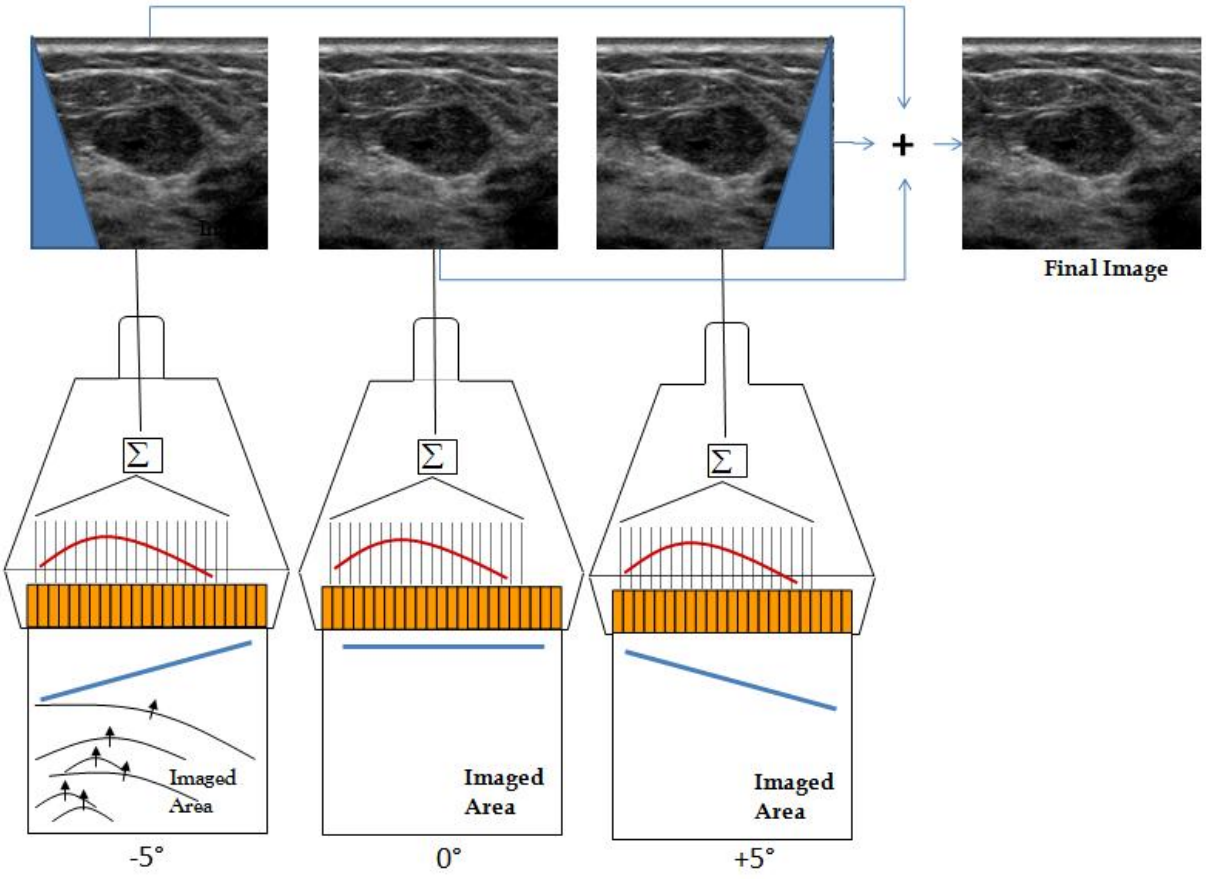

Figure 2.3: Plane wave compounding which involves transmitting multiple ultrasound beams in planes with different angles, allowing for a wide and comprehensive view of the target tissue, adopted from Ref.[72]. By then compounding or combining the echoes received from these multiple angles, a single high-quality image with reduced speckle noise and improved image quality is generated. This technique has the advantage of significantly enhancing image resolution and contrast compared to the single plane wave technique, while maintaining high frame rates.

echoes to reach to each element. As shown in Fig. 2.4, by precisely adjusting the timing of these signals, beamforming concentrates the ultrasound energy, enhancing spatial resolution and allowing the system to differentiate between structures at different depths[77]. Various beamforming algorithms are employed in ultrasound imaging, each with its own advantages and disadvantages.

The Delay And Sum (DAS) method stands as the most conventional approach and serves as the foundational technique in ultrasound beamforming[78]. It involves adjusting specific time delays for signals received from each element of the transducer array, which are then summed to create a focused beam with a predefined apodization weight for each element. Apodization refers to the technique of varying the amplitude of the signals from

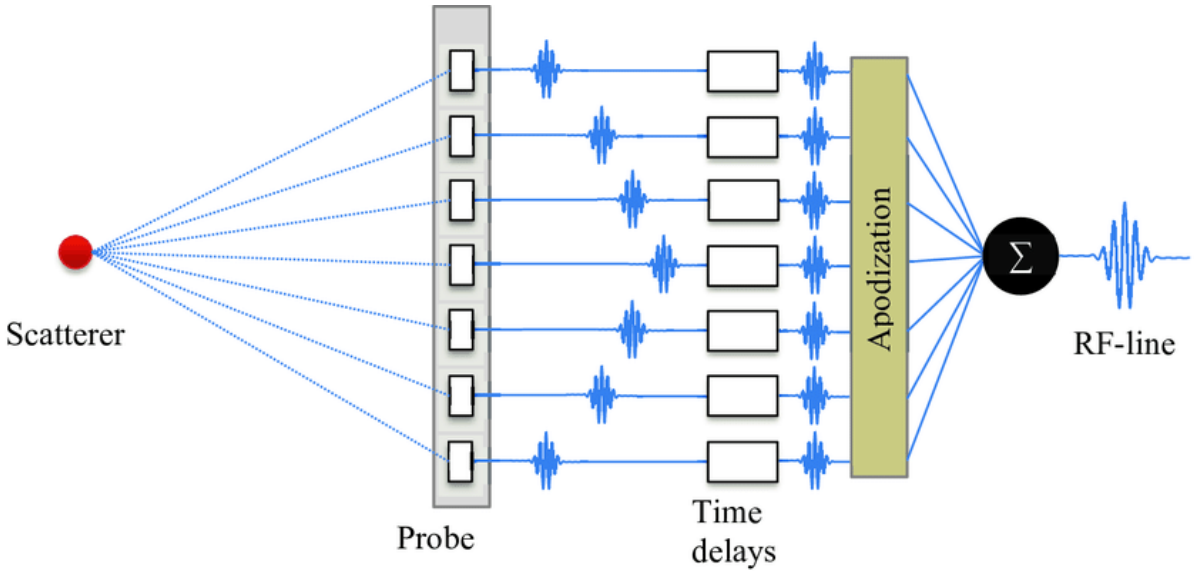

Figure 2.4: Beamforming: Enhancing ultrasound imaging clarity by focusing acoustic waves. The signals received by different elements of the transducer are aligned through precise time delays. These aligned signals are then combined, with each channel weighted by specific apodization factors.

individual transducer elements to control the shape and directionality of the ultrasound beam. By applying different weights to each element, apodization helps to reduce side lobes and grating lobes, thereby enhancing the spatial resolution and overall image quality. While DAS beamforming produces good image quality, it can still be limited by issues such as grating lobes and side lobes, which can reduce spatial resolution[79].

Adaptive beamforming is another approach designed to improve image quality, particularly in terms of contrast and signal-to-noise ratio by dynamically adjusting the apodization weights and phases of the signals received by individual elements in an ultrasound transducer array[80–82]. This is in contrast to traditional DAS beamforming, which applies fixed weight factors and delays to the received signals and then sums them to form an image. In DAS beamforming, all the signals received by the transducer elements are combined with fixed delays, which are based on the assumed speed of sound in the tissue. However, the actual speed of sound can vary within the body, leading to suboptimal image quality. Adaptive beamforming addresses this limitation by continuously adjusting the delays and weights of the signals based on the characteristics of the received data[83, 84]. This adaptability allows the system to better account for variations in tissue properties and improve image quality in challenging conditions.

Another successful beamforming technique is Delay Multiply And Sum (DMAS), which combines traditional DAS with a crucial multiplication step[79, 85]. Following time delaying of the received signals, the aligned signals are multiplied together to highlight strong echoes and to reduce the effect of incoherent noise and artifacts. This process ultimately produces ultrasound images with higher contrast and improved tissue differentiation, making DMAS a valuable tool for enhancing visualization and aiding in the detection of subtle structures within the imaging medium.

2.5 Experimental facility for ultrafast ultrasound imaging

All ultrasound recordings in this thesis were conducted utilizing a Verasonics research system (Vantage 64LE; Verasonics, Kirkland, WA, USA), equipped with 128 transmit channels and 64 receive channels, linked to a 5-MHz linear probe (ATL L7–4; Philips, Amsterdam, The Netherlands). Verasonics has been extensively utilized by research laboratories for ultrasonic research. The system is well-matched with a variety of Philips transducers and it offers substantial flexibility in designing sequences for ultrasound experiments. Additionally, it provides direct access to the unprocessed channel data from each element of the transducer array, along with software capabilities for beamforming and generating ultrasound images. To have the highest possible frame rate with Verasonics, the recordings is done in a so-called super-frame. To have a clear view on super-frame concept in Verasonics, it is necessary to have a better understanding of the Verasonics hardware first.

The Verasonics Vantage Research System, illustrated schematically in Fig. 2.5, comprises two primary components: the Verasonics data acquisition hardware, which includes electronic modules for functions such as multi-channel transmit waveform generation, analog receive signal amplification and filtering, digital signal processing, and scan sequencing; and the host controller computer, which operates software modules within the Matlab programming environment. These software modules enable users to program and execute

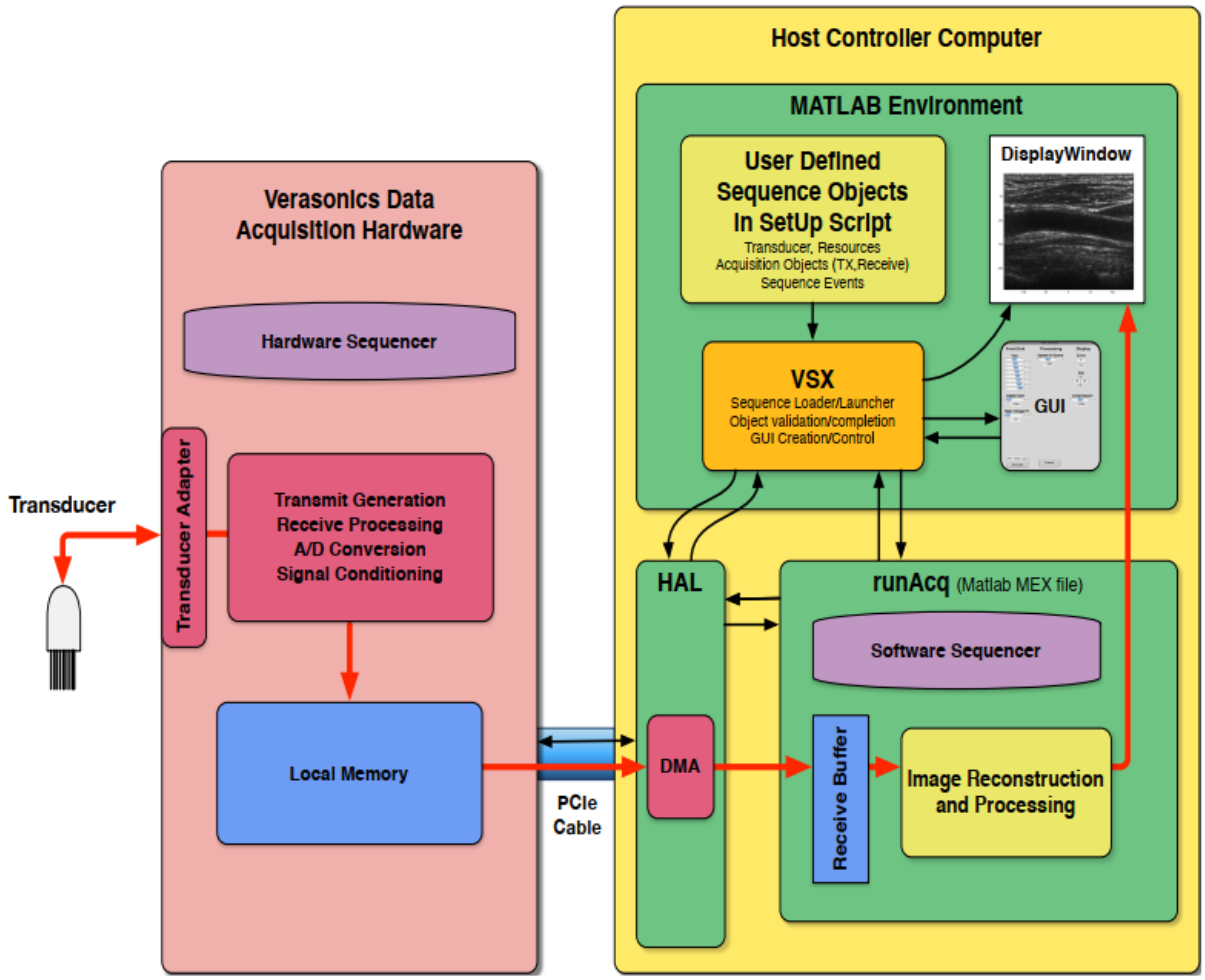

Figure 2.5: Streamlined system architecture of the Verasonics Research System: The flow of ultrasound data is indicated by the bold red line starting with the transducer and ending with the display, adopted from Ref.[86] with permission.

sequences of actions, referred to as *events*, in both the hardware and software domains. To create a sequence of events, users write a Matlab script known as a *Setup script*, which generates a set of objects loadable into the system. These objects are defined using Matlab structures that specify various attributes. Upon execution of the setup script, it generates a binary data file containing all the object structures and programming information, stored in the format of a Matlab *.mat* file. This *.mat* file can be subsequently loaded into the system using a dedicated loader program, named *VSX* (short for Verasonics Script eXecution), which operates as a standard script within the Matlab environment. This loader program communicates with the hardware via a Hardware Abstraction Layer (*HAL*) and conducts checks on the structures extracted from the *.mat* file. A typical Matlab setup script contains different elements. Some of the most important ones include

Transducer Specification, Transmit Specifications, Receive Specifications, Sequence Control Specifications and Sequence Event Specifications. To describe the super-frame used in this thesis, in the following, the sequence event specification will be discussed in more details.

The sequence of events required to acquire one or more frames of ultrasound data are outlined through a set of Event Objects. Typically, these Event Objects are the final structures specified in a Setup file. However, to define the objects used by these Events, it is necessary to have a predefined plan of actions.

Event structures define actions that typically execute in a sequential manner. The initial action is typically an acquisition, which involves a transmit operation followed by a receive period. Subsequently, the reconstruction action can process the newly acquired data to generate an output, and the process action can operate on the reconstructed output. While it is often useful to combine multiple actions within the same event, it's not mandatory. For instance, one can perform acquisitions without involving any reconstructions or processing. It is important to note that an event can also be a transmit-only event, with no receive specified, but a receive action must always be accompanied by a transmit reference.

In a typical frame within the Verasonics system, there is a transmit event followed by a receive event. Afterward, the received data is transferred from the local memory in the hardware to the host computer, and the image is reconstructed. One challenge here is that the data transfer to the host computer takes some time, which reduces the imaging frame rate.

However, there is an alternative approach where, instead of transferring the acquired data to the host computer after each frame, a concept called a "super-frame" is employed. Immediately after receiving data for the first transmit, the second ultrasound wave is sent, and the echo data for the second frame is acquired within the same super-frame. This process is repeated for all subsequent frames. As a result, all the received data for multiple frames is stored within a single super-frame, which can be transferred to the host computer once all data acquisition is complete.

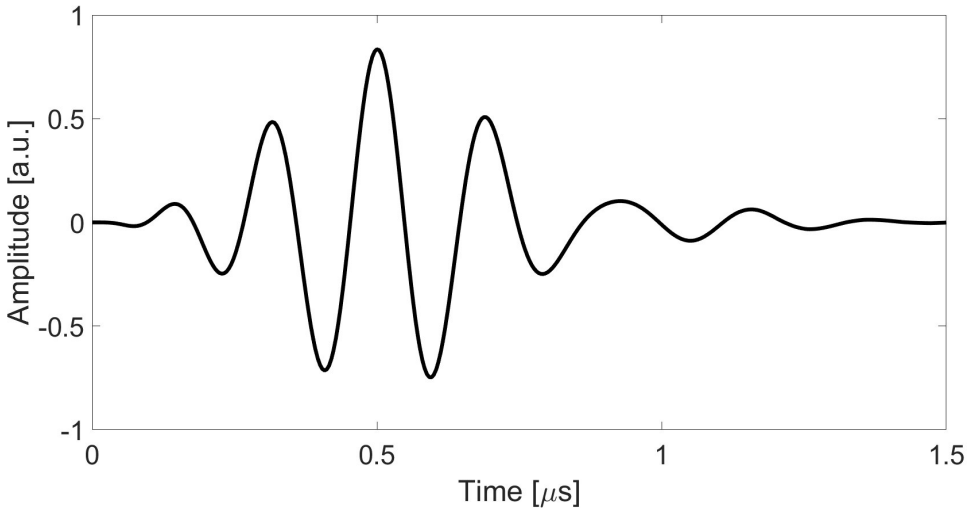

Figure 2.6: Transmit waveform used in all 128 transmit channels, with a center frequency of 5MHz.

It's worth noting that the data in the super-frame cannot be used directly for image reconstruction and the data needs to be separated into individual frames. This separated frames can then be used in Verasonics' offline mode for image reconstruction or with a custom algorithm offline. The full setup script employed in this experiment is available in Appendix A.

While the Verasonics system hardware can generate arbitrary transmit waveforms, here we use a simple *parametric* transmit waveform with four parameters. The first parameter is the frequency of the transmit pulse which was set as 5 MHz. The next parameter is the amount of time that the transmit drivers are active in the half cycle period, which was set as 0.67 to generate a digital drive waveform that approximates a sine wave. This parameter can take the values between 0.1 and 1.0 to control the amount of power delivered by a transmitter. The third parameter denotes the number of half cycles in the transmit waveform, which is configured to 2, resulting in a single cycle burst. The final parameter denotes the initial polarity of the first half cycle, with a value of 1 representing a positive polarity utilized in this thesis. Detailed information about the other methods to generate transmit waveforms is available in Verasonics sequence programming manual[86]. The transmit waveform used in this work is shown in Fig. 2.6.

2.6 Plane wave imaging of gas bubbles

This chapter primarily delves into capturing cavitation bubble dynamics through plane wave ultrasound imaging. Before we use the technique for observing fast dynamics of cavitation bubbles, we set a test experiment to investigate the image quality achieved through compounding plane waves with different number of angles. This investigation is important due to the fact that wave compounding results in higher image quality in expense of reducing the effective frame rate[66] as described in Subsection 2.3. As capturing fast dynamics of cavitation bubble is the main goal here, having high-frame rate imaging is crucial and compounding should be essentially limited or even avoided if possible. All the recording in this work has been done using a super-frame concept as discussed previously in Subsection 2.5.

For the test experiment, gas bubbles are generated by introducing air through a submerged needle. The generated bubbles then rise due to buoyancy in the cuvette, covering a distance of approximately 50 mm until they reach the free surface, as illustrated in Fig. 2.7. This method ensures the generation of stable and observable gas bubbles, which are integral to the study. The custom-made cuvette incorporates an acoustically transparent window on one of its lateral sides, to which the ultrasound imaging probe is affixed, while glass windows on the remaining sides allow for optical imaging from a lateral perspective. For the acoustically transparent window, we use a low density polyethylene film.

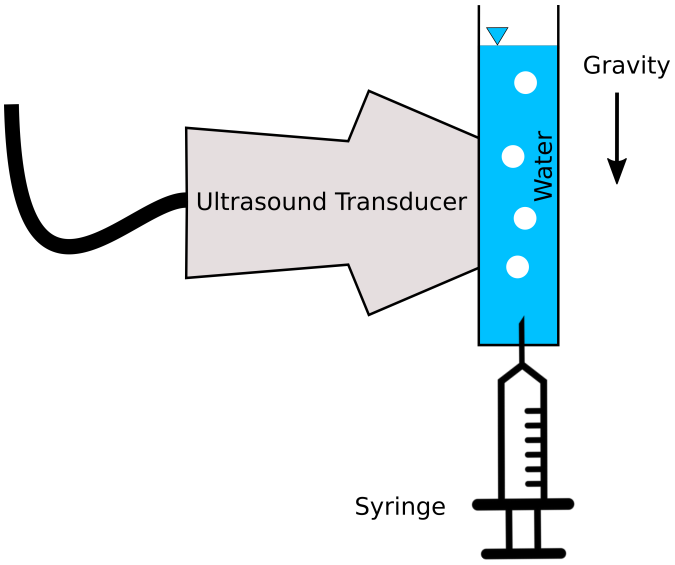

Figure 2.7: Experimental setup for imaging ascending bubbles in water using the ultrasound plane wave technique, with a maximum imaging depth of 12mm. The bubbles are generated through a submerged needle. The ultrasound transducer, connected to a Verasonics system is attached to the cuvette from the left side.

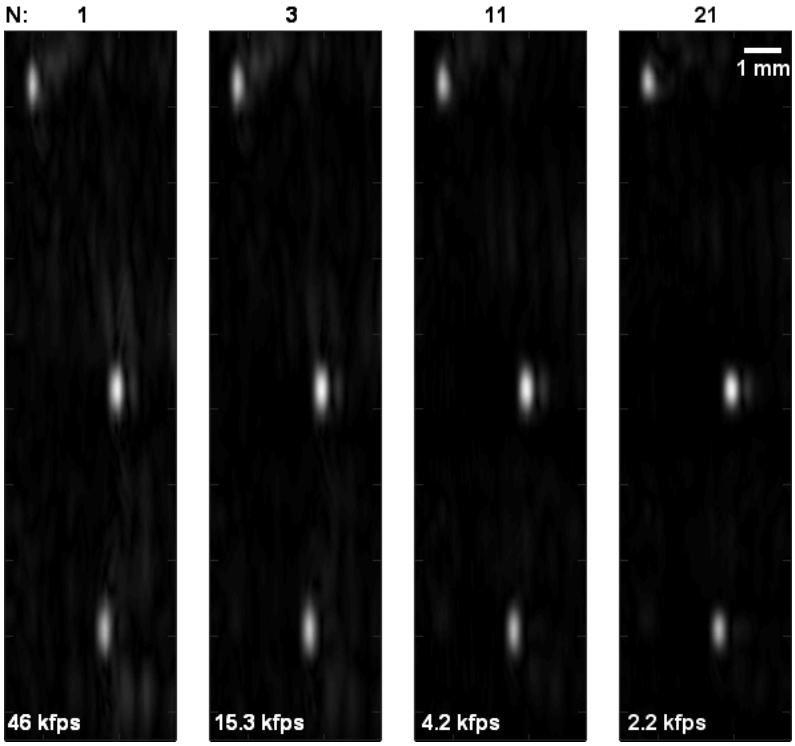

Figure 2.8: A qualitative assessment of single plane wave imaging versus plane wave compounding for visualizing a bubble column in water, using various numbers of tilted angles. The variable N represents the total number of plane waves employed in the compounding process. The imaging frame rate is written for each case, showing a reduction in the frame rates proportional to the number of compounding waves, reprinted with permission from Ref.[66]. The ultrasound transducer comes from the left side of the images.

Figure 2.8 presents a comparison of images acquired by employing an increasing number, denoted as N, of compound waves for reconstructing data obtained at depths ranging from 3 mm to 7.5 mm. The images are reconstructed using DMAS as described in Subsection 2.4. Imaging frame rate is written under each case. The experiment is carried out in a single continuous session, involving 21 distinct tilt angles ranging from $-10°$ to $+10°$. However, in the first three images only $N = 1, 3, 11$ angles are used to process the compound images. For the case where $N = 1$, a single plane wave at an angle of $0°$ is chosen. When $N = 3$, compound waves with angles $0°$, $-10°$, and $+10°$ are used. And for $N = 11$ and $N = 21$, we additionally consider intermediate angles. It is important to mention that the millimeter-sized bubbles in this setup ascend at a velocity of 0.3 m/s. Consequently, they only move approximately 6 μm between two compound waves. Even at the maximum number of compound waves, the bubble displacement is still less than fifty percent of the acoustic wavelength. Consequently, in our analysis, we regard them as static bubbles.

The significant difference in acoustic impedance between water and air results in notable acoustic reflection at the liquid-gas interface of the bubbles facing the transducer. Interestingly, even a single plane wave yields adequate contrast in ultrasound imaging to identify bubble positions. Incorporating additional angles enhances the signal-to-noise ratio, minimizes imaging artifacts, and improves vertical resolution. Nonetheless, bubble detection and localization do not rely on compounding. This is of great importance, as instead of using 21 compounding angles with frame rates of 2.2 kHz, we can utilize single plane wave imaging with a much higher frame rate of 46 kHz in this case. This method streamlines processing and, crucially, enhances the attainable frame rate for the examination of fast dynamics of cavitation bubbles.

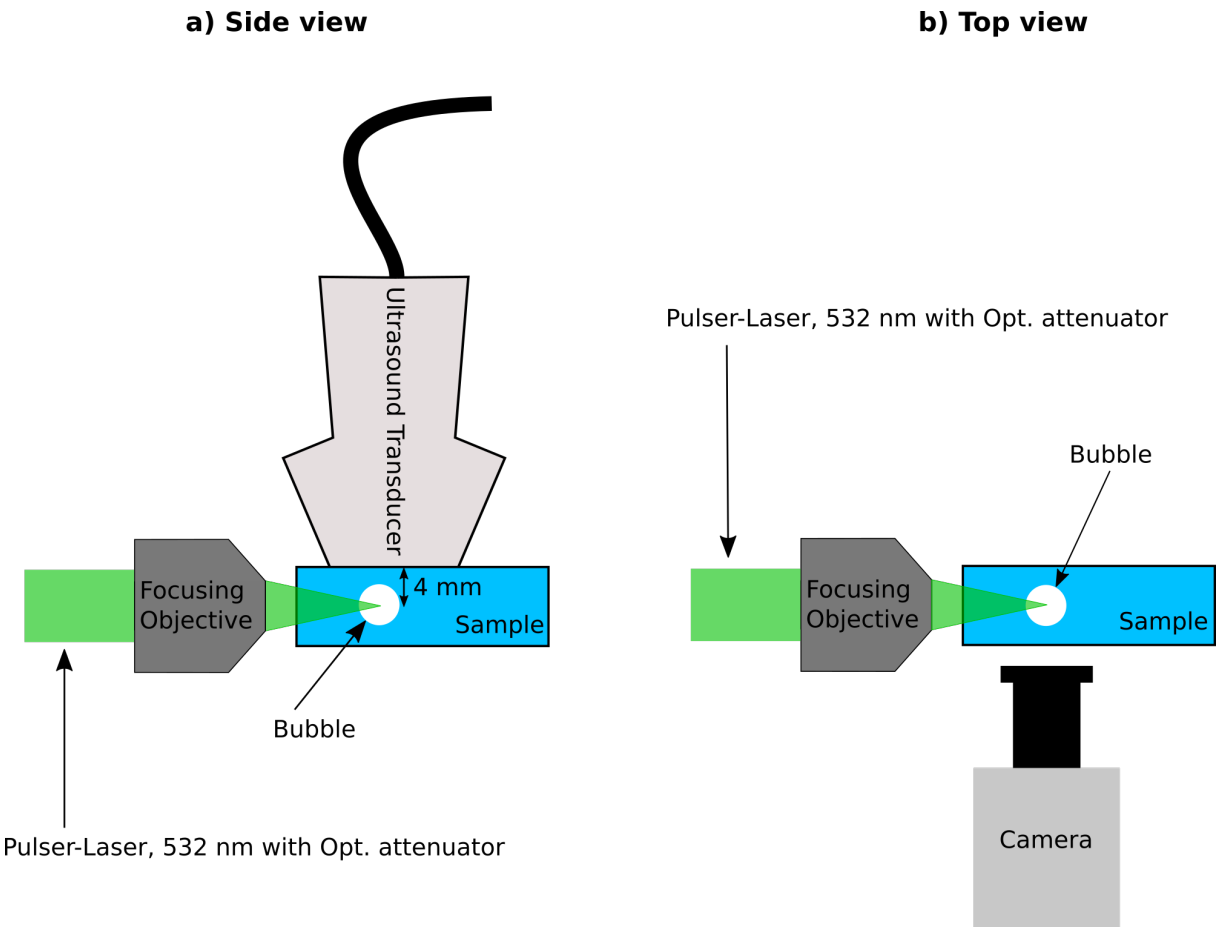

Figure 2.9: a) side view of the setup for generating and recording single cavitation bubbles in water and gelatin samples. The ultrasound transducer comes from the top and records data for an imaging depth of 6 mm. The cavitation bubbles are generated at a distance of about 4 mm below the transducer through laser breakdown. b) Top view of the setup, showing the high-speed optical imaging path.

2.7 Single plane wave imaging of transient cavitation bubbles

As we already know that single plane wave imaging is enough for observing bubbles, in the next step we explore the rapid dynamics of expanding and collapsing cavitation bubbles in water using only single plane wave imaging. Fig. 2.9 illustrates the experimental setup, where the acoustic and optical imaging techniques are employed simultaneously to record the bubble dynamics. The bubble is observed from two perspectives: from the top using the ultrasound probe, connected to the Verasonics system and from the side using an optical high-speed camera (Photron, FASTCAM Mini, AX200). The illumination in the cuvette's interior shadowgraphs is conducted using a continuous white LED lamp SMETec

(9000 lm). Laser-induced cavitation bubbles are produced individually by focusing a collimated laser pulse (Litron Nano series, Q-switched Nd:YAG, 6 ns, wavelength 1064 nm) into the imaging region with a microscope objective (Leitz, Wetzlar UM 20/0.33).

The optical breakdown at the focal region of the lens initiates the bubble's dynamics, including expansion, collapse, and rebound. The high-speed camera captures the bubble's dynamics and Simultaneously, the ultrasound imaging system records reflected Radio Frequency (RF) data from single plane waves. The devices are meticulously synchronized using a digital delay generator (BNC 525, Berkeley Nucleonics), guaranteeing concurrent activation of ultrasonic imaging and the camera upon the start of the laser pulse.

2.8 Cavitation bubble dynamics in water

As already discussed in Chapter 1, after focusing the pulsed laser beam into water, a cavitation bubble emerges which rapidly expands to a maximum radius before collapsing, and subsequently undergoes a series of rebounds and the bubble oscillations eventually cease. The collapse is usually violent, leading to the formation of multiple bubble fragments. The minute gas pockets may subsequently float due to buoyancy, and their non-condensable gas content diffuses back into the liquid, ultimately resulting in the absence of any stable bubble in the water.

Figure 2.10 displays chosen frames from the high-speed optical recording, illustrating the dynamics of a cavitation bubble throughout its expansion, collapse, and rebound in water. The bubble forms around 4 mm beneath the ultrasonic transducer, attaining a maximum radius of $R_{\max} = 730\mu$m and collapsing 130μs post-formation. A line is also displayed to indicate the origin of the z-axis, directed downward. The location $z = 0$ denotes the upper bubble-water boundary at the maximum bubble radius. In the frames preceding the initial collapse, when the bubble's center is practically stationary and its spherical shape is preserved, the difference in z between two consecutive frames roughly shows with the change in radius. However, following the collapse the bubble's center relocates, and the bubble moves toward the transducer, which functions as an attractive hard barrier. Thus, the displacement of z now signifies not just the change in bubble size

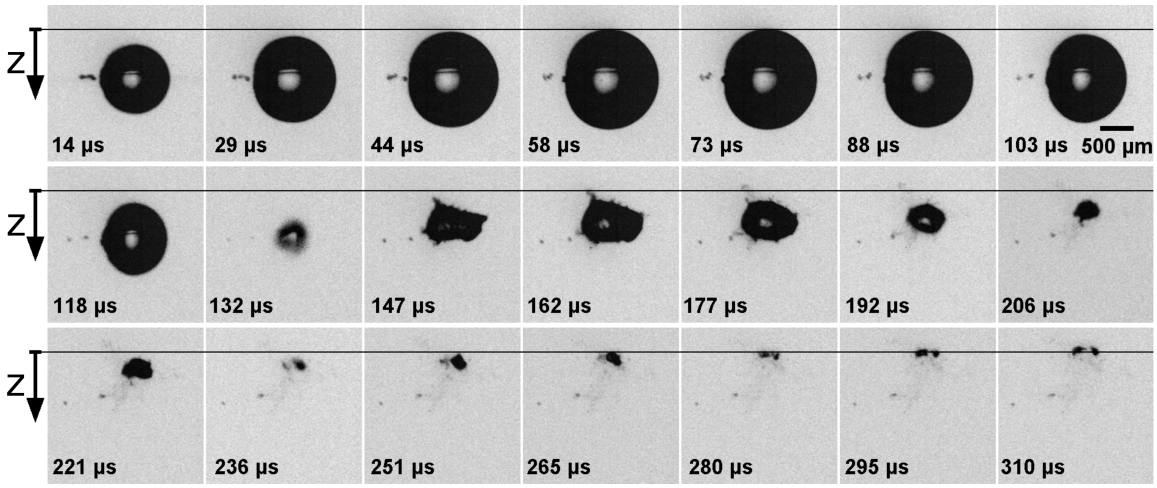

Figure 2.10: Selected frames of a laser induced cavitation bubble dynamics in water, recorded at a frame rate of 67500 frames/s, and an exposure time of 4 μs. The laser comes from left side and the ultrasound transducer comes from the top. Before the first collapse, the bubble center remains almost stationary. However, after collapse, the bubble moves towards the ultrasound transducer which acts as a rigid boundary.

but also the movement of the bubble.

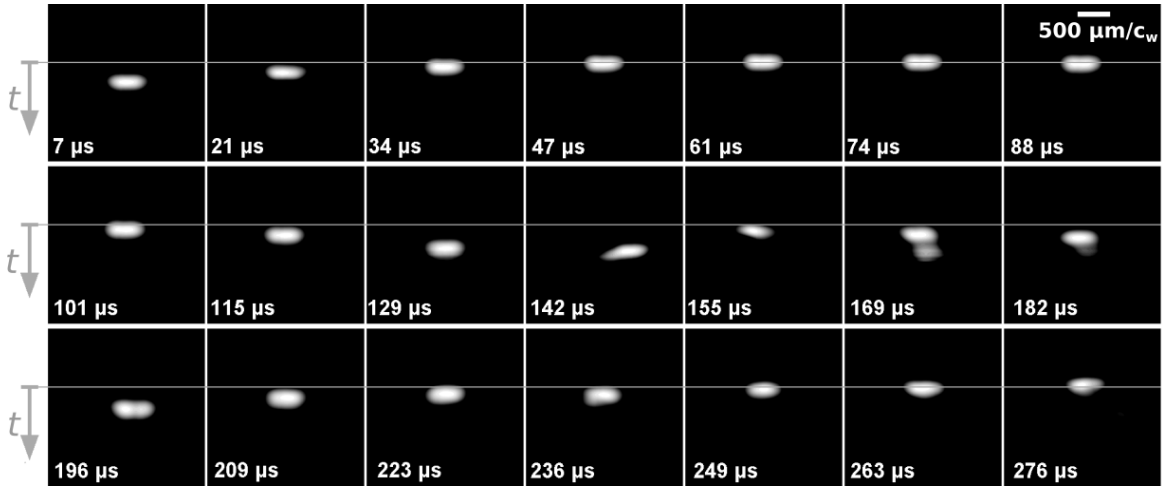

Figure 2.11: Ultrasound images of the bubble, reconstructed utilizing the DMAS algorithm and acquired through single plane wave imaging technique. The ultrasonic transducer is positioned horizontally at the top of each frame. A temporal axis is established under the assumption of a constant sound velocity of $c_{\mathrm{w}} = 1480\,\mathrm{m/s}$.

Moving forward, we investigate the corresponding ultrasound images in Fig. 2.11 which are reconstructed using the DMAS beamforming algorithm implemented in the ultrasound toolbox USTB from Ref.[87]. The transmitted ultrasound wave is reflected on the bubble-water interface. As a result the bright spots in the reconstructed images indicate the upper-wall position of the bubble, closest to the transducer. While this region is imaged

effectively, it is important to note that deducing the actual size of the bubble directly from the acoustic image is not possible. Although the minimum resolvable bubble size is not studied here, at 276μs when the bubble's dimensions are only 60μm vertically and 300μm horizontally, it is still well-imaged using the acoustic technique. In contrast to a z-axis established in the optical images, we define a time axis for the ultrasound images, with the positive direction oriented downward. The temporal reference, designated as $t = 0$, is established at the instance of minimal reflection delay of the initial oscillation cycle, specifically coinciding with the peak expansion of the bubble.

Under the assumption of an ideal soft reflector, a position-stable bubble, and a constant sound speed in the liquid, a straightforward relationship exists between the reflection delay t and the instantaneous bubble radius $R(t)$: $t \propto R_{\max} - R(t)$. The proportionality coefficient is the inverse of the speed of sound, represented as $1/c$. Nonetheless, it is observed that following the initial collapse, the displacement of the bubble centroid and the non-spherical morphology bring complexity that diverge from this straightforward equation. To obtain the reflection delay t from the acoustic pictures, a $2D$ Gaussian is fitted to the intensity planes of Fig. 2.11. Subsequently, we ascertained the location of the bubble wall closest to the transducer by locating the peak of the Gaussian fit.

Prior to quantifying the instantaneous bubble radius $R(t)$, the position of the upper bubble wall z, illustrated in Fig. 2.10, and the reflection delay t, depicted in Fig. 2.11, are ascertained and presented in Fig. 2.12 as a function of time. The displacement of the bubble's upper wall from its maximum size position, derived from optical images, is depicted on the left vertical axis, whilst the acoustic reflection delay, obtained from ultrasound images, is shown on the right vertical axis. Both axes have the same origin for clarity and comparability.

Assuming negligible motion of the bubble center during the initial oscillation cycle, the evolution of bubble radius extracted from both optical and ultrasound images is depicted in Fig. 2.13. A comparison with the Rayleigh-Plesset model discussed in Section 1.2 highlights a notable agreement between the experimental findings and the theoretical model. Measuring the bubble radius from the optical high-speed images is straightforward.

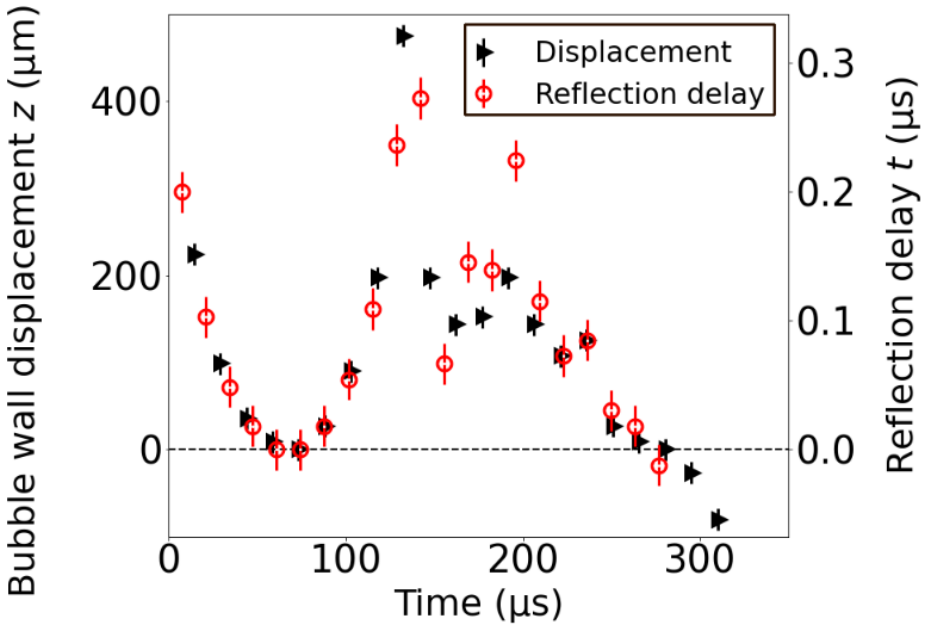

Figure 2.12: The left axis depicts the displacement of the upper bubble wall from its maximum size position, whereas the right axis indicates the time delay between the reflection of the ultrasound wave from the upper bubble wall in each frame and the frame associated with the bubble's maximum size.

However, ultrasound images exclusively reveal the upper wall of the bubble, preventing the extraction of the absolute bubble radius in each frame. Consequently, only the change in bubble radius can be assessed from ultrasound images. To establish absolute values for the bubble radius over time, the maximum bubble radius obtained from the high-speed camera is utilized. Additional studies are required to confirm determining the bubble center based on the spherical shockwave emitted during bubble formation and captured by the ultrasound transducer. By tracing the recorded pressure pulse backward, the origin of this wave—and thus the bubble's center—can potentially be identified.

2.9 Cavitation bubble dynamics in Gelatin

The same experimental setup is employed to record laser-induced cavitation bubble dynamics in gelatin. Gelatin is a hydrogel with an acoustic impedance similar to that of water which is a common choice for TMMs[88] and offers adjustable elastic properties through changes in its concentration. Numerous recent studies have used gelatin to in-

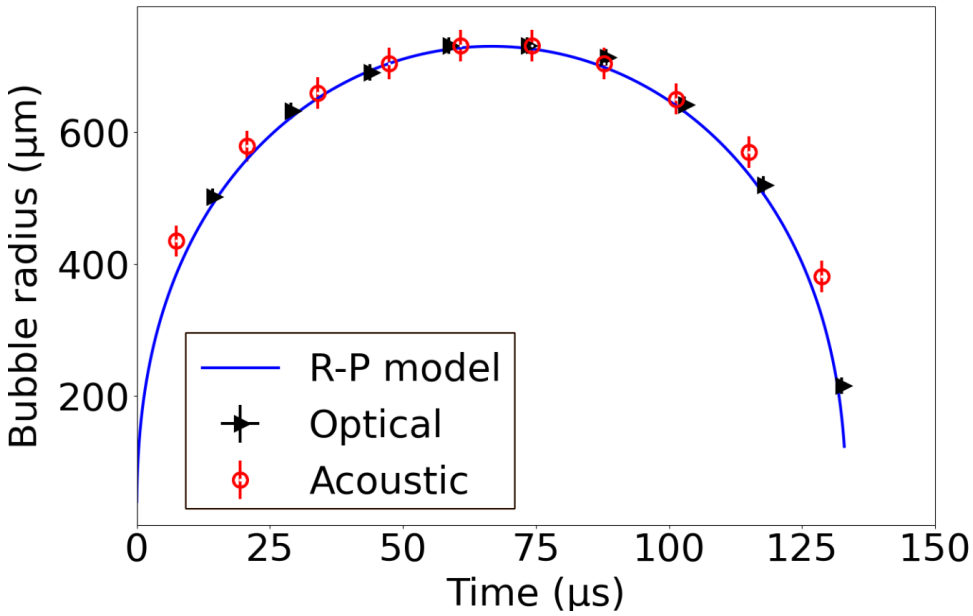

Figure 2.13: Temporal variation of bubble radius as recorded by a high-speed camera, an ultrasonic machine, and a fitted Rayleigh-Plesset model.

vestigate the dynamics of cavitation bubbles within an elastic medium[89–91]. In this process, we prepare samples using powdered gelatin (Gelatin 250 bloom, Yasin Gelatin CO., LTD) by creating a mixture of gelatin and deionized water at a mass ratio of 4% (gelatin to water), which is then dissolved in a flask on a hot plate equipped with a magnetic stirrer. The heated mixture is subsequently transferred into a custom-designed cuvette measuring $35 \times 25 \times 55\text{mm}^3$, featuring an open top for ultrasound imaging and three optically transparent sides to enable accurate laser focusing, clear observation, and illumination (see Fig. 2.9). Upon reaching room temperature, the samples are refrigerated and subsequently returned to room temperature before to use. To minimize wave reflection, the bottom wall of the cuvette is made from low-density polyethylene film, and the cuvette is situated atop a water tank with a depth of 60 mm.

After directing the laser beam into the gelatin sample, a cavitation bubble emerges, undergoing expansion, collapse, and rebound phases similar to those observed in water. However, in contrast to cavitation in water, a stable bubble remains near the laser focus within the gelatin for a prolonged duration. Over time, the residual bubbles within the gelatin may either diminish due to the elastic forces of the gelatin or expand through

diffusion, particularly if the gelatin is adequately supersaturated[92].

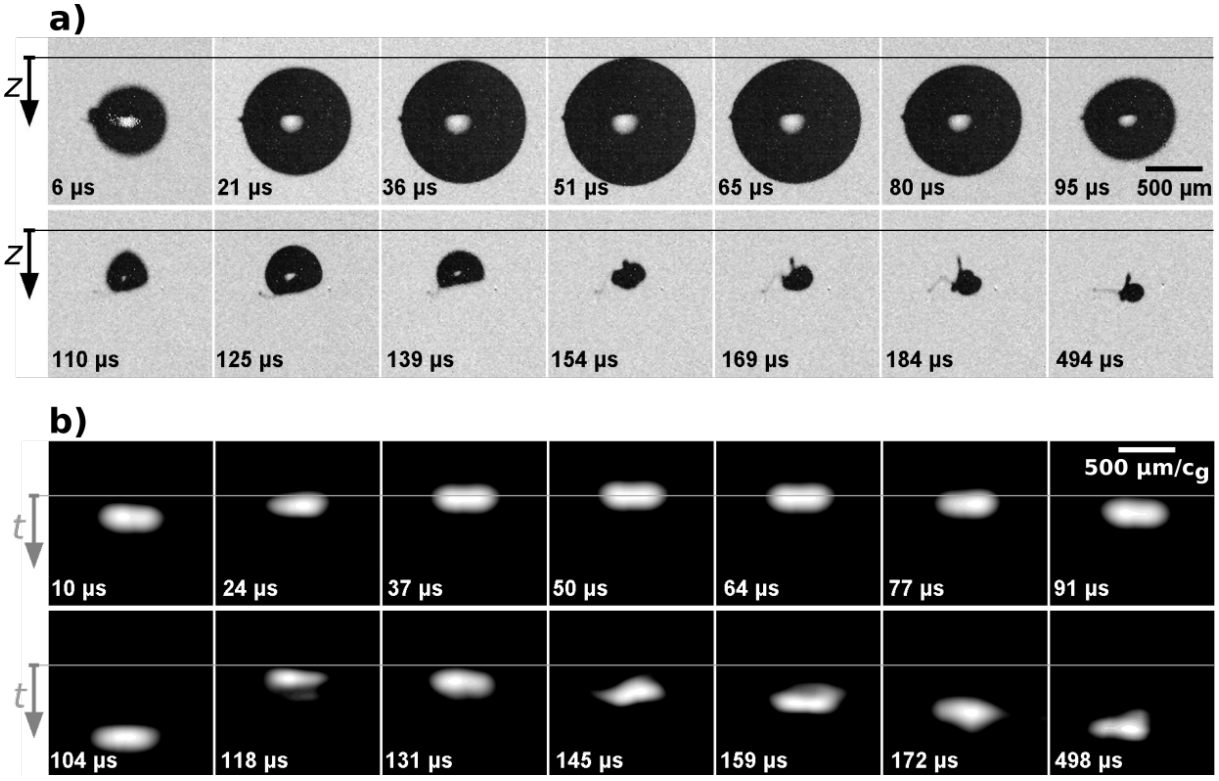

Figure 2.14: Visualization of the dynamics of a laser-generated cavitation bubble within gelatin. (a) Images captured with a high-speed camera operating at 67, 500 frames per second. (b) Corresponding ultrasound frames of the bubble, reconstructed using single-plane wave imaging ($N = 1$), with the transducer positioned horizontally at the top of each frame. Both image sets (a and b) are presented at identical spatial scales, assuming a uniform sound speed of 1540m/s. A temporal axis is provided for the ultrasound data.

In Fig.2.14a, optical results are presented in a similar way to those in Fig.2.10. The generated bubble in this case reaches a maximum radius of 540μm and exhibits a lifetime of approximately $T_{\mathrm{L}} \approx 104\mu$s. The last optical frame shows the remaining gas bubble. The same ultrasound technique is also used here for the ultrasound images shown in Fig.2.14b. There is one outlier within the dataset presented in Fig.2.14b which we would like to highlight. At $t = 104\mu$s, the transducer receivers capture the shock wave emitted from the collapsing bubble rather than the reflection of the transmitted signal from the bubble-water interface. Notably, the shock wave's pressure amplitude is higher that of the reflected signal, consequently leading to an inaccurate reconstruction of the bubble.

Figure 2.15a illustrates the position of the upper bubble wall z obtained from optical imaging and the reflection delay t recorded through ultrasound imaging. In the water

scenario depicted in Fig. 2.12, it is observed that after approximately 300μs, the position of the upper bubble wall registers a negative value in both z and t. This indicates the bubble's movement due to buoyancy here. Conversely, in the gelatin case illustrated in Fig. 2.15a, at time around 180μs, the bubble position is situated proximate to the bubble nucleation point.

As observed in Fig. 2.15b, during the initial bubble cycle, there is a notable agreement between the acoustic and camera data. However, the Rayleigh-Plesset model predicts a shorter bubble lifespan. Incorporating the elasticity of the gelatin material [93] would provide a more accurate fit for the collapse and the elasticity of the soft material could be potentially measured in this way.

2.10 Conclusion

To summarize, this chapter presents an ultrasonic plane wave imaging technique capable of capturing the dynamics of sub-millimeter-sized cavitation bubbles at ultra-high frame rates, reaching up to 74.2kHz. The only limiting factors affecting frame rate in this technique are the speed of sound within the medium and the imaging depth. Validation of the acquired data is conducted through comparison with optical high-speed imaging and the application of the Rayleigh-Plesset model to analyze bubble oscillation, both within water and gelatin serving as a TMM. Utilizing a transparent TMM facilitates controlled cavitation bubble generation and facilitates direct comparison with optical imaging techniques.

Although the acoustic wavelength is relatively large, around 300μm, the integration of significant acoustic contrast and an adequately high sampling rate enables the imaging of the bubble wall with precision akin to that of high-speed cameras. It is significant that, despite utilizing a single plane wave imaging technique, the data quality remains elevated, indicating the possibility of attaining high acoustic framing rates. The analogous quality of outcomes in a TMM and water substantiates the assertion that plane wave imaging may serve as an effective method for monitoring transient cavitation in opaque tissues. However, in vivo measurements are essential for thorough validation.

Furthermore, the bubble dynamics in tissues are influenced by their elastic properties, as highlighted in previous studies [93] and the plane wave imaging could provide a means to monitor the progression of cavitation-based therapies in tissues. The technique also could be potentially used in thermal-based therapies, such as radio wave ablation, with monitoring the rapid bubble dynamics. A remaining challenge lies in extending the technique to monitor deeper into tissues without compromising framing rates. One possible solution involves sustaining a high excitation pulse rate and applying signal analysis to targeted delay intervals (gates), similar to methodologies used in high-pulse repetition frequency Doppler velocimetry [94].

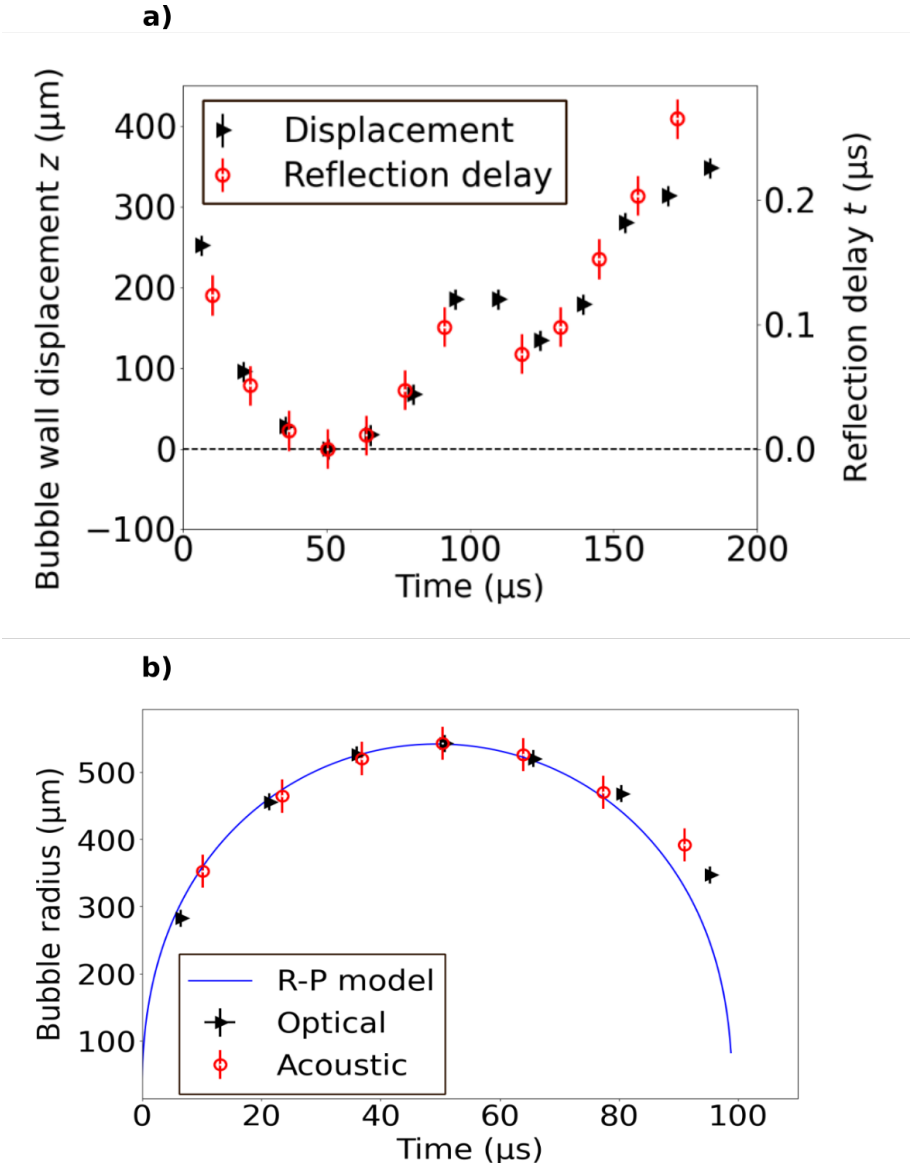

Figure 2.15: a) Graph depicting the displacement of the upper bubble wall in relation to its maximum dimension, obtained from high-speed camera data on the left axis, alongside the time delay between ultrasonic wave reflections off the bubble's upper wall in each frame and the frame of maximum bubble size on the right axis. b) Comparison of bubble radius over time, derived from optical and ultrasound imaging and a fitted Rayleigh-Plesset model.

Chapter 3

Shear wave by laser-induced cavitation bubble

The work presented in this chapter has been published in parts in S. Izak Ghasemian, F. Reuter, Y. Fan, G. Rose, and C. D. Ohl. "Shear wave generation from non-spherical bubble collapse in a tissue phantom", Soft matter, vol. 19, no. 48, p. 9405–9412, 2023, see Ref. [95]. There I was the lead author. My contribution to the publication was conducting the experiments, performing the data analysis, and drafting the manuscript.

3.1 Introduction

As we already talked about it in Section 1.4, Shear Wave Elastography (SWE) is one of the widely used elastographic techniques to measure tissue elasticity by measuring shear wave propagation speed in a region of interest in tissue. A crucial step in this technique involves the generation of shear waves within the tissue, so that in the next step its propagation speed can be measured. The acoustic radiation force impulse technique is frequently employed for this purpose.[95, 96]. This method employs focused ultrasound push beams to create local displacement in the tissue, resulting in the emergence of a

shear wave. Shear waves may also be produced by external mechanical vibrations [97], Lorentz forces in conductive materials [98], bubble nucleation through electrolysis [99], and the collapse of cavitation bubbles close to tissue-air interfaces [100].

In this chapter, we demonstrate that the non-spherical dynamics of a cavitation bubble near a rigid boundary, typically encountered in proximity to hard tissue or bone, results in the generation of shear waves too. The shear waves caused by cavitation are detected using high-speed optical imaging, which captures the motion of tracer particles. We subsequently establish a link between particle mobility and cavitation bubble dynamics by high-speed photography. Single bubbles are efficiently generated at varying distances from a solid boundary in a soft solid using a pulsed focused laser beam, as discussed throughout this thesis. Our exploration of the potential of cavitation bubbles to induce shear waves is motivated by the rather common occurrence of bubble nucleation in various medical procedures. Examples include HIFU [101, 102], histotripsy [103, 104], laser lithotripsy [37, 105], and thermal ablation of tumors [106, 107], to name a few. Cavitation has also been documented in the brain after skull trauma [45], and in synovial fluid during joint manipulation [108, 109].

3.2 Experimental setup and methodology

Gelatin samples are used as a Tissue Mimicking Phantom (TMP) as it is transparent at low concentrations so that it enables us for optical imaging. In addition, the elastic properties of the TMPs can be adjusted by changing the gelatin concentration. Here the idea is to measure the displacement field in TMPs over time so that we can follow the propagation of shear waves in the gelatin samples. The conventional method for measuring the displacement field is based on volumetric seeding of particles in samples and illuminating the plane of interest with a light sheet. However, we instead seed the particles in a plane and illuminate the entire volume here. This approach is beneficial since the main objective in this chapter is to investigate the physics underlying the shear wave generation by single cavitation bubbles and its correlation with the dynamics of bubbles. In volumetric particle seeding, the laser pulse intended to create a cavitation bubble is

absorbed, resulting in the formation of numerous bubbles along the laser beam's trajectory, complicating the detection of the shear wave produced by an individual cavitation bubble. To measure the displacement field, we therefore insert graphite particles into a layer that serves as optical tracers.

Following the procedure detailed in subsection 2.9, the TMPs are prepared by dissolving powdered gelatin in deionized water at a mass ratio of 4% (gelatin to water). The elasticity of parenchymal tissues is comparable to that of a specific concentration of 4%[110]. The mixture is placed into a cuvette ($20 \times 20 \times 10$ mm^3) that has glass windows on three sides, allowing for optical access for accurate laser focusing, high-speed camera observation, and illumination.

A 3D-printed spacer, measuring 1mm in thickness, is inserted from above into the uncured gelatin to introduce the tracer particles at a designated plane. The samples are thereafter stored in a refrigerator for gelation. Upon curing, the spacer is meticulously extracted, and the resultant cavity is filled with a newly cured mixture of gelatin and graphite particles. This mixture is prepared by incorporating graphite particles (Fluka 231-153-3, diameter distribution 5-20 μm) at a mass ratio of 0.1% into the aforementioned gelatin solution. The samples are once more gelled in a refrigerator. Prior to utilization, we confirm that the samples have attained room temperature. Following the stimulation of shear waves in the samples, the propagation of these waves is quantified by the shear-induced displacement of graphite tracer particles via a PIV approach.

The experimental setup is illustrated in Fig. 3.1. A microscope objective (Mitutoyo 50x, NA = 0.42, nominal working distance 20.5 mm) is employed to concentrate a collimated laser pulse through the base of a cuvette into the thin layer of graphite particles, resulting in the formation of a single laser-induced cavitation bubble. To attain optical index matching, the output aperture of the microscope objective and the cuvette are submerged in water.

The distance of the bubble from the boundary is a critical parameter for characterizing bubble dynamics, expressed as $\gamma = d/R_{\max}$. In this equation, d denotes the distance from the center of the plasma to the solid boundary, while $R_{\max}$ indicates the maximum

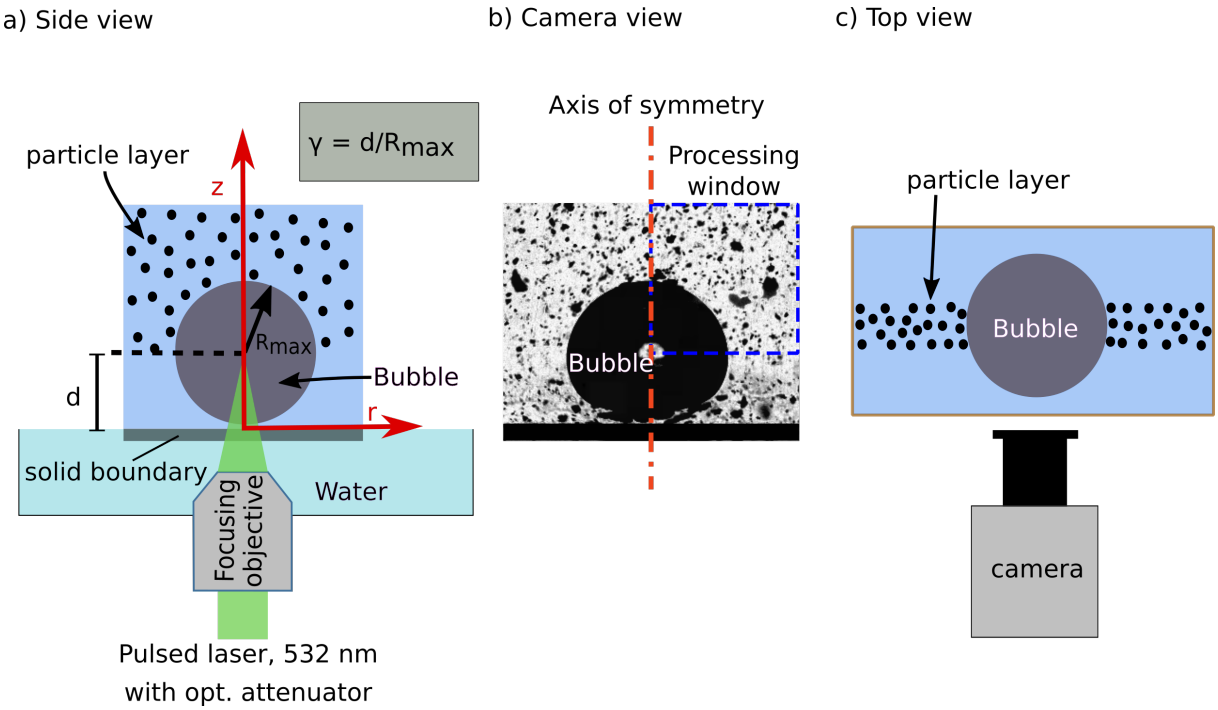

Figure 3.1: Experimental setup for investigating shear waves produced by the non-spherical collapse of a laser-induced cavitation bubble in a TMM, reprinted with permission from Ref.[95]. (a) Lateral viewpoint: A collimated laser beam is focused at a preset distance d from the lower cuvette wall to produce a bubble in gelatin infused with tracer particles. The coordinate system is defined with the wall positioned at $z = 0$, while the plasma and bubble centers are situated along the axis of symmetry at $r = 0$. (b) A sample high-speed image illustrating the bubble at its maximum expansion. The shear field exhibits symmetry along the red axis, whereas the blue box defines the quadrant employed for shear wave observations in this study. The entire plane was infused with particles to ascertain the symmetry of the shear wave emission in this instance. (c) Top view of the arrangement: The bubble is generated within a layer of graphite particles, roughly 1mm in thickness.

bubble radius during expansion. The measurement of $R_{\max}$ is conducted in the direction perpendicular to the solid, as detailed in [111]. The graphite particles are tracked using a Photron camera (Photron, FASTCAM Mini, AX200) at a pixel resolution of 6.5μm per pixel. The cavitation bubble dynamics are recorded with a much higher frame rates (500,000 frames per second) using a Shimadzu HPV-X2 camera. The synchronization of the laser and the high-speed cameras is achieved by a digital delay generator (BNC 525, Berkeley Nucleonics).

The displacement field is acquired using a PIV technique that measures the velocity distribution within a fluid or soft solid by analyzing the movement of tracer particles in image data. For this analysis, we utilize PIVlab, an open-source MATLAB toolbox specif-

ically designed for PIV applications [112]. We employ the Fast Fourier Transform (FFT) window deformation algorithm with three passes and interrogation windows of sizes 64, 24, and 16, each with 50% overlap. Sub-pixel estimation is performed using a Gaussian fit to the integer intensity distribution, which enhances the accuracy of the velocity measurements [113]. Prior to PIV analysis, the images are inverted and background subtracted using a rolling ball background subtraction method with a radius of 20 pixels.

After extracting particle velocities from the images, the kinetic energy density of the propagating shear wave can be approximated. Under the assumption of cylindrical symmetry of the displacement field about the axis of symmetry ($r = 0$), the energy density per unit cross-sectional area, u, at a specific position (r, z) is determined as follows:

$$u = \frac{dU(r,z)}{dA} = \frac{1}{2}\,\rho\,(2\,\pi\,r)(V_r^2 + V_z^2) \tag{3.1}$$

Here, $\rho = 1000$ kg/m^3 signifies the mass density, whereas V_r and V_z indicate the horizontal and vertical speed components at the location (r, z), respectively. Thus, the complete cylindrical volume is taken into account.

3.2.1 Symmetry of shear wave generation

In Fig. 3.1b, a selected image of a cavitation bubble is presented, with the axis of symmetry located at $r = 0$. As for precise shear measurement high pixel resolution is needed, only a smaller geometric section can be imaged. To address this, we use the symmetric shear wave emission and focus on imaging only one quadrant, as indicated by the blue window in Fig. 3.1b. The symmetry is verified at various stand-offs by capturing the entire geometry around the bubble. An instance for $\gamma = 0.48$ is seen in Fig. 3.2. In the left image area, the wave propagates at an angle of 8 degrees, whereas in the right section, it propagates at 10 degrees. The shear wave propagation speeds in both the left and right quadrants are identical, measured at 1.8 ± 0.12 m/s. Assuming symmetric, we henceforth exclusively record and process the shear wave within the blue window of Fig. 3.1b. This approach enables camera recordings at higher resolutions, resulting in more accurate measurements of displacement throughout the rest of this chapter.

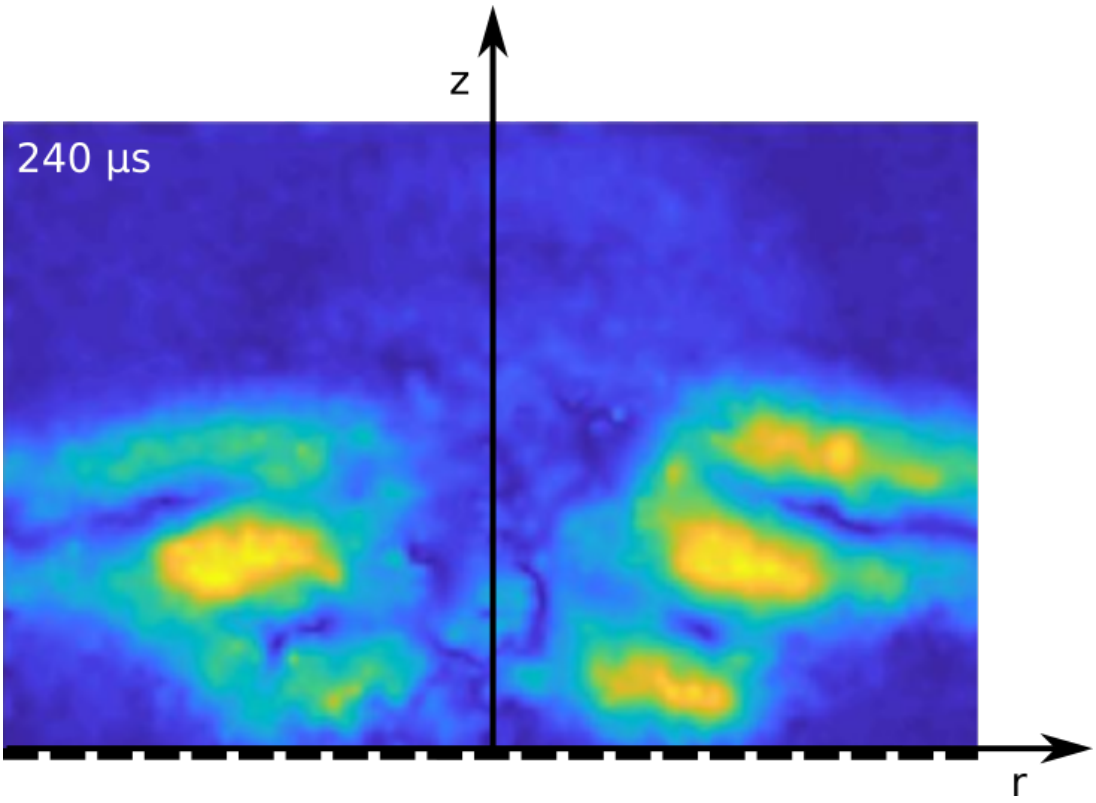

Figure 3.2: Shear observed in the left and right quadrants produced by a cavitation bubble at stand-off distance $\gamma = 0.48$. The solid boundary is indicated by a dashed line beneath the frame. Reprinted with permission from Ref.[95].

3.2.2 Assessing tracer particle behavior: following the shear

To verify that the particles conform to the shear motion within the gelatin, we examine the spatial distribution of particles before and after the cavitation event. Particles that elastically return to their former positions have moved in synchrony with the gelatin, while particles that have detached from the gelatin are located at disparate positions. In Fig. 3.3, an overlay is presented, depicting the initial distribution of particles in purple, and in green after the shear wave has passed, generated using the Matlab function 'imshowpair' where we only show the quadrant window of Fig. 3.1b. This visualization allows for the observation of differences in particle distribution before the cavitation event and after the shear passage. Particles that elastically revert to their original position look black, however little deviations from the initial particle position produce green and purple coronas surrounding the tracer particles. Particles that are completely green or purple signify a movement exceeding their length.

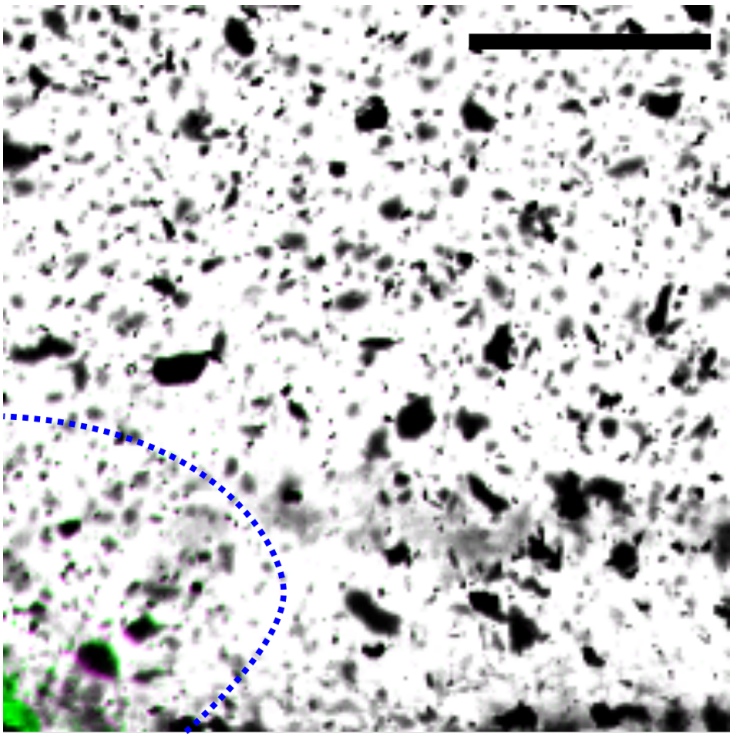

Figure 3.3: Comparison of particle distribution before and after shear wave passage for $\gamma = 0.15$, reprinted with permission from Ref.[95]. Particles are shown in purple at $t < 0, \mu$s (prior to bubble generation) and in green at $t = +4300\mu$s (well after the shear wave exited the frame). The bubble formation occurs at $t = 0$. Regions in black indicate particles that elastically returned to their original positions. This behavior is observed across most of the image area, where the tracers align with the shear flow. The bubble contour at its maximum expansion is displayed. Only in a small localized region, where intense bubble activity occurred, the tracers deviate noticeably from ideal behavior. The scale bar represents 500μm.

The majority of particle positions correspond closely to their initial locations, exhibiting a black appearance. In the lower left corner, where the more intense part of the bubble dynamics occurred, small colored coronas arise around the particles, and a bigger green zone emerges, which is an artifact of the leftover bubble. Only locations where particles elastically adhere to the shear motion are included in the data evaluation, while the lower left region is omitted from analysis.

3.3 Bubble dynamics effect on shear wave generation

The behavior of bubbles in proximity to a solid surface is intricately linked to the stand-off distance. Consequently, we initially examine the dynamics of the bubble, highlighting

three specific stand-off scenarios, before concentrating on the resultant shear waves generated by these dynamics. Figure 3.4 illustrates selected frames from high-speed recordings of bubble dynamics at these three stand-offs.

A dashed line at the base of each frame in Fig. 3.4 indicates the position of the rigid boundary in the experiment, which limits the deformation of the gelatin. Each bubble is initiated at time $t = 0$. For $\gamma = 1.85$, the bubble undergoes spherical expansion, reaching a maximum radius of $R_{\max} = 566 \pm 6\,\mu$m at $t \approx 47\mu$s, shown in the top image sequence of Fig. 3.4. During the subsequent contraction, the bubble's shape becomes progressively non-spherical, and an axial jet forms directed towards the solid boundary. This jet induces axial indentation of the bubble, notably visible in the frame just prior to collapse at $t = 99\mu$s. Such jetting phenomena are commonly observed when bubbles collapse in vicinity of solids in a liquid or soft material[42].

When the stand-off distance is reduced to $\gamma = 0.97$, as depicted in the middle image sequence of Fig. 3.4, the bubble's expansion deviates from a spherical shape. The bubble reaches a maximum radius of $R_{\max} = 555 \pm 6\mu$m and undergoes collapse around $t \approx 108\mu$s. The collapse instance is determined with greater precision than the interframe time of 2μs, achieved through backtracking the shockwave emitted during collapse. The shadowgraphic imaging using an ultrashort pulsed illumination setup effectively captures the shockwave, enabling accurate determination of the collapse at $t = 108\mu$s. Notably, in the frame just before collapse, i.e. at $t = 106\mu$s, the axial indentation of the bubble appears broader compared to the previous case, indicating a wider jet flow.

At the smallest stand-off distance, $\gamma = 0.11$, the bubble reaches a maximum radius of $R_{\max} = 720 \pm 6\mu$m and collapses at $t \approx 116\mu$s, as indicated by the shockwave visualized through shadowgraphy in the last image sequence of Fig.3.4. In this stand-off regime, a considerably different bubble dynamics emerges, leading to the creation of a needle jet, which has been reported in the case of water [114, 115]. This phenomena originates from a planar, initially boundary-parallel jetting flow, as demonstrated by the kink at $t = 108\mu$s. In contrast to prior instances, the bubble indentation during collapse now manifests in the radial direction, distinctly observable at $t = 110\mu$s. Upon collision of the radial jet at

the axis of symmetry, a high-velocity, needle-like jet is produced, exerting axial impact on the boundary. The complex process, taking place between $t = 110\mu$s and $t = 116\mu$s, is not depicted in this image sequence.

Next, we will examine the shear waves generated from these three cases of far, intermediate, and short stand-off distances. In this step graphite particles were introduced into the samples following the procedures detailed in section3.2. The propagation of the energy density associated with the shear wave calculated from Eq. 3.1 in these three stand-off cases is illustrated in Fig. 3.5. Please note that although the stand-off distances slightly differ from those in Fig. 3.4, the dynamics remain representative of their respective cases.

The reference time $t = 0$ corresponds to the moment of bubble generation. Frames are presented for $t > 474\mu$s for the first two cases and $t > 148\mu$s for the third case, well beyond the bubble collapse. These time points ensure that the shear field has adequately propagated, allowing for clear resolution with the present experimental setup. To clarify, the shock wave is not visible in these series due to the significantly higher speed of sound, approximately 1480 m/s, compared to the shear velocity which is less than 2 m/s here. Consequently, the shock wave propagates out of the imaging frame already 1.1μs after its initiation at the collapse instance.

At $\gamma = 1.75$, a shear wave is emitted horizontally, displaying a propagation velocity of $V_s = 1.84 \pm 0.12$m/s. To estimate the uncertainty in shear energy magnitude, we assume that the shear wave front position is detected with an uncertainty equivalent to 1/3 of the PIV window size. This velocity aligns with findings from prior studies using a similar gelatin recipe by Rapet *et al.* [100], who reported a shear wave velocity of $V_s = 1.8$ m/s. The propagation velocity is utilized to determine an elastic modulus of 9.8kPa for the gelatin sample. This calculation is performed using Eq. 1.2, with parameters $\rho = 1000$kg/m^3 and $\nu = 0.45$ [100].

Before delving into the analysis of the intermediate distance, let's first examine the scenario at the closest distance, i.e. $\gamma = 0.15$, shown in bottom graph in Fig. 3.5. In contrast to the previous case, the shear wave here propagates predominantly in the vertical direction, exhibiting significantly higher energy. The total energy in one quadrant amounts to

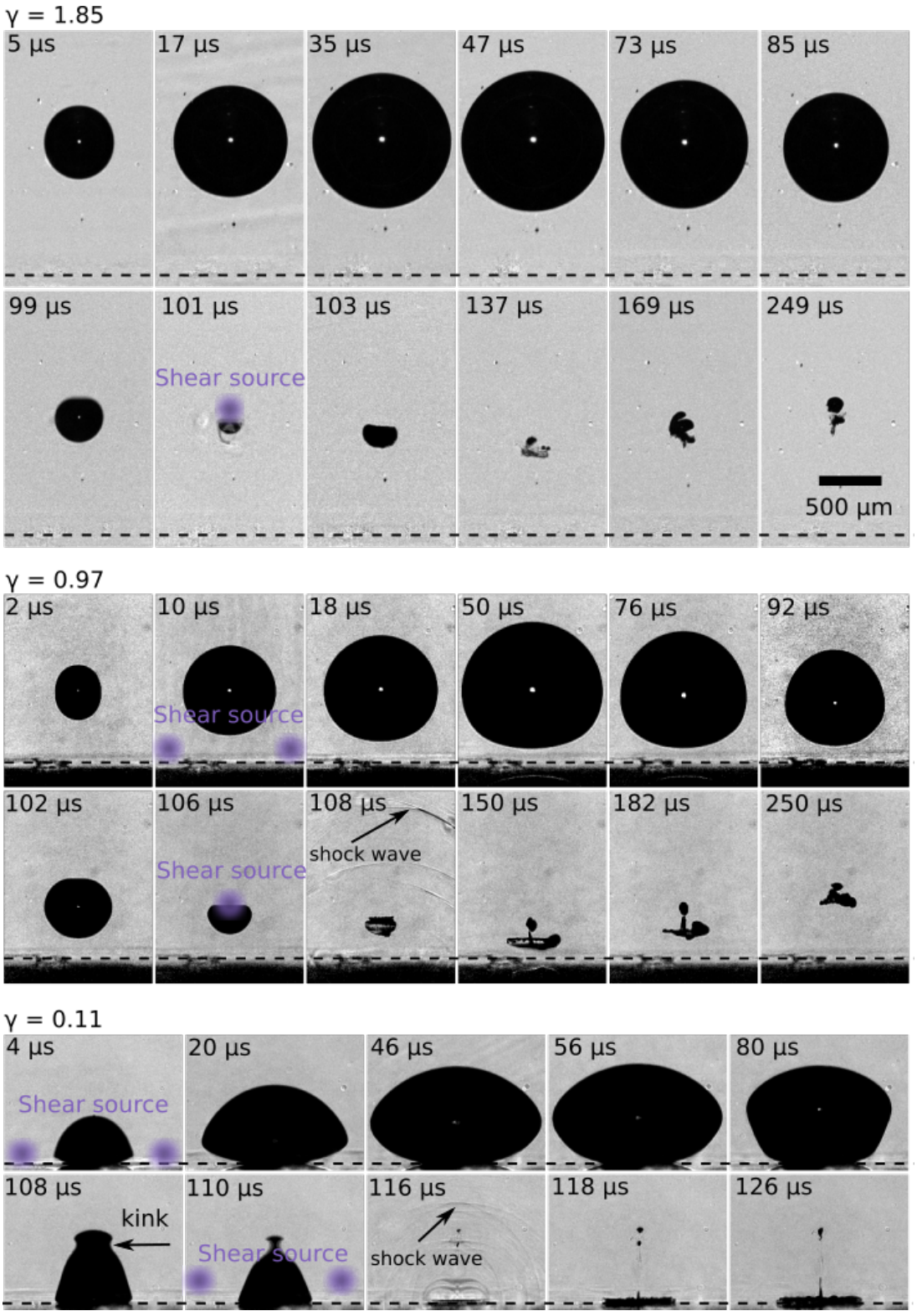

Figure 3.4: Behavior of laser-generated cavitation bubbles in a TMM at three distinct stand-off distances (γ), captured at 500,000 frames/s, reprinted with permission from Ref.[95]. The laser pulse was directed upward, focusing from bottom of the cuvette, with the interface of the solid boundary marked by a dashed line beneath each frame. During the collapse phase of the bubble, a shock wave is produced. The approximate locations of the shear wave origins, determined from Fig. 3.6, are highlighted in the corresponding frames.

0.4μJ, which is seven times greater than that observed in the $\gamma = 1.75$ case. Furthermore, the wave geometries differ markedly between the two cases. While the $\gamma = 0.15$ scenario generates a planar wave, the $\gamma = 1.75$ case produces a wave that is partially spherically shaped.

Analyzing the intermediate stand-off distance, $\gamma = 0.97$, indicates a more intricate pattern. The phenomenon can be described as a superposition of two shear waves: one that propagates nearly parallel to the boundary (HS) and another that propagates approximately perpendicular to the boundary (VS). This indicates that in the intermediate scenario, both mechanisms for shear wave generation are active, resulting in the production of shear waves with approximately equal energy levels. The total shear energy in one quadrant is approximately three times greater than that recorded in the $\gamma = 1.75$ scenario.

3.4 Shear origin

To provide a deeper understanding of the shear wave's origin, we correlate the shear wave emission with the bubble dynamics. Firstly, analogous to the center of mass, but considering the energy distribution instead the mass distribution, we measure energy centroid in each frame and we track the shear centroid in both space and time. Through linear extrapolation of the shear wave trajectory, we trace it back in space and time to localize its origin. Figure 3.6 presents the spatial and temporal propagation of shear waves for large ($\gamma = 1.75$) and small ($\gamma = 0.15$) stand-offs, represented in black and blue, respectively. The reference time $t = 0$ corresponds to the bubble generation, the coordinate $z = 0$ denotes the position of the solid boundary and $r = 0$ denotes the position of the axis of symmetry as illustrated in the schematic view of Fig. 3.1.

Figure 3.6a illustrates the plotted trajectories of shear waves in conjunction with the corresponding bubble shapes at their maximum expansion phase. The centroid of shear generation must align with the linear extrapolations. In scenarios involving a large stand-off distance, the shear wave is generated in proximity to the bubble generation area, specifically at the center of the expanded bubble. In contrast, within the small stand-off

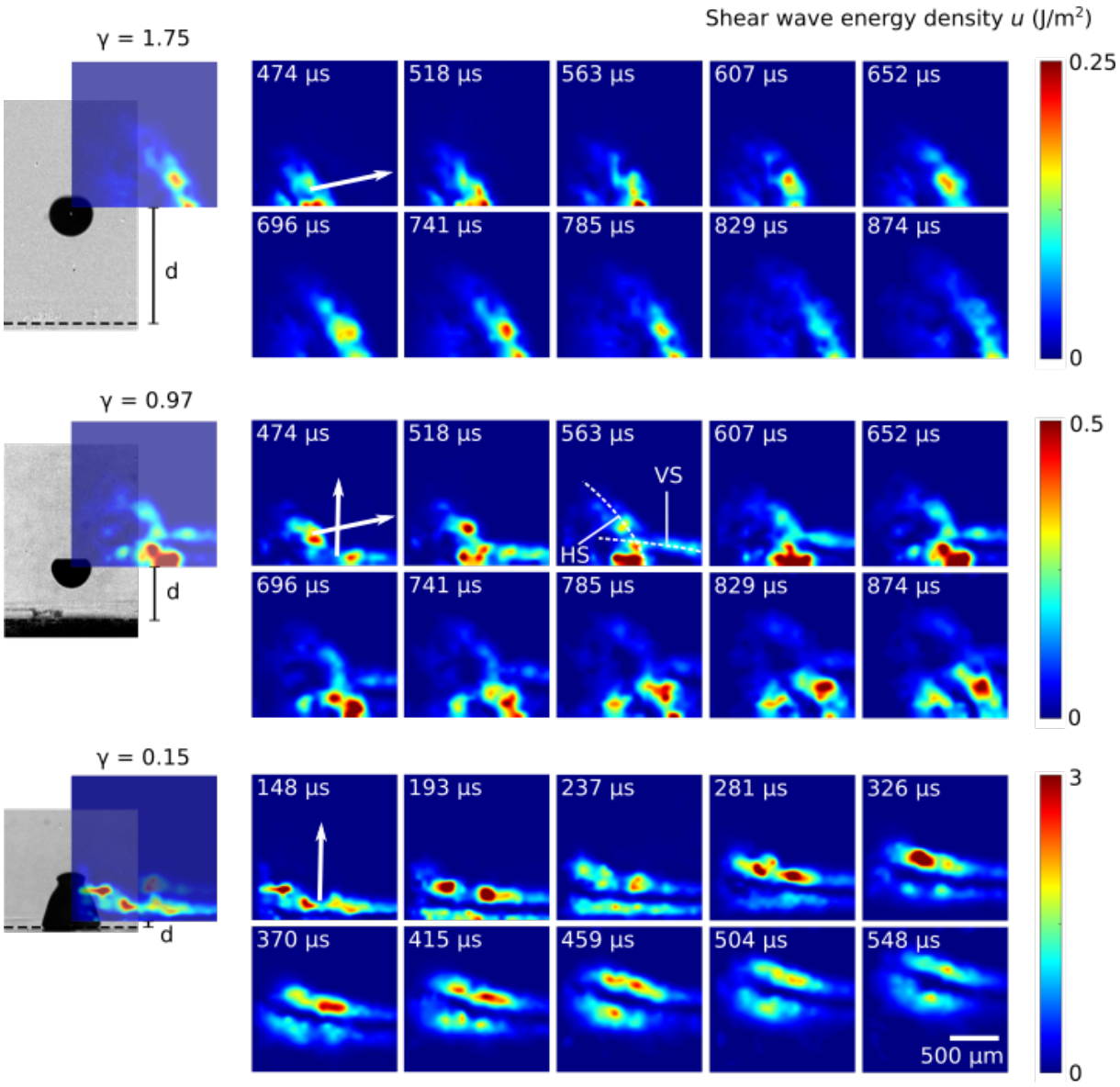

Figure 3.5: Variation of the areal energy density of shear waves over time for three specific stand-off distances (γ), reprinted with permission from Ref.[95]. The shear measurement positions in relation to the bubble are illustrated on the left for each stand-off distance. The bubble on the left is depicted just prior to collapse, with the stand-off distance d indicated. The analysis of shear maps is conducted within the area defined by the blue box in Fig. 3.1b. The Poynting vector of the shear wave, which indicates the direction of energy flux, is depicted in the first frame for each scenario. The directions of the Poynting vector are established by following the linear path of the shear wave fronts, as demonstrated by the slopes of the dashed lines in Fig. 3.6b and c. At a large stand-off distance ($\gamma = 1.75$), the shear wave predominantly propagates in a direction parallel to the boundary. In contrast, for a small stand-off distance ($\gamma = 0.15$), the wave exhibits predominant propagation in a vertical direction, which is perpendicular to the boundary. In the intermediate scenario ($\gamma = 0.97$), a combination of waves propagating both perpendicular and parallel to the boundary is observed. At $t = 563\mu$s, the shear wave traveling in the vertical direction is designated as "VS", whereas the shear wave traveling horizontally is identified as "HS".

scenario, the shear wave is produced at a location significantly nearer to the solid wall and external to the area of maximum bubble expansion.

Figure 3.6b provides further detail, illustrating the positions $z(t)$ and $r(t)$ for the large stand-off scenario. The specified positions denote the coordinates associated with the trajectory of the shear wave. The centroid of shear wave generation must be aligned with the dashed lines once again. The trajectory $r(t)$ is of particular significance in this context, as the shear wave propagates in the r-direction in this scenario. The curve indicates that the shear wave was produced at the collapse instance $T_{\mathrm{C}} = 109\mu$s. At this moment, the trajectory intersects the time axis, and due to symmetry considerations, negative r coordinates are not permitted. As a result, the centroid of shear emission is determined to be $(r(T_{\mathrm{C}}), z(T_{\mathrm{C}})) = (r = 0, z = 1126)\,\mu$m, which is in proximity to the bubble generation point $(r = 0, z = 1098)\,\mu$m.

This position precisely corresponds to the region where the jet forms and penetrates the bubble. The jetting into the bubble is evident from its deformation, as illustrated in Fig. 3.4 for $\gamma = 1.85$ and the time interval $99\mu\mathrm{s} \leq t \leq 103\mu$s, where concurrent with the jetting phenomenon is a motion of the bubble toward the rigid wall. The shear wave's origin implies that it is the formation of the jet on the upper part of the bubble that initiates the launch of the shear wave.

The analysis of the small stand-off case, as depicted in Fig.3.6c, presents a more intricate scenario. This time, in contrast to the previous case, the $z(t)$ trajectory is the relevant one as the shear propagates in the z-direction. The shear wave could potentially be generated either around the collapse instance T_{C}, indicating $z \approx 205\mu$m, or at the time of bubble generation, $t = 0$, with $z \approx 0\mu$m, or at both instances.

To further elucidate the dynamics of shear generation in this case ($\gamma = 0.15$), we present the time evolution of particles located within the designated potential shear generation region, highlighted by the blue box in Fig.3.7. The path of an individual tracked particle is represented by the dashed line, with sudden changes in its slope indicating the generation of shear. The analysis indicates that shear is predominantly produced at the wall and during the initial phases of expansion. Additionally, shear is observed to be

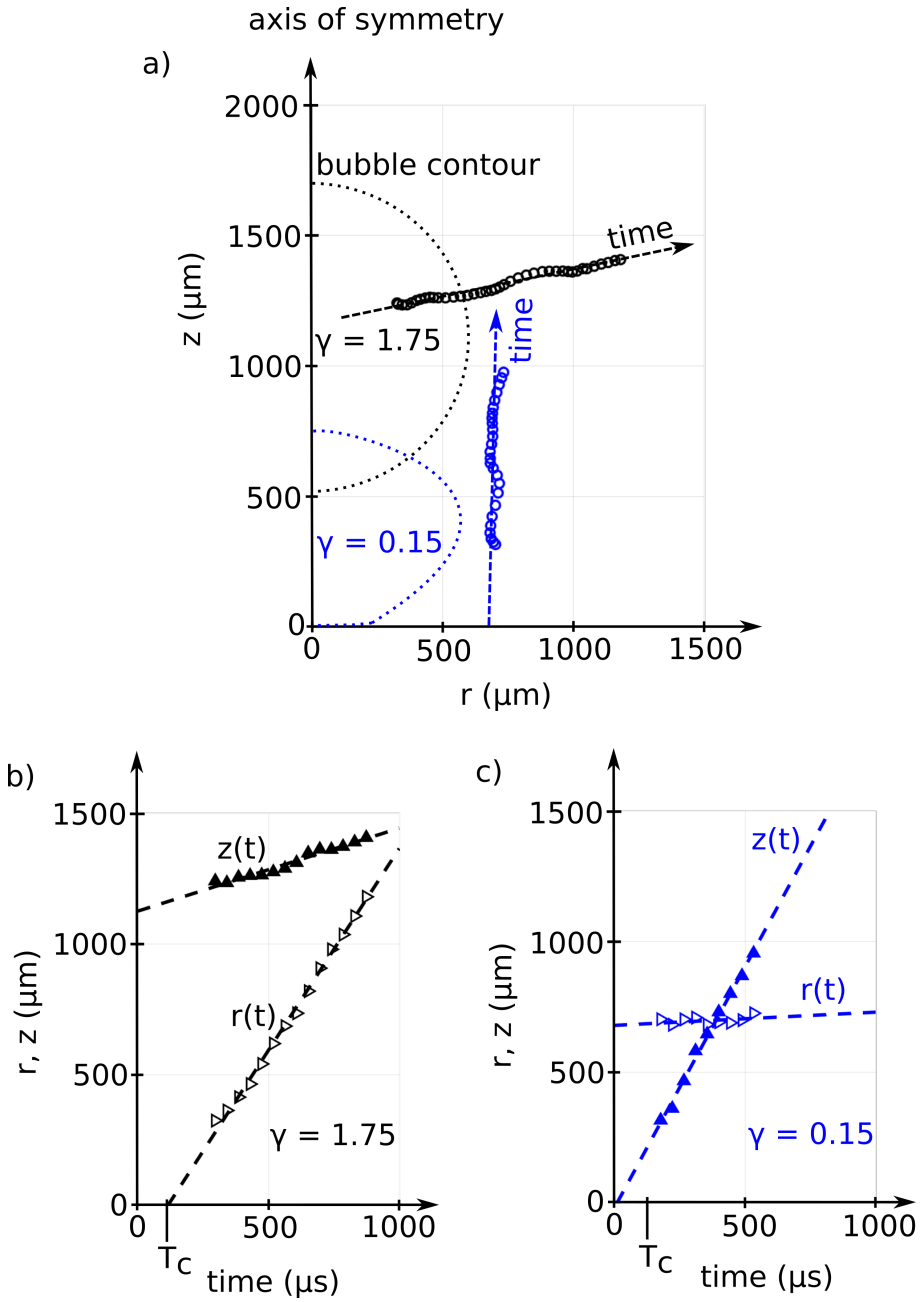

Figure 3.6: The spatial and temporal paths of shear waves are shown for two stand-off distances, reprinted with permission from Ref.[95]: black represents the large stand-off ($\gamma = 1.75$), and blue denotes the small stand-off ($\gamma = 0.15$). Dashed lines indicate linear fits, which are used to trace the shear wave back in both space and time to estimate its point of origin. The solid boundary is positioned at $z = 0$, and T_C marks the moment of collapse. (a) Paths of shear waves and outlines of bubbles at their maximum size. The bubbles were generated at positions $(r = 0, z = 1098)\mu$m and $(r = 0, z = 99)\mu$m, respectively. The shear waves originate from some point along the dashed lines, extended from $t = 0$ to $t = 1000\,\mu$s. (b) and (c) illustrate the trajectories of the shear fronts along the z and r coordinates independently for the two γ scenarios. These plots help narrow down the potential locations of the shear wave sources. In the large γ (b), the shear seems to be predominantly produced at the collapse event, as evidenced by the $r(t)$ curve intersecting the axis of symmetry close to T_C. In the scenario where γ is small, and shear waves propagate in the z direction, the plot of $z(t)$ offers essential insights. This indicates that the shear originated near the solid boundary, either at the time of collapse or during the process of bubble formation.

generated during the late collapse stage and subsequent to the impact of the jet. As a result, both the expansion and collapse phases play a role in the generation of the shear wave for the small stand-off case.

3.5 Shear wave propagation angle

In Section 3.4, our findings demonstrated that the shear wave can be produced either during bubble collapse in the jet region for larger γ or during both expansion and collapse at the wall for smaller stand-offs. Thus, the shear wave propagates either horizontally or vertically respectively, whereas the Poynting vector ideally forms an angle of 0° or 90° relative to the wall. Figure 3.8 illustrates the angle of the Poynting vector with respect to the axis of symmetry as a function of γ. To assess the uncertainties, we initially compute the standard error of the slope[116] of the fitted shear wave trajectories. We then calculate the propagation angle error utilizing the error estimate for the derived quantities[117].

The results demonstrate that for $\gamma < 0.5$, shear wave generation occurs in the wall-near region, whereas for $\gamma > 1$, it takes place around the jet. The stand-offs between $\gamma = 0.5$ and $\gamma = 1.0$ indicate an intermediate regime in which both shear waves are produced. It is crucial to acknowledge that the shear wave produced in the wall-near region may be subject to underestimation in our measurements. The observed phenomenon is linked to the positioning of the shear measurement window in the upper quadrant, indicating a specific propagation distance of the shear wave into the measurement window along with associated attenuation effects.

3.6 Shear efficiency

The shear maps illustrated in Fig.3.5 indicate that the smallest γ results in the maximum shear wave energy. To systematically examine the efficiency of shear wave generation η, we show the ratio of shear energy to bubble energy as a function of the stand-off in Fig.3.9, namely $\eta = U_{\mathrm{SW}}/U_{\mathrm{bubble}}$. In this context, U_{SW} is derived from the area integral $U_{\mathrm{SW}} = \int_{\Omega} u \, dA$, where u denotes the shear wave energy density illustrated in Fig. 3.5,

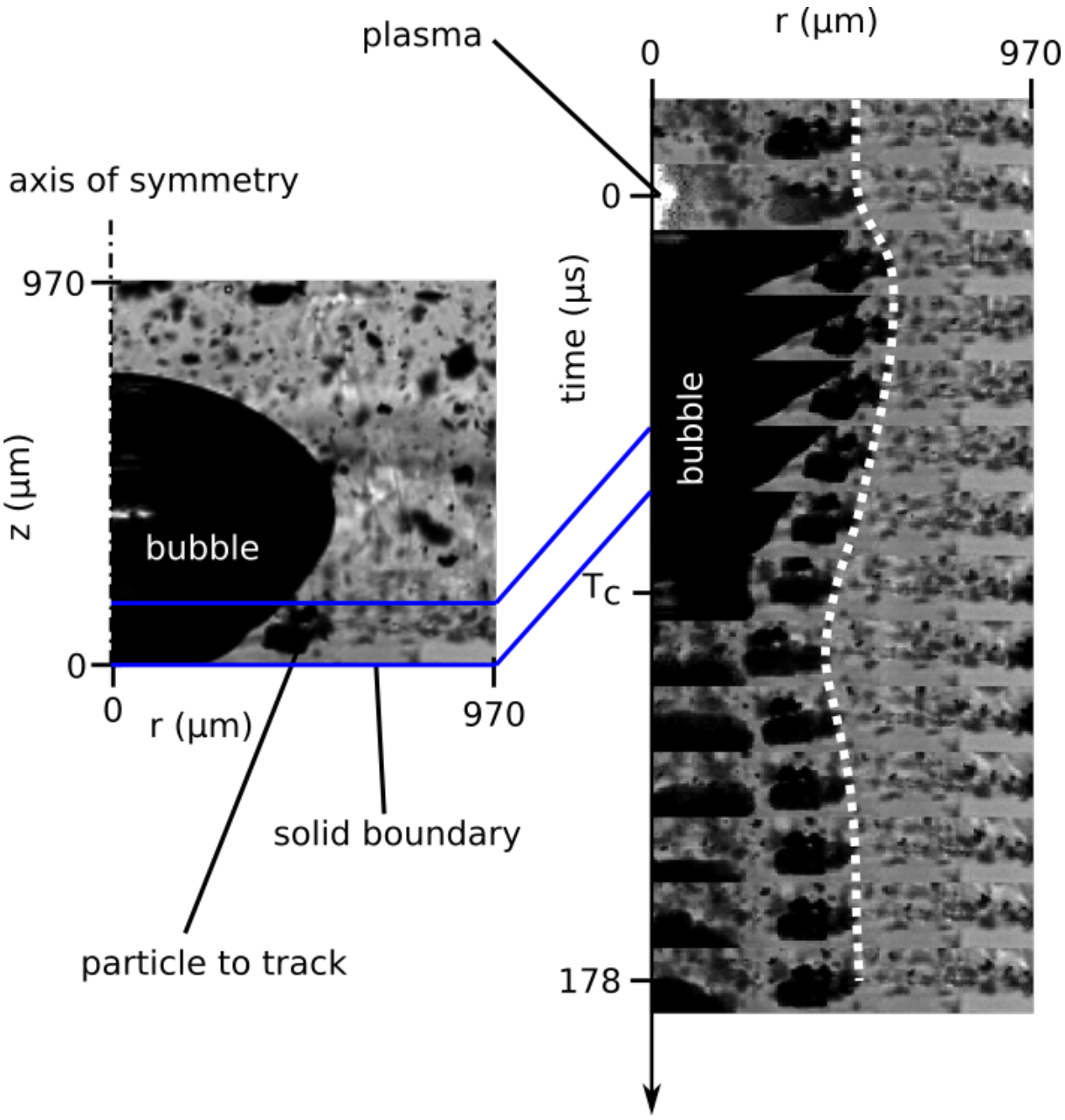

Figure 3.7: Investigation of shear wave generation for the small stand-off case ($\gamma = 0.15$), reprinted with permission from Ref.[95]. The temporal evolution of the region marked by a blue box is presented, with a specific particle's trajectory traced over time using a dashed line. Abrupt shifts in the slope of this line during the initial expansion and the late collapse phases highlight the instances of shear generation.

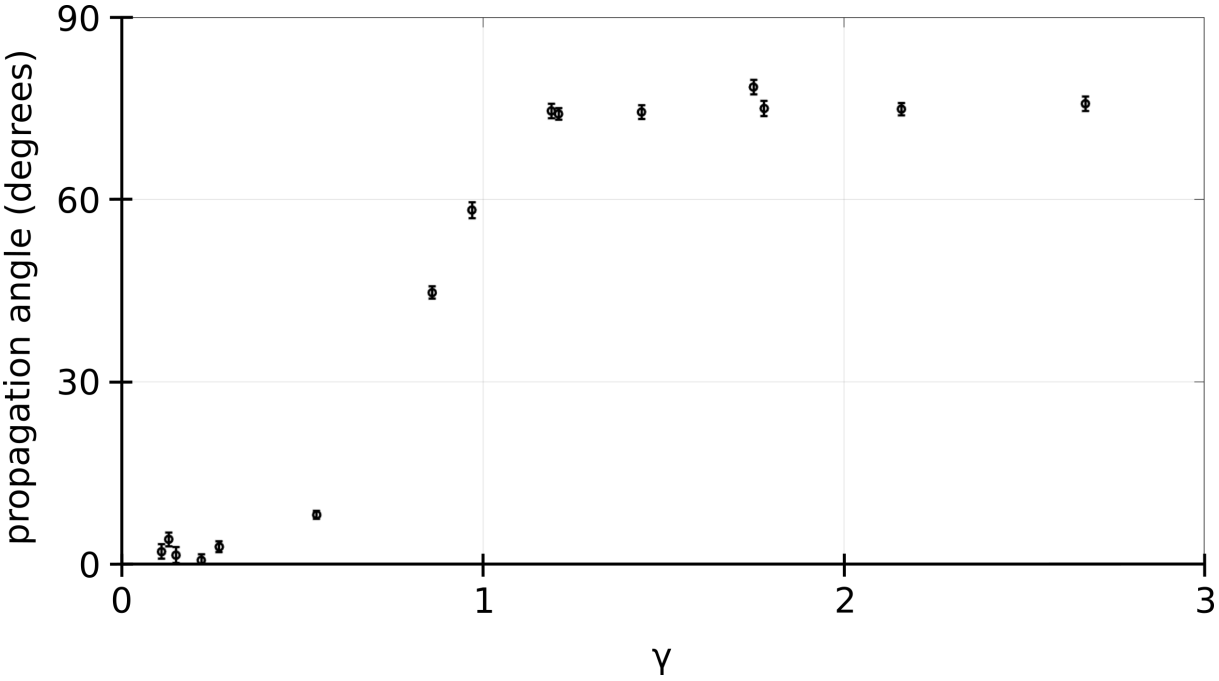

Figure 3.8: The angle of the shear wave Poynting vector, measured relative to the axis of symmetry, reprinted with permission from Ref.[95]. For $\gamma < 0.5$, the shear wave propagates in a direction that is approximately parallel to the axis of symmetry. When $\gamma > 1$, its propagation angle shifts to approximately 75° relative to the axis. In the transitional range ($0.5 \leq \gamma \leq 1$), both shear waves are produced with comparable amplitudes.

and Ω signifies the measurement area. For vertically propagating shear waves that reach the quadrant of evaluation, the entire wave is in the measurement window. However, for horizontally propagating waves, a special treatment is necessary. In these instances, we assume the waves exhibit symmetry about the bottom axis of the evaluation window, thus we multiply the corresponding energy by a factor of two for cases where $\gamma > 0.5$.

The bubble energy is expressed as $U_{\text{bubble}} = p_0 V$, where $p_0 = 1\text{bar}$ denotes atmospheric pressure, and V signifies the maximum bubble volume. To estimate the volume of the non-spherical bubble, we apply the formula $V = \frac{4}{3}\pi R_{\text{max}}^3$ for $\gamma > 1$. For stand-offs less than 1, we utilize the equation $V = \frac{4}{3}\pi R_{\text{max}}^3 - \frac{\pi}{3}(R_{\text{max}} - d)^2(2R_{\text{max}} + d)$ as outlined by Bußmann *et al.* [118], where R_{max} denotes the bubble radius at maximum expansion, and d signifies the bubble seeding distance. Due to the temporal fluctuations of shear energy, we select the maximum energy for our analysis. We estimate uncertainties by assuming a spatial uncertainty of 1/3 of the PIV window size for the detection of the shear front. Figure 3.5 clearly illustrates that shear generation reaches a maximum as $\gamma \to 0$ and tends toward zero as bubble dynamics transition to a spherical form, specifically $\eta(\gamma \to \infty) = 0$.

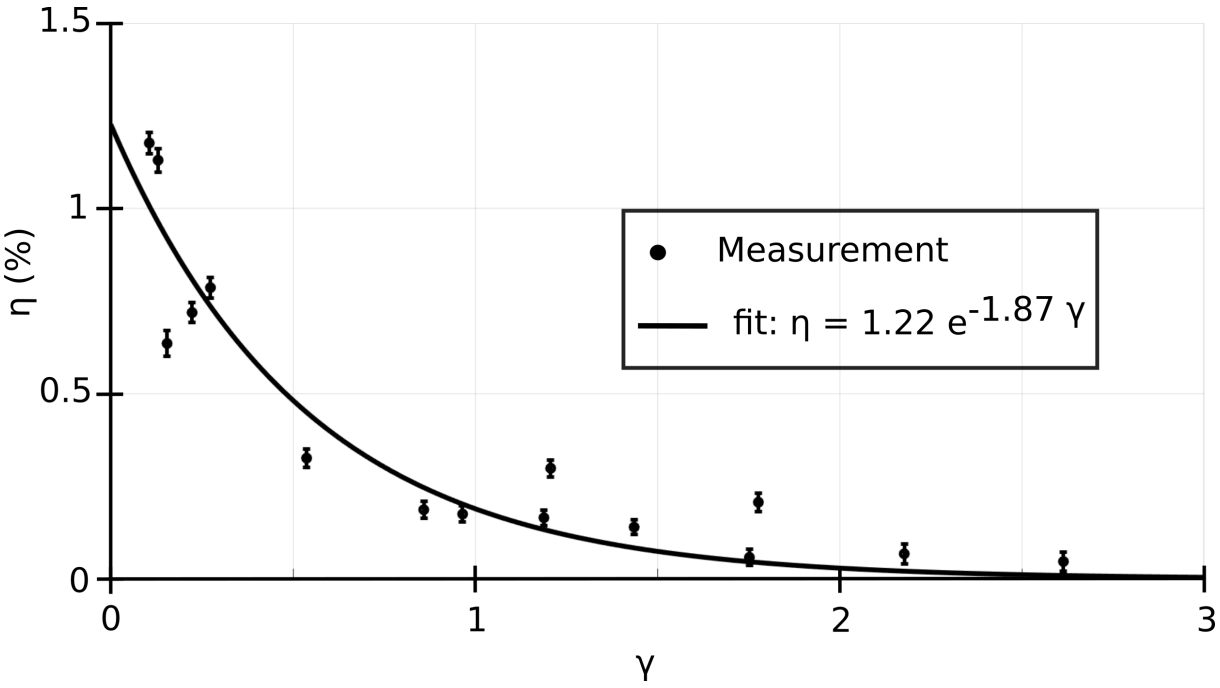

Figure 3.9: Shear generation efficiency plotted against the stand-off distance γ, reprinted with permission from Ref.[95]. An exponential curve fit of the form $\eta = a\ \exp(b\,\gamma)$ reveals that shear efficiency decreases exponentially with γ. The fitted parameters are $a = 1.22$ and $b = -1.87$, with a root-mean-square error (RMSE) of 0.1241.

This observation aligns with the expected behavior of spherically oscillating bubbles. A phenomenological fit of the shear generation efficiency is performed utilizing the function $\eta = ae^{b\,\gamma}$, where the parameters are defined as $a = 1.22$ and $b = -1.87$. The extrapolation of the fit suggests that, under this configuration, a maximum of $\eta(\gamma = 0) = 1.22\%$ of the bubble energy is convertible into shear energy for the specific gelatin concentration used in this study.

3.7 Shear stress confinement

In this section, we aim to explore the conditions for shear wave excitation and establish a link with the phenomenon of acoustic emission resulting from the absorption of laser light, commonly known as photoacoustics. Specifically, in the context of generating acoustic waves through impulsive laser-induced heating, it has been established that the duration of heating must be limited to a timeframe shorter than the stress confinement time, which denotes the time required for stress to propagate across the heating region in

the form of an acoustic pulse, as discussed by Choi *et al.* [119]. Consequently, the stresses can be build up, eventually released through a strong acoustic emissions. This condition, commonly known as stress confinement, can also be analogously applied to shear generation. In simple terms, if the duration of shear stress generation is shorter than the time it takes for shear wave to propagate out of the volume, shear stress will be confined. This concept can be quantified by considering the Rayleigh collapse time[111], denoted as $T_{\mathrm{C}} = R_{\max}\sqrt{\rho/\Delta p}$, where $R_{\max}$ is the maximum bubble radius, ρ is the density, and Δp is the pressure difference between the bubble interior and the ambient liquid pressure. Concurrently, the shear wave propagates out of the stress generation volume within a time $T_{\mathrm{SW}} = R_{\max}/V_s \approx R_{\max}\sqrt{\rho/E}$, with V_s representing the shear wave velocity and E denoting the Young's modulus. Shear stress confinement is then achieved when $T_{\mathrm{C}} < T_{\mathrm{SW}}$ or $T_{\mathrm{C}}/T_{\mathrm{SW}} = \sqrt{E/P} < 1$.

During maximum expansion, the pressure in the bubble is typically close to zero, allowing us to estimate the pressure difference as the atmospheric pressure, $\Delta P = 100\mathrm{kPa}$. For the current material with an approximate modulus of $E \approx 10\mathrm{kPa}$, the calculated value of $T_{\mathrm{C}}/T_{\mathrm{SW}} \approx 0.1$ is expected. This analysis suggests that shear stress confinement is more challenging to achieve in stiffer materials. As a result, in situations where tissue stiffness increases during treatment, such as in thermal ablation, the amplitude of the shear wave may diminish. Thus, monitoring the strength of emitted shear waves during thermal procedures can yield important information regarding the thermal dose absorbed by the tissue. Further exploration into shear wave generation as a function of tissue properties, particularly the elastic modulus, could be a promising avenue for future research.

3.8 Conclusion

In conclusion, this Chapter explores the generation and propagation of shear waves resulting from the non-spherical collapse of laser-induced cavitation bubbles in a TMM. The investigation, covering various stand-off distances, reveals that distinct shear wave patterns and dynamics, are associated with different bubble behaviors. Key findings and implications can be summarized as follows:

Shear Wave Generation Mechanisms: The study uncovers two primary mechanisms for shear wave generation. For larger stand-off distances, shear waves predominantly arise during the collapse phase, particularly in connection with the formation of axial jets. In contrast, for smaller stand-off distances, shear waves are generated both during bubble expansion and collapse, with a significant contribution from the region near the solid boundary.

Propagation Characteristics: The shear wave propagation exhibits particular patterns depending on the stand-off distance. Larger stand-off distances result in shear waves propagating predominantly parallel to the boundary, while smaller stand-off distances yield shear waves propagating in the vertical direction, perpendicular to the boundary. Intermediate distances exhibit a combination of both orientations.

Shear Wave Efficiency: The efficiency of shear wave generation, quantified as the ratio of shear wave energy to bubble energy, is systematically analyzed across various stand-off distances. The results indicate a maximum shear wave efficiency for small stand-off distances, highlighting the influence of bubble dynamics on shear wave generation. For spherical bubbles on the other hand, no shear wave will be released.

Connection to Tissue Properties: The study establishes a potential connection between shear wave excitation and tissue properties, particularly the elastic modulus. The analysis suggests that shear stress confinement, analogous to stress confinement in photoacoustic phenomena, may be a crucial factor influencing shear wave strength. This finding has implications for monitoring tissue changes, such as stiffening during thermal ablation procedures. The observed relationship between shear wave strength and tissue properties opens avenues for therapeutic monitoring, especially in procedures where tissue stiffness is altered. Monitoring the strength of emitted shear waves may provide valuable insights into the thermal dose received by the tissue during treatments like thermal ablation.

Chapter 4

Ultrasound imaging of cavitation-induced shear waves

The work presented in this chapter has been published in parts in J. Rossello, S. Izak Ghasemian, and C. D. Ohl. "High-speed ultrasound imaging of bubbly flows and shear waves in soft matter", Soft matter, vol. 20, no. 4, p. 823-836, 2024, see Ref. [120]. There I was the second author. My contribution to the publication was data curation, formal analysis, investigation, software development, visualization, conducting experiments together with the lead author, and drafting parts of the original manuscript.

4.1 Introduction

The conventional method for monitoring shear wave propagation in biological tissues involves utilizing high frame rate Ultrasound Imaging (USI), with frame rates higher than 1 kHz[121] within the region of interest. To achieve the necessary high frame rate, plane wave compounding is commonly employed. There, the received RF signals encapsulate information of the dynamically evolving speckle pattern—the granular pattern that emerges in ultrasound images due to the interaction of echoes with a large number of randomly dis-

tributed scatterers within the resolution cell[122]. This pattern undergoes frame by frame changes as the tissue experiences displacement due to the propagating shear wave and comparing the backscattered signal from two sequential frames, shear wave front could be localized. Widely employed in SWE, this technique provides valuable insights into the mechanical properties of tissues with measuring shear wave propagation speed[72–74]. The method is particularly advantageous for characterizing the stiffness of biological tissues, offering a non-invasive approach to assess pathological conditions.

After demodulating the recorded RF echoes from K different compounding angles, In-phase and Quadrature (IQ) data are formed which represents the in-phase (I) and quadrature (Q) components of the complex analytical signal, often obtained through quadrature demodulation[123]. After beamforming and summing the K different beamformed IQ from different angles, the compounded IQ for each frame is formed. In the subsequent phase, the compounded IQ data are employed directly for tissue motion estimation. One of the first successful algorithms for estimating tissue motion is the Kasai Algorithm[124]. Originally designed for measuring blood velocity using Doppler, the algorithm measures the average phase shift respecting the center frequency, to calculate the displacement between a reference and a displaced signal.

Another widely employed algorithm for displacement estimation is the Loupas autocorrelator[125]. Serving as an extension of the Kasai algorithm, the Loupas algorithm uses the information from depth samples within a specified axial range to compute displacement. A key distinction between the Kasai and Loupas algorithms lies in the way they take the carrier frequency data. The Kasai approach presumes a constant carrier frequency, whereas the Loupas algorithm computes the average Doppler frequency and the average RF frequency at each axial point. Essentially, the Loupas algorithm addresses local variations in the center frequency, thereby enhancing accuracy in displacement estimation[126]. Eq. 4.1 presents the final formulation for the axial velocity calculated by the Loupas algorithm.

$$v = \frac{c}{2}\frac{t_s}{T_s}\frac{\arctan\left(\frac{\sum_{m=0}^{M-1}\sum_{n=0}^{N-2} Q(m,n)I(m,n+1) - I(m,n)Q(m,n+1)}{\sum_{m=0}^{M-1}\sum_{n=0}^{N-2} I(m,n)I(m,n+1) - Q(m,n)Q(m,n+1)}\right)}{2\pi f_{dem} + \arctan\left(\frac{\sum_{m=0}^{M-1}\sum_{n=0}^{N-2} Q(m,n)I(m+1,n) - I(m,n)Q(m+1,n)}{\sum_{m=0}^{M-1}\sum_{n=0}^{N-2} I(m,n)I(m+1,n) - Q(m,n)Q(m+1,n)}\right)} \tag{4.1}$$

Here, the axial velocity v is measured across an axial range M and N different frames. c represents the speed of sound in tissue, t_s is the sampling period, T_s is the pulse repetition period, I and Q denote the in-phase and quadrature components of the IQ data, and f_{dem} represents the number of wavelengths of the center frequency per RF sample. The derived axial velocity corresponds to the displacement rate of tissue particles induced by the propagating shear wave. By measuring the axial velocity (v) from the demodulated IQ data using the Loupas algorithm, the shear wave's location is visualized in each frame. Tracking this location allows for the measurement of its local propagation speed within the region of interest.

In Chapter 3, the non-spherical collapse of cavitation bubbles was demonstrated to generate shear waves, with a particular emphasis on optical imaging. There, the exploration focused on explaining the underlying physics governing shear wave generation from the collapse of cavitation bubbles where a transparent TMM was employed to enable optical imaging. In this chapter, we broaden our investigation by presenting the high frame rate USI of shear waves generated from non-spherical cavitation bubble collapse within a soft solid. Additionally, we examine shear waves arising from the jetting phenomenon of a cavitation bubble penetrating into a soft solid using optical and ultrasound imaging.

4.2 Experimental setup and methodology: Shear wave generation from bubble collapse inside a soft solid

To mimic the mechanical characteristics of soft tissues, a gelatin mixture is prepared with a 4% mass ratio of gelatin to water, following the procedure outlined in Chapter 3.

The prepared gelatin is then carefully poured into a homemade cuvette with dimensions of $12 \times 12 \times 55$ mm^3. In our initial attempts, we observed that placing a thin layer of graphite within the gelatin, such as what we did for optical shear wave observation in chapter 3, did not produce sufficient scattering to generate the required speckle pattern for effective USI of the shear waves. Subsequently, we modified our approach by integrating graphite particles into the entire volume of the gelatin samples. This adjustment ensures a more effective scattering medium, enhancing the visibility of the shear wave in USI.

The experimental setup is illustrated in Fig. 4.1. A collimated pulsed laser is focused into the gelatin sample from below using a microscope objective (Olympus 10 Plan Achromat, NA = 0.25). By focusing the laser energy near the lower boundary, a cavitation bubble forms within the focal area of the objective, leading to the subsequent non-spherical collapse of the cavitation bubble and the generation of a shear wave, as detailed in Chapter 3.

The propagating shear wave is captured using a high-speed camera (Photron, FASTCAM Mini, AX200) coupled with a macro lens (Canon MP-E 65 mm f/2.8 $1-5\times$ Macro) and the Verasonics ultrasound system connected to ATL L7-4 (center frequency of 5MHz). Both imaging systems operate simultaneously, with the ultrasound system having a sampling rate of 62.5 MHz. For the data acquisition, the ultrasound system records RF echoes from $K = 3$ different angles at $-10°$, $0°$, and $+10°$. To enhance image quality, compounding is performed by acquiring data from these multiple angles. The timing of the laser, the high-speed camera, and the ultrasound system is precisely synchronized through the use of a digital delay generator (BNC 525, Berkeley Nucleonics).

4.3 Shear wave visualization using graphite particles as trackers

The same PIV technique presented in Chapter 3 is applied here to visualize the propagating shear wave recorded by the high-speed camera. It is essential to note that due to the presence of graphite particles throughout the entire volume, laser focusing inside the

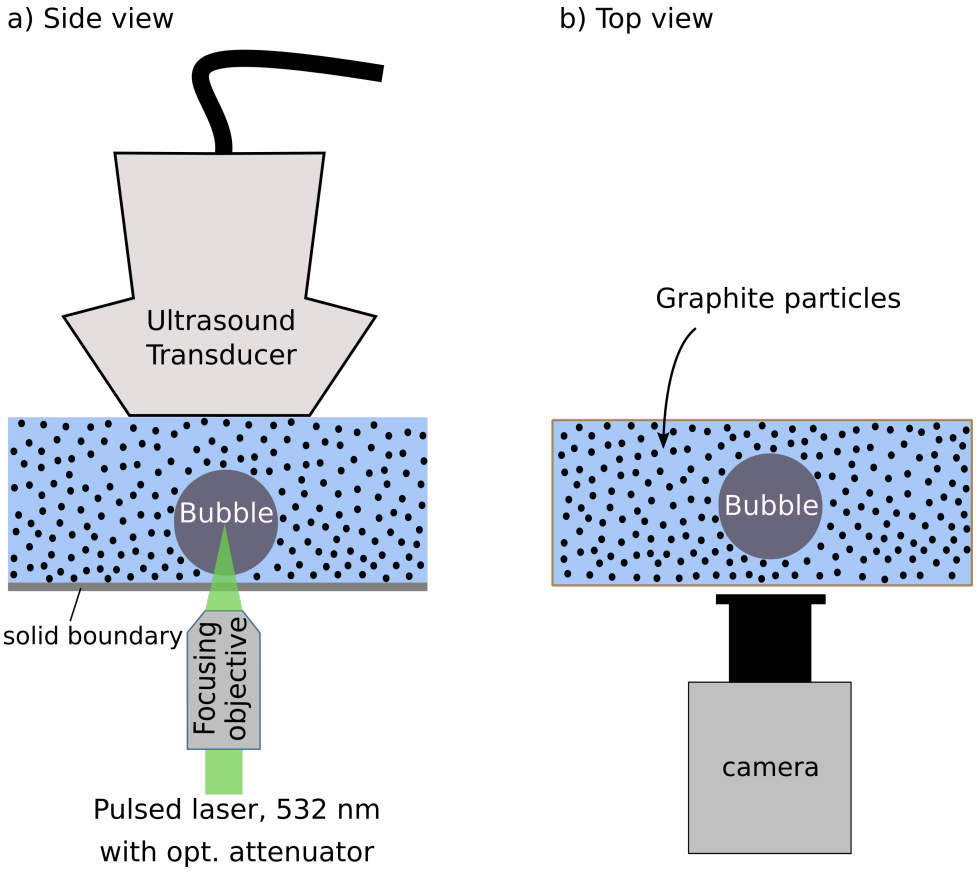

Figure 4.1: Experimental setup for optical and ultrasound imaging of shear waves generated by laser-induced cavitation bubbles in a tissue mimicking material. a) Side view: The bubble is generated near the lower wall of the cuvette, undergoing non-spherical collapse and initiating a shear wave. b) Top view of the setup with the bubble generated in the center of the cuvette, producing a shear wave captured by the high-speed camera.

samples, far away from the solid boundary, was not feasible. Consequently, cavitation bubbles with very small stand-off distances γ were the only ones that could be generated in this case. Fig. 4.2 showcases a sequence of PIV visualized images, where an upward propagating shear wave is observed, similar to what was observed in Chapter 3 for cases with small stand-off distances.

The recorded ultrasound data is used to visualize the propagating shear wave using the Kasai algorithm with a frame rate of 7250 fps. A selected sequence of frames is presented in Fig. 4.3, where the cavitation bubble is created in the lower left corner of the imaging window, and the ultrasound transducer is positioned from the top. Following the collapse of the bubble towards the lower wall of the cuvette, two shear waves propagate through the medium, with only the right-hand wave being imaged to capture a more extended propagation distance. The gray colormap image indicates the axial velocity of particles,

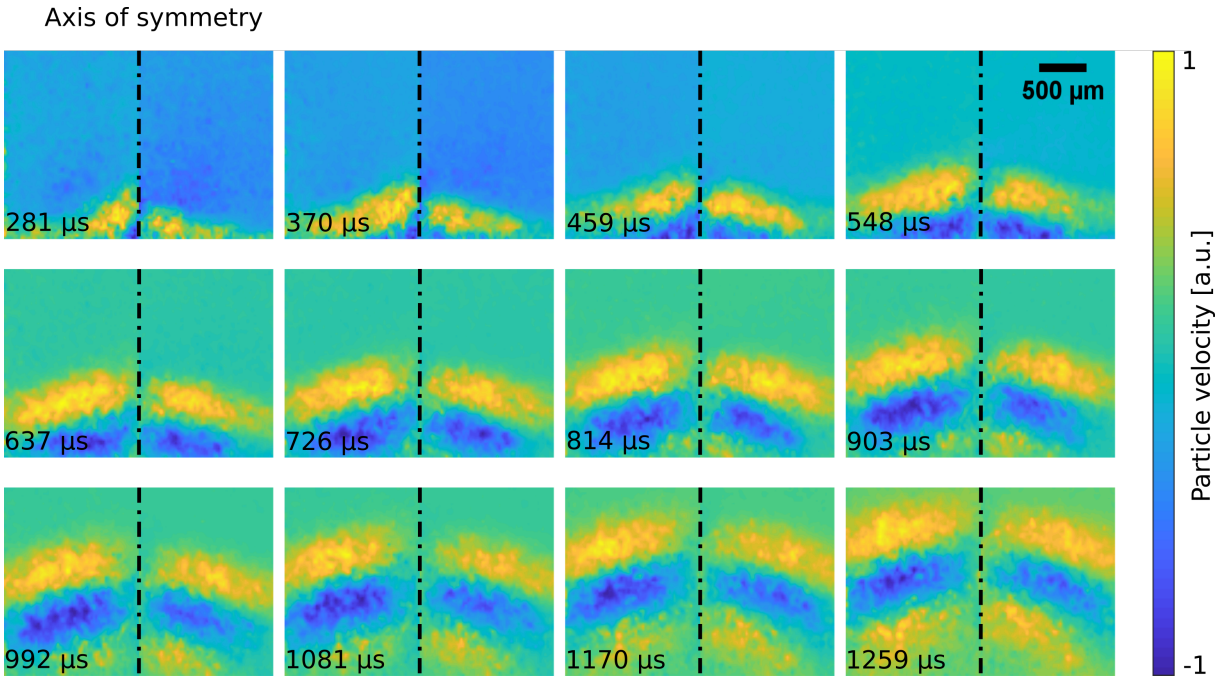

Figure 4.2: PIV visualized image sequence illustrating shear wave propagation resulting from non-spherical collapse of a cavitation bubble with $\gamma = 0.23$. The predominant direction of shear wave propagation is upward, consistent with our earlier observations in Fig. 3.5 for the small γ case.

with brighter spots indicating higher axial velocity.

It is essential to note that detecting the horizontal velocity of the particles in this formulation is challenging as the Kasai algorithm measures only the axial velocity. As previously discussed in Chapter 3 and also visible in Fig. 4.2, the shear waves generated from small γ cases propagate vertically, causing the particles to oscillate horizontally. Consequently, it becomes difficult to capture shear waves generated from small stand-off distances in this configuration and the captured shear waves with ultrasound lack sharpness, and bright spots in the images are primarily in regions where the shear wave induces axial velocity. Additionally, as discussed earlier, the presence of particles in the bulk volume of the sample complicates the generation of bubbles with larger γ cases.

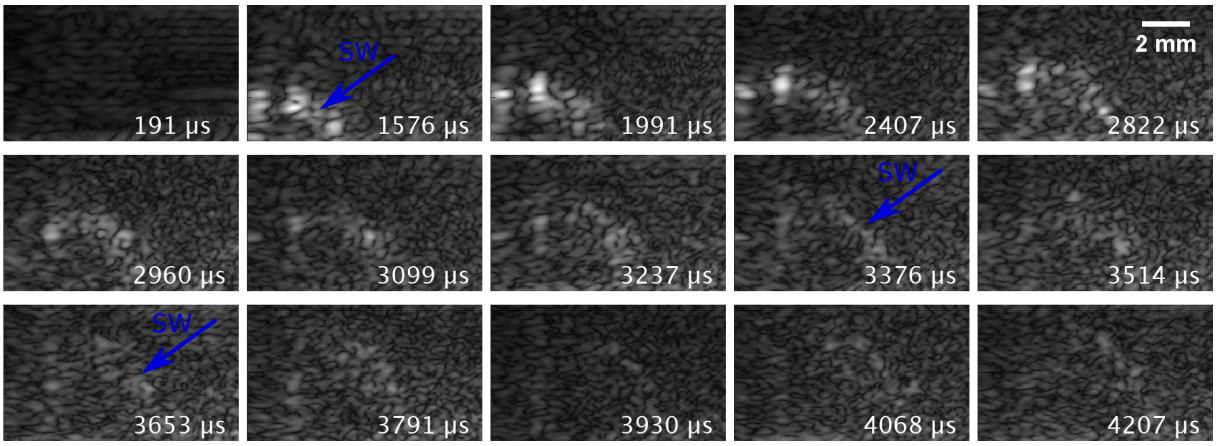

Figure 4.3: Time evolution of the shear wave induced by bubble activity generated through laser breakdown, captured by plane wave compounding ultrasound imaging with 3 different angles. The shear wave front ("SW") is visible as bright spots, highlighted by the blue arrow.

4.4 Shear wave visualization using bubbles as trackers

Initially, placing the graphite particles in a thin layer similar to what we did in Chapter 3, failed to generate the desired ultrasound speckle pattern, resulting in poorly detectable shear waves. To address this limitation, we opted for a different strategy—dispersing the particles uniformly throughout the entire volume of the gelatin. This adjustment increased the scattering effect, significantly improving the visibility of shear waves in USI. However, this solution brought about a new challenge: the inability to generate cavitation bubbles far from the solid wall. The laser energy, utilized for bubble generation, was absorbed by the graphite particles, hindering its penetration deep into the gelatin sample. This limitation restricted the stand-off distance, allowing only the small γ values for the generation of shear waves induced by bubbles.

Drawing inspiration from our observations in Chapter 2, where bubbles proved to be effective scatterers for USI without the necessity for compounding, we revisit our approach. Considering the efficiency of bubbles as scatterers in ultrasound, we explore the feasibility of utilizing small gas pockets as tracers for shear wave visualization. In this approach, we introduce small bubbles into a targeted layer instead of using particles, intending to leverage their ultrasound scattering properties to track shear waves.

To introduce small gas pockets as tracers into the gelatin samples, we leverage the residual bubbles previously demonstrated in Chapter 2. As established in that chapter, following the collapse of the cavitation bubble in gelatin—distinct from water—a small gas bubble persists in the sample for a rather long time. In the current context, after laser focusing and shooting in the gelatin sample, a residual small gas bubble endures after a few oscillations of the cavitation bubble. Subsequently, by systematically moving the cuvette in a linear pattern and triggering the laser at each step, a series of gas pockets are generated along a trajectory. Repeating this process for multiple lines results in the formation of a layer comprising small gas bubbles, serving as tracers for tracking the propagating shear wave in the next step.

The setup depicted in Fig.4.1 is employed for the new samples as well. The only difference is that instead of having graphite particles in bulk, there is only a layer of gas pockets. In Fig.4.4, the resulting bubble pattern is shown, featuring tracer bubbles with an approximate radius of 50μm. A laser-induced cavitation bubble is generated near the solid wall, and the resulting shear wave is captured using USI.

Figure 4.5 illustrates a frame of the propagating shear wave reconstructed using the Kasai algorithm where Fig. 4.5a depicts the result obtained through compounding with three angles ($-10°$, $0°$, and $+10°$) and Fig. 4.5b shows the outcome with a single plane wave at $0°$. Remarkably, with using bubbles as tracers instead of graphite particles, not only a layer of trackers is enough to capture shear wave propagation using ultrasound, but it also eliminates the necessity for compounding and a single plane wave is enough to capture the shear wave dynamics. Notably, both images reveal a similar pattern, showcasing the effectiveness of shear wave capture with a single plane wave without the need for angle compounding using gas cavities as tracers. This approach results in a higher frame rate for capturing shear wave propagation through the medium. Alternatively, for the same frame rate, it enables deeper imaging into tissues using a single plane wave instead of plane wave compounding.

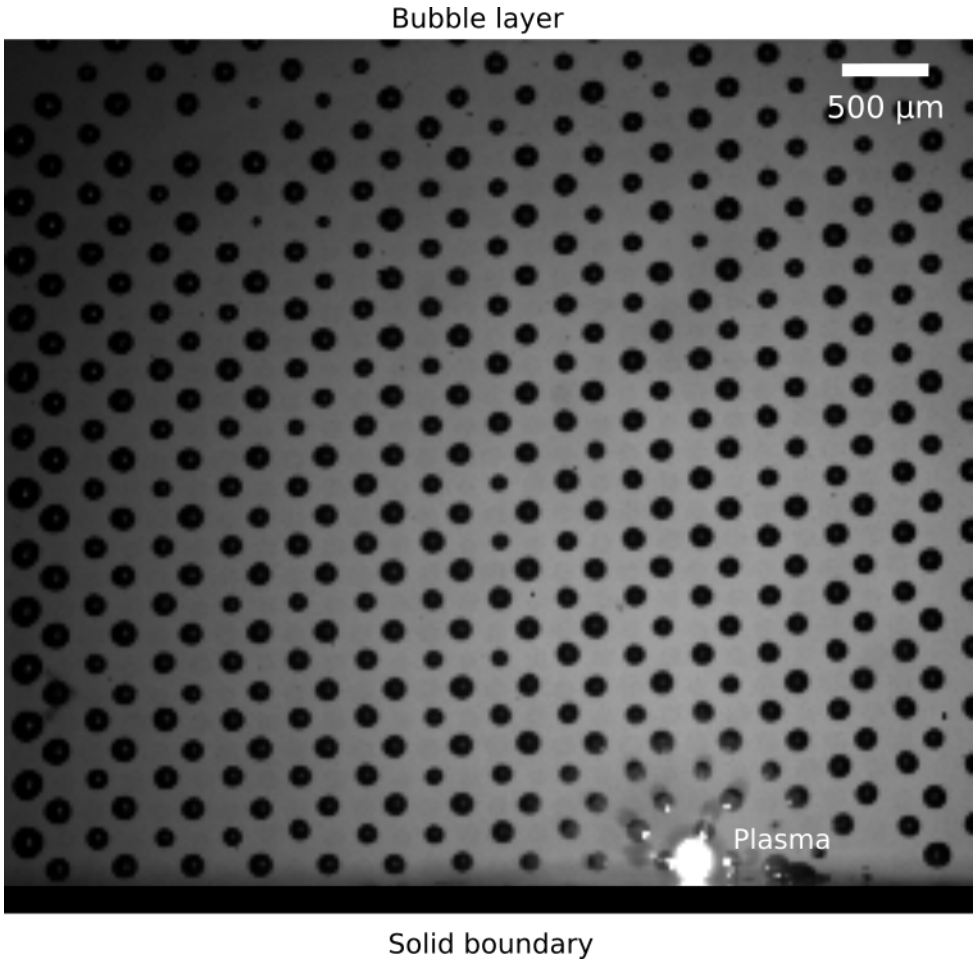

Figure 4.4: Utilizing bubbles as tracers to visualize shear waves through ultrasound imaging where the ultrasound transducer is positioned from the top. In the laser's focal region, where plasma forms, a cavitation bubble is initiated, undergoing non-spherical collapse near the solid boundary. This process gives rise to a propagating shear wave within the domain, and its movement is tracked by ultrasound imaging through the presence and motion of the tracer bubbles.

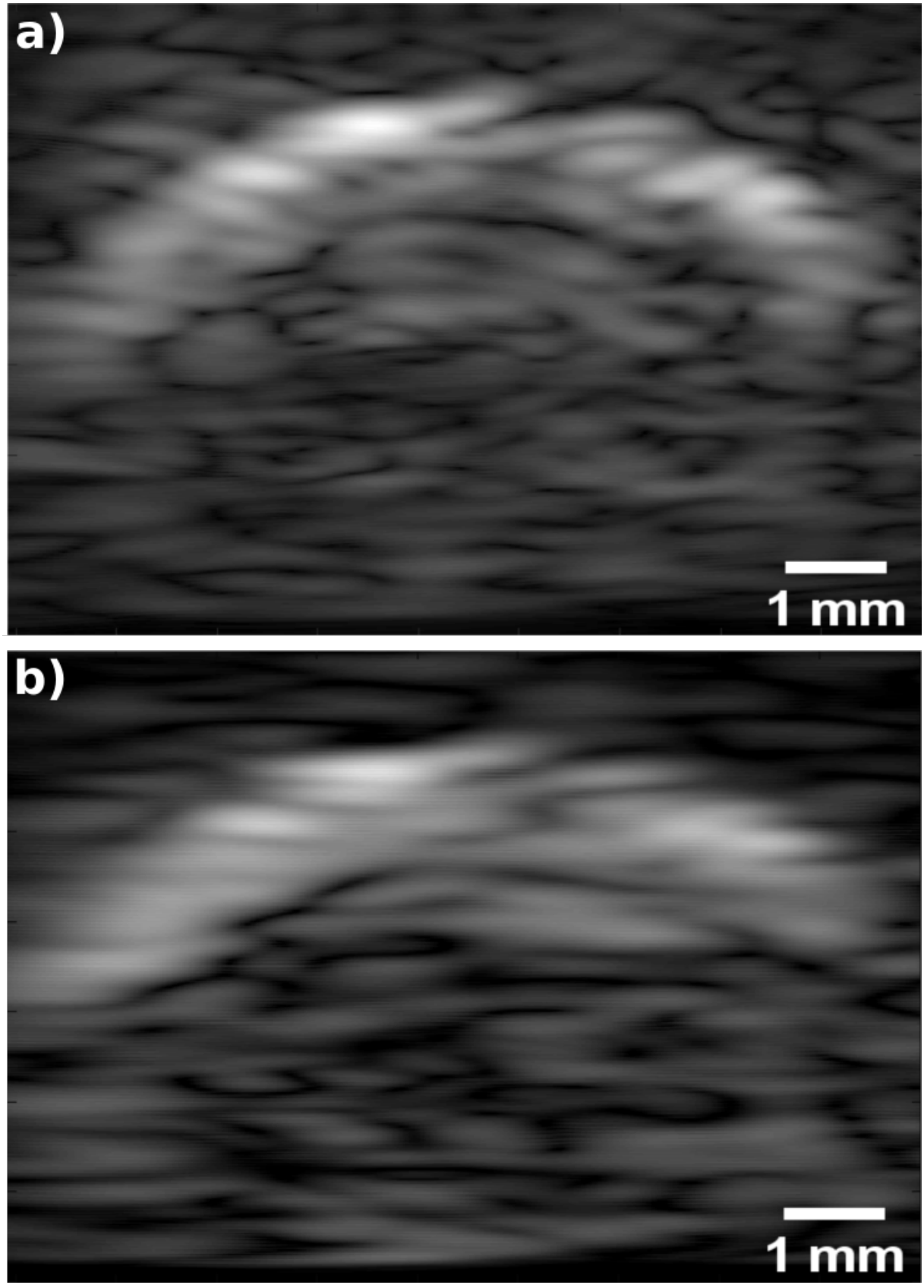

Figure 4.5: Ultrasound imaging captures the shear wave generated due to cavitation activity, using a layer of gas cavities as tracers. (a): Utilizing plane wave compounding with 3 angles, reaching a frame rate of 8100 fps. (b): Employing single ultrasound plane wave imaging at a frame rate of 24300 fps.

4.5 Experimental setup and methodology: Shear wave generation from bubble jetting

After exploring the generation of shear waves arising from the non-spherical collapse of cavitation bubbles inside soft solids, we now study the same effect on the surface of a soft solid using high-speed optical and USI techniques. Specifically, we cover a block of gelatin with a 1mm thick layer of water and hit the water layer with a focused pulsed laser at varying depths d relative to the water surface. This, results in the development of a laser-induced bubble, which evolves into different types of liquid jets depending on the depth of the laser focus point, as discussed in Ref. [120]. The jet then penetrates the surface of the gelatin block and moves downward, generating shear stresses that propagate radially from the injected liquid column.

The experimental setup for the optical and ultrasound detection of shear waves generated from jetting into the soft solid is outlined in Fig. 4.6. The central component of the experiment includes an open rectangular cuvette with internal dimensions of 76mm in length $\times$ 12mm in width $\times$ 13.5mm in height, with transparent 1mm glass walls on all lateral sides. The ultrasound transducer comes from bottom of the cuvette, which is securely sealed at the base using a thin layer of low-density polyethylene film, maintaining contact with the transducer through a fine layer of ultrasound transmission gel. Integrated into the Verasonics system, the transducer operates at a central frequency of 5 MHz for USI. The use of a slim low-density polyethylene film at the base ensure an effective seal for the cuvette without impeding the transmission and reception of ultrasound signals. The optical recordings are acquired at a frame rate of 25 kfps, utilizing a Shimadzu XPV-X2 camera connected to a LAOWA 60 mm $f/2.8$ macro lens.

In line with the previous experiment studied in Section 4.4, we utilize bubbles as tracers in this experiment as well. However, instead of intricately seeding bubbles in a layer, we employ an alternative method for bubble generation. Here, an unfocused pulsed laser with a maximum pulse energy of approximately 51mJ illuminates the volume parallel to the array of transducer elements, creating a cluster of numerous Bulk Laser Bubbles (BLB)s

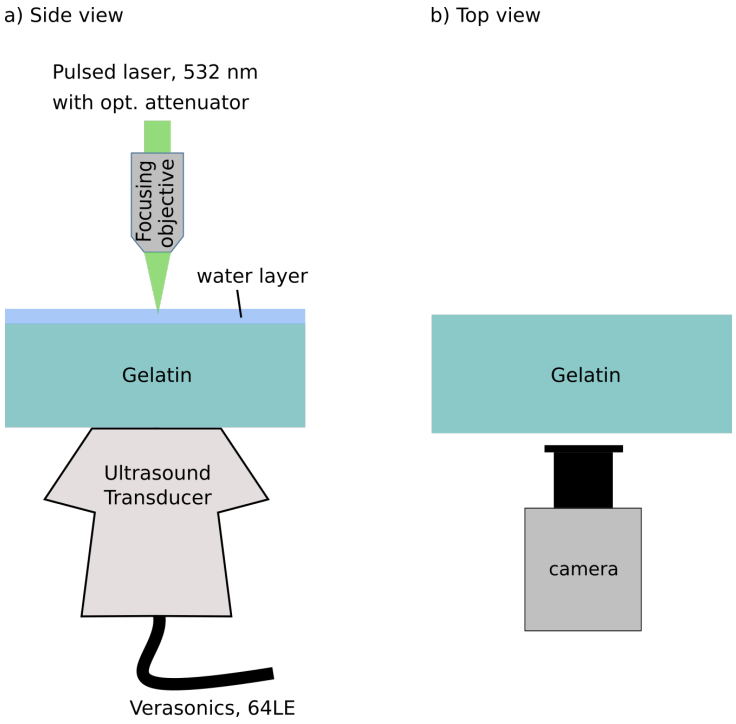

Figure 4.6: Experimental setup employed for the investigation of shear waves through ultrasound imaging and high-speed video recordings simultaneously. The primary component of the system consists of a rectangular cuvette with clear glass walls on four sides, an open top, and a sealed bottom created by a thin polyethylene film that is linked to the ultrasound transducer for imaging purposes. Tracer bubbles are produced by projecting an unfocused collimated laser pulse onto the gelatin in the cuvette, aligned parallel to the surface of the ultrasound transducer. A second green laser pulse was concentrated just beneath the liquid surface, leading to the formation of a cavity that evolved into a downward-directed jet within the 4% gelatin block, covered by a fine layer of water.

with a diameter below the pixel size, i.e. 6μm. The process follows the approach outlined in References [127, 128]. In this setup, the Gaussian laser beam diameter is achieved through two consecutive lenses with focal distances $L_1 = 100$ mm and $L_2 = -25$ mm, spaced approximately 75mm apart. The beam is then clipped with a pinhole, resulting in a final diameter of 1 mm. The gelatin samples are infused with graphite particles. Initially invisible in optical images, the BLBs can eventually reach a diameter of approximately 1mm after a few minutes. In this context, the particles function as trackers in optical PIV, and the bubbles play a similar role as contrast agents in USI.

4.6 Effect of different jets on shear wave propagation in soft solids

Figure 4.7 presents a comparison of shear waves in gelatin generated by a single laser-induced bubble alongside three different types of piercing jets. The examination of shear waves, performed immediately after the liquid attains its maximum depth, employs both optical PIV (second column) and ultrasound (right column) to monitor particle displacement. The observations indicate that stronger jets, which penetrate deeper into the gelatin, lead to an increase in shear wave amplitude and cause the wave front to change from a spherical to a cylindrical shape, originating at the interface between the penetrating liquid and the gelatin. The results in Fig. 4.7 demonstrate strong agreement between the optical and ultrasound techniques. Furthermore, it is disclosed that the peak particle velocity within the gelatin and the amplitude of shear wave oscillations are significantly greater for all piercing jet scenarios in comparison to the spherical shear waves produced by a point source when the bubble is directly introduced into the gelatin, as illustrated in Fig. 4.7(a).

The particles and BLBs are restricted to a 1mm thick observation plane, and due to the restricted focal depth in the optical images, the displacement measurements in both the PIV analysis and USI are predominantly unaffected by shear wave components propagating out of the plane of view. This ensures a high degree of consistency between the two measurement methods. Additionally, the PIV images indicate that the bubbles are much smaller than the apparent wavelength of the deformation waves, causing them to shift with the wavefront without significantly distorting it.

With investigating the radial propagation of shear waves, it becomes apparent that their oscillatory characteristics are consistently similar, regardless of the jet type or penetration depth. This is evidenced by the temporal evolution of material displacement recorded by USI, as displayed in Fig. 4.8. The plotted curves illustrate the average particle velocity within the red-outlined regions in the examples provided in Fig. 4.7. This analysis confirms the connection between the oscillation amplitude of the shear waves and

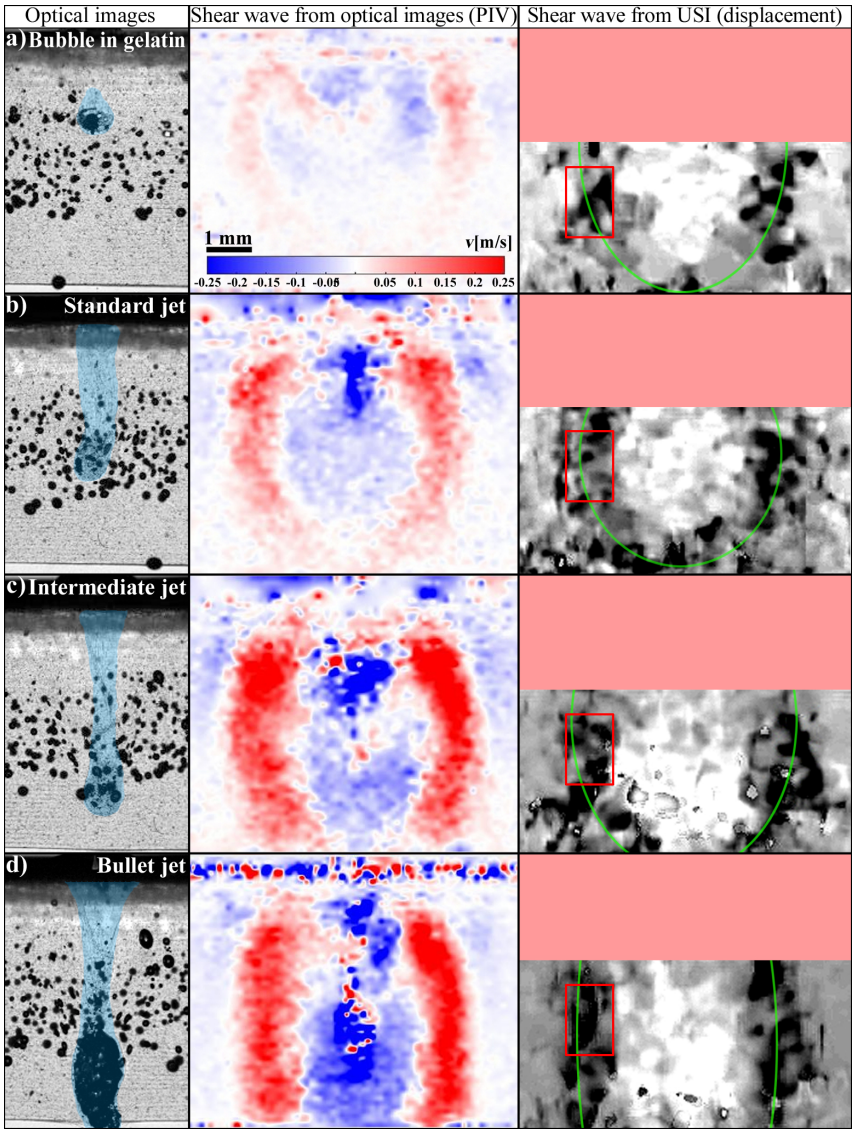

Figure 4.7: Concurrent optical and ultrasonic imaging of shear waves produced by a laser-induced bubble (a) and three distinct jet configurations (b-d), reprinted with permission from Ref.[120]. The illustrated scenarios comprise: (a) a single laser bubble created roughly $\sim 1\,\mathrm{mm}$ below the gelatin surface, (b) a "Standard" jet, (c) a "Intermediate" jet, and (d) a "Bullet" jet. The first column presents an optical image depicting the bubble or jet at its greatest penetration depth, with the injected liquid highlighted in light blue. The second column depicts a PIV image of the fully developed shear wave, whereas the third column presents ultrasound displacement data related to the wave. Both PIV and USI illustrate the mean vertical displacement across three frames centered at $t = 2.5 \pm 0.2\,\mathrm{ms}$. The optical frames utilized for PIV were captured at a frame rate of 25 kfps, but USI functioned at an effective frame rate of roughly 5.5 kfps. To improve the visualization of the shear waves, the contrast in the USI photos was altered arbitrarily. The surface region was omitted from the study to prevent interference from intense reflections that might conceal the shear wave signal. The area examined in Figure 4.8 is delineated by a red border.

the jets' penetration depth.

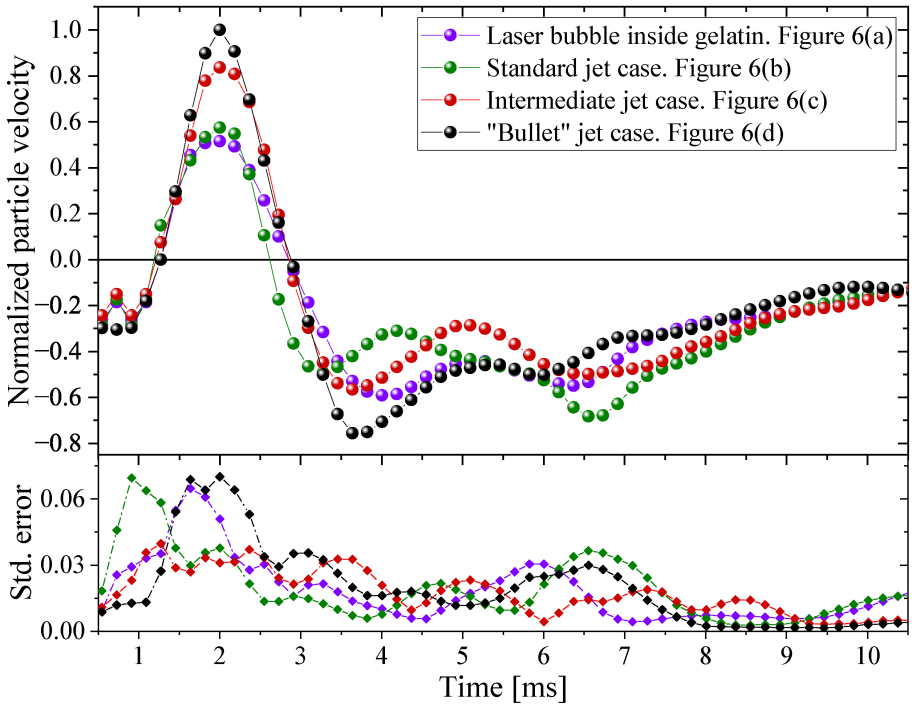

Figure 4.8: The temporal evolution of ultrasonic particle displacement velocity resulting from shear waves generated by different forms of jetting bubbles, as depicted in Figure 4.7, reprinted with permission from Ref.[120]. Each curve illustrates the averaged velocity profiles inside the red-bordered area in the third column of that figure. The velocities are normalized by the greatest displacement rate recorded for the bullet jet and a downward movement is set as positive. To facilitate the comparison of shear waves, the temporal references of the curves were adjusted to align the displacement peaks, considering the varying timings of the jets.

The consistency in the behavior and shear wave propagation speed across different jet types demonstrates the effectiveness of this technique for examining the rheological properties of opaque materials or in conditions with limited optical accessibility. The results of elastography evaluations are predominantly unaffected by fluctuations in the depth of laser focus or the exact quantity of water applied to the soft material. However, generating BLBs in opaque materials presents a significant challenge due to the limited penetration depth of lasers in such media. While this thesis effectively visualizes shear wave propagation using BLBs as tracers in transparent or semi-transparent materials, extending this approach to fully opaque materials may require further developments, such as alternative methods for bubble generation or deeper-penetrating laser systems.

4.6.1 Shear wave generation from bullet jet

Figure 4.8 further supports the idea that bullet jets are the most efficient jets for producing strong and uniform wave fronts. These characteristics are influenced by the jet's penetration depth, which can be scaled by keeping a consistent ratio between the laser cavity size (determined by the pulse energy) and its seeding depth. With this consideration in mind, the focus will now shift to the jet piercing mechanism and the specifics of shear wave generation, concentrating solely on the bullet jet scenario. These two features are examined in further depth in Fig. 4.9, utilizing PIV images acquired from high-speed video recordings of a bullet jet. The penetration dynamics are depicted in the first frames of the sequence. The upper section of the gelatin is affected by the downward jet generated by the collapse of the laser cavity in the liquid phase. The influence of the liquid column on the gelatin creates a high-pressure region, squeezing the gelatin surrounding the jet tip. The localized overpressure displaces the gelatin, causing the liquid column to go downward. This force stretches the soft material perpendicular to the jet's path, ultimately resulting in the gelatin's fracture and facilitating the liquid's penetration. Significantly, following the jet tip's passage through a designated segment of the gelatin, the previously downward-compressed material is now elevated, as evidenced by the blue region in the PIV sequence. The compression, fracturing, and release pattern observed in the bullet jet is similarly evident in the standard and intermediate jets depicted in Fig. 4.7(b) and (c). Ultimately, as the jet decelerates upon reaching its maximum penetration depth, the shear stresses confined within the material are released, generating shear waves [129, 130]. These waves are already observable in the final frames of Fig. 4.9 indicated in red.

Figure 4.10 depicts the monitoring of the wave front produced by a bullet jet for a longer time, employing both PIV methodologies derived from optical pictures and displacement tracking from ultrasound images. Upon emission, the cylindrical shear wave front traverses the gelatin phantom with minimum distortion, except for the interaction with its own reflection from the free surface, visible in the upper part of the final frames in both sequences depicted in Fig. 4.10. The integration of PIV analysis with optical images demonstrates that the existence of BLBs does not alter the wave front. This is evident

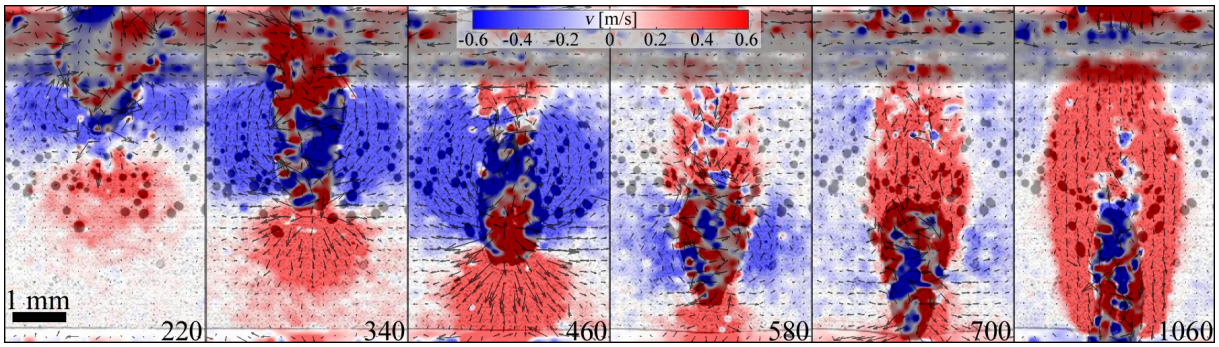

Figure 4.9: The dynamics of the bullet jet penetration were analyzed using PIV, with the color bar indicating the vertical velocity component, reprinted with permission from Ref.[120]. The labeled numbers denote the time elapsed in μs following the laser pulse directed at the top liquid layer.

when comparing the propagation dynamics in the central region, heavily populated with bubbles, and the lower region, which is practically devoid of bubbles.

The shear wave is observable over distances spanning the entire length of the ultrasound transducer, which is about 20mm. Since the dimensions of the bullet jets are proportional to the laser cavity size [131], and also as larger jets would produce stronger shear wave fronts, it is feasible to adjust the volume of soft material being analyzed by adjusting the region of interests for shear wave propagation monitoring. This approach facilitates the investigation of shear wave propagation within constrained volumes, enabling "real-time" elastography in highly localized areas which is especially useful for identifying tissue anomalies and evaluating the mechanical properties of soft materials.

A method for accurately measuring the propagation speed of shear waves V_s entails the creation of a particle velocity map, as depicted in Fig. 4.11. The maps, obtained from both PIV data and USI, illustrate the mean particle velocities (v) along vertical pixel lines across a horizontal band situated 1.7mm to 4.7mm below the gelatin surface. The selected Region Of Interest (ROI) was determined by the horizontal propagation direction of the wave fronts across all jet types (see to Fig. 4.7), rendering it ideal for monitoring the peak position of the deformation velocity. The outcomes illustrated in Fig. 4.11 correspond to the optical image sequence depicted in Fig. 4.10.

The particle velocity maps demonstrate a constant shear wave propagation speed V_s. Consequently, by fitting lines to the points of maximum amplitude within the map, sepa-

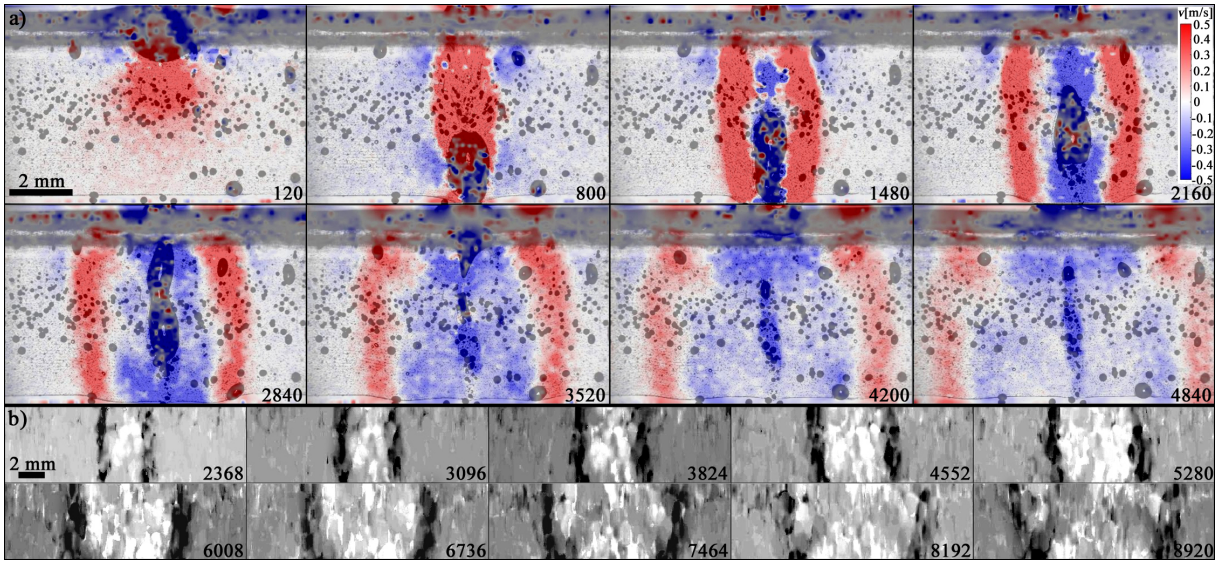

Figure 4.10: Shear wave generation and propagation induced by a high-speed "bullet" jet penetrating into gelatin, reprinted with permission from Ref.[120]. The vertical shear stress imparted by the jet, propagates laterally through the soft solid as a shear wave. Graphite particles incorporated in the gelatin serve as trackers for optical shear waves propagation studies using a PIV method, whilst gas pockets enable us for wave tracking via ultrasound imaging. a) Vertical velocity map obtained from PIV data, overlaid on high-speed optical images recorded at a frame rate of 25 kfps. b) Ultrasound imaging of shear waves, captured at a frame rate of 5.5 kfps, utilizing a 2-D autocorrelation method on the ultrasound data. Similar to Figure 4.7, the near-surface region is excluded from the USI data.

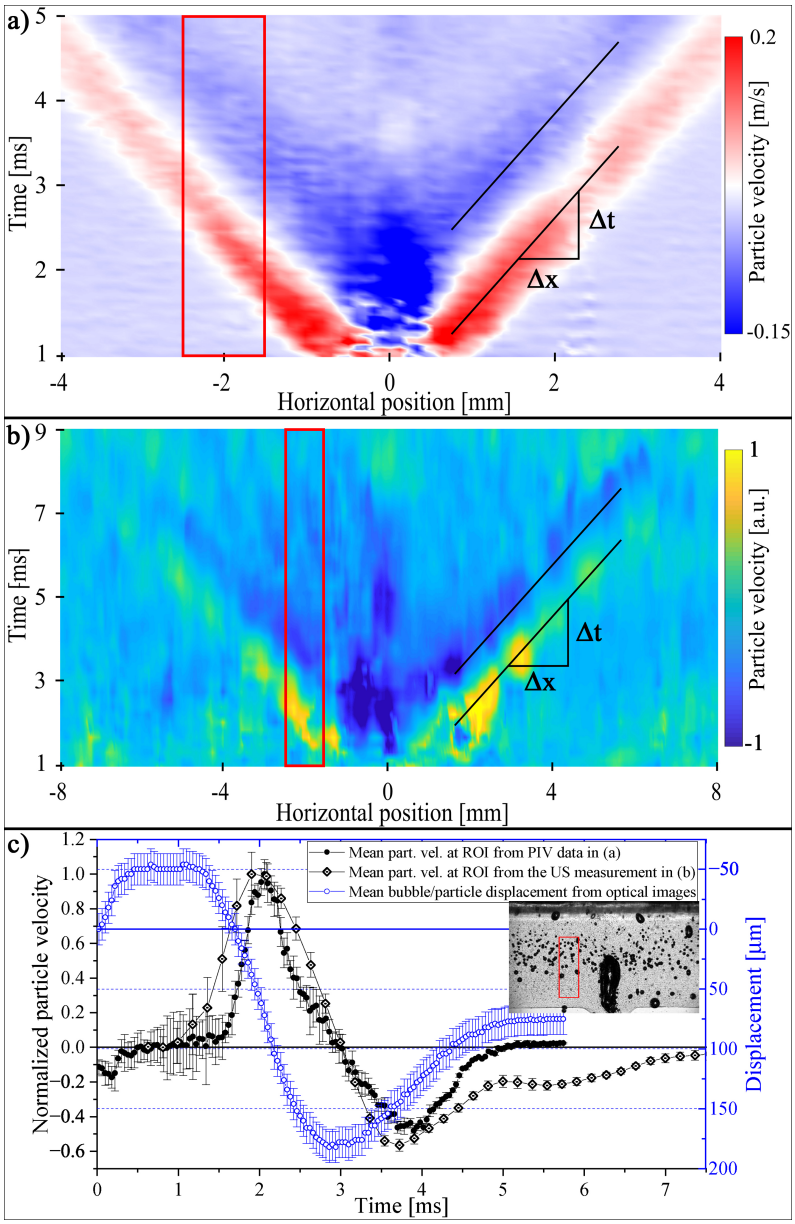

Figure 4.11: Vertical component of the particle velocity mapped against horizontal position and time, averaged over a depth range from 1.7 to 4.7 mm below the gelatin surface, reprinted with permission from Ref.[120]. Positive velocities indicate downward mobility, with $x = 0$ denoting the bubble's center on the horizontal axis and $t = 0$ representing the moment of bubble nucleation. a) Velocity map obtained from PIV applied to high-speed optical pictures, with a spatial resolution of 25.3 μm per pixel and a temporal resolution of 40 μs. The red zone signifies the shear wavefront, whereas the blue area denotes negative velocity. b) A map generated from the axial velocity field utilizing the Loupas 2-D autocorrelator applied to the ultrasound data. The velocity field is displayed in normalized format. The shear wave propagation velocity is determined by fitting a line to the peak displacement velocity recorded in the particle velocity maps, resulting in $V_s = 0.91 \pm 0.01$ m/s from the PIV approach and $V_s = 0.89 \pm 0.03$ m/s from the USI. c) Averaged velocity field along the x-coordinate inside the interval designated between 1.5mm and 2.5mm, as indicated by the red box in a) and b). The assessed area is also depicted in the inset of c).

rately for the leftward and rightward propagating waves, V_s can be accurately estimated. For the bullet jet illustrated in Fig. 4.11, V_s is calculated $0.91 \pm 0.01\,\mathrm{m/s}$ from the PIV data and $0.89 \pm 0.03\,\mathrm{m/s}$ from the USI. Moreover, the decay rate of particle velocity can be derived from these maps. Figure 4.11(c) illustrates the displacement caused by the shear wave traversing the specified section of the gelatin block, as depicted in the inset. The graphic depicts the temporal progression of particle velocity derived from the red-highlighted ROI in both the optical (a) and US displacement (b) maps of Fig. 4.11. The sharper peak in the optical data compared to the ultrasound data suggests that the PIV method provides superior spatial resolution relative to the acoustic technique.

These findings illustrate that even a modest presence of bubbles within the gelatin medium is adequate for characterizing shear wave behavior and determining its velocity using ultrasound. In our experiments, we observe an approximate density of 5 bubbles per square millimeter, with an average cavity radius of 76.3μm. Employing the same analytical approach outlined in Fig. 4.11, we process all available data. The average propagation velocities for each jet type is as follows: $V_{sj} = 0.95 \pm 0.5$ m/s for the standard jet, $V_{ij} = 0.92 \pm 0.5$ m/s for the intermediate jet, and $V_{bj} = 0.96 \pm 0.5$ m/s for the bullet jet.

4.7 Conclusion

In this chapter, we detail an experimental setup to visualize shear wave propagation using ultrasound techniques. Initially, shear waves are generated via the non-spherical collapse of cavitation bubbles inside a soft solid. By integrating graphite particles throughout the gelatin, we successfully visualize shear waves using both optical and ultrasound techniques. Additionally, we demonstrate that using bubbles as tracers instead of graphite particles eliminates the need for complex angle compounding, allowing for higher frame rates.

Furthermore, we investigate shear wave generation from bubble jetting, extending our study to include shear waves produced by liquid jets impacting the surface of the gelatin. Comparative analysis between shear waves generated by different types of jets reveals that stronger jets, which penetrate deeper into the gelatin, result in higher amplitude shear

waves and altered wavefront shapes.

Our findings underscore the potential of these methodologies for examining the mechanical properties of soft materials and tissues. They offer insights into the interaction between cavitation dynamics and shear wave propagation. This work lays a foundation for further exploration and optimization of shear wave elastography techniques, particularly in contexts where optical access is limited. It emphasizes the utility of combining optical and ultrasound imaging for comprehensive material characterization.

Chapter 5

Cavitation Induced Shear Wave Rheometry

5.1 Introduction

The characterization of soft materials plays a pivotal and intricate role in various research and engineering applications[132], particularly within the field of biomedical engineering, where the mechanical properties of soft tissues are closely associated with their physiological functionalities. However, characterizing soft materials presents challenges due to time-varying, inhomogeneity, and strain rate dependency of their mechanical properties. Traditional techniques measure bulk material properties under quasi-static loads. For example, approaches such as the split Hopkinson pressure bar and Taylor impact test are suggested for high strain-rate measurements; however, their applicability to soft matter is limited [132–134].

Another interesting method for characterizing soft solids involves utilizing cavitation to measure tissue properties. One such approach is the use of Cavitation Rheology Technique (CRT)s, which generate a cavity in soft matter through needle injection [135–137]. This technique, assessing the critical pressure of mechanical instability, is cost-effective

and minimally invasive. However, its application for measuring the high strain rate elastic modulus is limited due to the injection speed. Another method involves using an existing residual bubble in soft materials[92]. In this approach, the mechanical properties of the soft material can be estimated by observing bubble motion under an acoustic radiation force [138–140]. Yet, this method is constrained to materials under dissolved gas supersaturation, where the residual bubble remains stable for a relatively extended period. Other techniques that use cavitation to measure tissue properties include IMR, which is capable of characterizing soft materials at various strain rates [141, 142] (see Section 1.3).

As demonstrated in Chapters 3 and 4, the non-spherical collapse of cavitation leads to the generation of shear waves. Inspired by shear wave elastography techniques, this chapter introduces a methodology termed Cavitation-induced Shear Wave Rheometry (CSWR), where the measurement of shear wave propagation speed is employed to assess the elasticity of a TMM. Here we use photoelastic imaging—an optical technique for capturing shear wave propagation in soft solids—while keeping in mind that the same approach can be applied using optical PIV and ultrasound techniques discussed in previous chapters.

5.2 Photoelastic imaging

Photoelastic imaging is a non-destructive technique primarily used to visualize and analyze stress and strain distribution in transparent materials subjected to mechanical loads or deformations. The technique is based on the photoelastic effect, which exploits the phenomenon of birefringence to study stress in materials. Birefringence refers to the property of certain transparent materials to either naturally exhibit double refraction or temporarily develop it when stressed[143]. The temporary form of birefringence, commonly utilized in photoelasticity, is especially prominent in specific polymers and plastics that are optically isotropic in their unstressed state. When these materials are stressed, they become optically anisotropic, causing light to split and propagate along two distinct paths with different polarizations.

5.2.1 The plane polariscope

The simplest form of photoelastic imaging employs a plane polariscope. In this setup, either white or monochromatic light is passed through a polarizing filter, which only allows light with a specific polarization orientation to pass. This polarized light then travels through the birefringent sample and reaches a second polarizer, known as the analyzer, oriented at 90 degrees relative to the first polarizer. If the sample is unstressed, the polarization of the light remains unchanged as it passes through the material. Since the analyzer is perpendicular to the initial polarizer, no light passes through, and the camera detects no light.

When the sample is under stress, however, the birefringence alters the polarization of the light as it passes through the material. This change in polarization allows some of the light to pass through the analyzer and be detected by the camera. The intensity of light that reaches the camera depends on the initial orientation of the polarizer and the birefringence properties of the material. The light intensity I_p leaving the analyzer is given by[144]:

$$I_p = I_0 sin^2(2\theta) sin^2(\delta/2) \tag{5.1}$$

where I_0 is the initial intensity of the light source, θ is the angle between the direction of the initial polarization and one of the principal stress axes in the sample, and δ is the phase retardation, which is a function of the material's birefringence. A limitation of this setup is that the intensity of light reaching the camera is dependent on the initial orientation of the polarizer.

5.2.2 The circular polariscope

To mitigate the dependency of light intensity on the initial polarizer orientation, a circular polariscope is employed. In this configuration, two quarter-wave plates are introduced—one placed between the polarizer and the sample, and the other between the sample and the analyzer. These plates, typically made from birefringent crystals, split

the incident light along the crystal's two optical axes. The plate thickness is chosen to induce a phase shift of $\lambda/4$ (a $\pi/2$ phase shift), converting the linearly polarized light into circularly polarized light. The addition of the quarter-wave plates eliminates the dependency of the exiting light on the polarizer orientation, effectively removing the isoclinic lines (regions of constant stress direction) from the image. The light intensity I_p is now given by[144]:

$$I_p = I_0 sin^2(\delta/2) \tag{5.2}$$

This results in an image where the stress distribution can be more easily visualized, free from the angular dependence of the polarizers.

5.3 Experimental Setup and Methodology

A cavitation bubble is generated via optical breakdown by focusing a pulsed laser into a gelatin phantom, as illustrated in Fig. 5.2(a). The gelatin samples are prepared following the procedure outlined in Section 2.9, using two different gelatin-to-water mass ratios: 4% and 8%. These samples are positioned in glass cuvettes with dimensions of $20 \times 20 \times 5$,mm^3, providing optical access from three sides, allowing for laser focusing, high-speed camera observation, and illumination through the glass windows. A long-working-distance microscope objective is used to focus the laser pulse near the boundary of the glass, which has a thickness of 1 mm, ensuring non-spherical bubble collapse. The dynamics of the bubble are recorded using a high-speed camera (Shimadzu XPV-X2) at a frame rate of 1 million frames per second, equipped with a macro lens (LAOWA f2.8) that provides a resolution of 11 µm per pixel. Continuous green laser light (Shaan'xi Richeng Ltd, DPSS Green Dot Laser Module, 532 nm wavelength) is used for illumination. For capturing shear wave propagation, a different high-speed camera (Photron AX-Mini 200) is employed, operating at 50,000 frames per second with a spatial resolution of 10 µm per pixel.

To visualize the shear stresses after cavitation bubble collapse, we employ a circular po-

lariscope setup. The gelatin solutions exhibit excellent birefringence under stress, making them well-suited for photoelastic experiments[145]. The circular polariscope is configured using two linear polarizers oriented at 90° to each other, along with two quarter-wave plates ($\lambda/4$), also oriented at 90° to each other, as explained in the previous section on polariscopes. This setup ensures that the sample is illuminated with circularly polarized light, allowing for stress visualization independent of the initial orientation of the polarizers.

To capture the fast cavitation dynamics and the associated shear wave propagation, the polariscope is initially set to photoelastic mode. However, when focusing on bubble dynamics specifically, the setup can be easily adapted to a standard shadowgraphy configuration. This is done by rotating the linear polarizers so that their axes are parallel, which allows for high-contrast imaging of the bubble boundaries and surrounding flow without stress-related birefringence interference.

5.4 Shear waves induced by non-spherical collapse near a rigid boundary

Figure 5.2(b) illustrates the behavior of a single bubble near a rigid surface in a 4% w/v gelatin solution at room temperature (22°C) for stand-off distance $\gamma < 0.17$. In Chapter 3 we show that this stand-off results in intense bubble dynamics, culminating in the formation of a needle jet and during the collapse phase, the bubble exhibits a radial indentation, which is also noticeable in our current observations, particularly in the kink seen in the final frame of Fig. 5.2(b). This phenomenon arises due to a radial flow parallel to the boundary that converges along the axis of symmetry which results in the emission of a shear wave near the solid boundary. Here, we don't focus on the bubble dynamics and its effect on the generated shear wave, but on the use of the generated shear wave for measuring elasticity of the propagating medium.

Figure 5.2 presents a typical result from the observation using photoelasticity for a laser induced cavitation bubble under the same conditions as in Fig. 5.1. To achieve

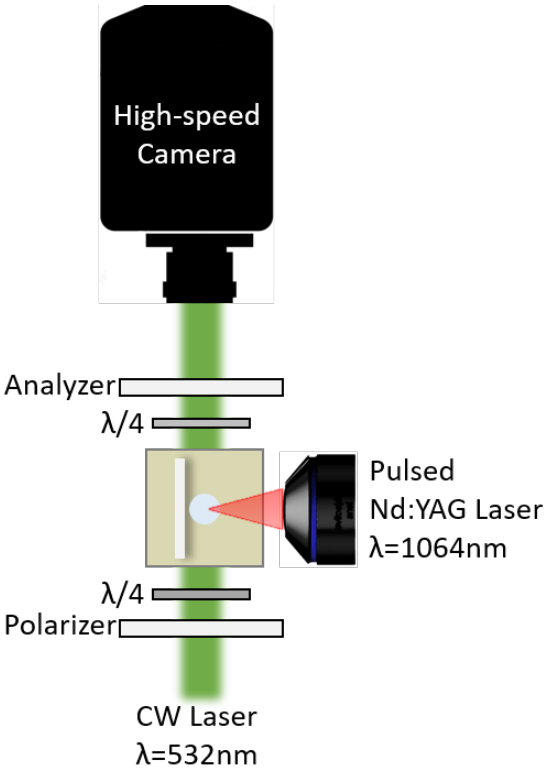

Figure 5.1: Top view of the experimental setup for high speed imaging of a laser-induced cavitation bubble in a tissue-mimicking material using a circular polariscope.

such a goal, two polarizers (the one closed to the camera is called analyzer) with their polarization vertical to each other and two $\lambda/4$ waveplates with their fast axis 90 degree rotated relative to each other are placed in the illumination path, Fig. 5.1(a). A detailed explanation of the principle of the stress-optical relation [146] and the principal of the circular polariscope [100] is not given here. Upon initiation at $t = 0$, the cavitation bubble grows and compresses the adjacent gelatin, producing a luminous corona surrounding the bubble due to heightened material stresses. When the bubble reaches its maximum size, it exerts pressure on the gel affixed to the rigid surface, functioning as a shear wave source, which produces a long luminous line along the rigid surface, proportional to the bubble's maximum radius. During the collapse stage of the cavitation bubble, a bright area appears on its kink due to strongly radial contraction. Besides, the bright area is further increased nearby the boundary due to the side wall of the bubble collapsing towards each other.

Taking advantage of the shear waves propagating away from the rigid boundary after the cavitation dynamics, the motion of the shear wave in different gelatin gel samples are

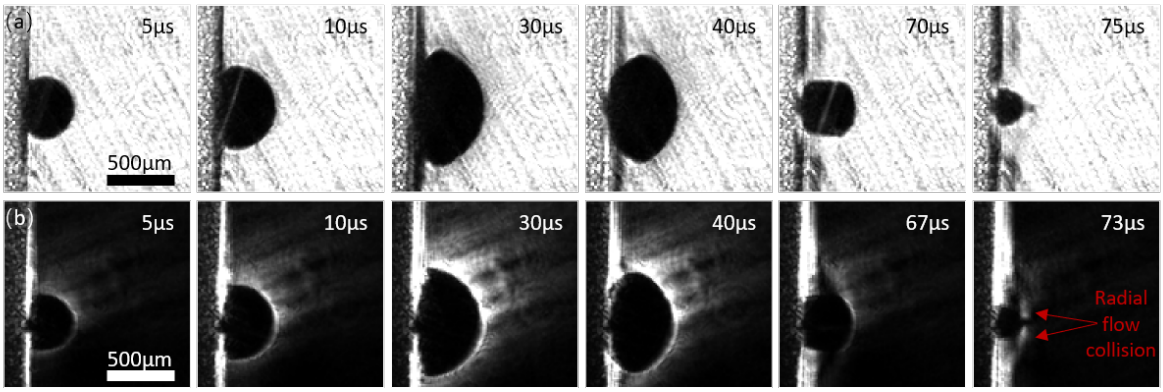

Figure 5.2: Selected shaodowgraphy frames (a) and photoelastic frames (b) of the dynamics of a laser induced cavitation bubble nucleated in 4% w/v gelatin gel under room temperature recorded at 1 million fps.

given in Fig. 5.3. In Fig. 5.3(a), 4% w/v gelatin gel under room temperature is used; in Fig. 5.3(b), 8% w/v gelatin gel under room temperature is used; In Fig. 5.3(c), 8% w/v gelatin gel under 6°C is used. Notice that, the presence of isochromatics can be clearly marked during the shear wave propagation. Besides, based on the video record, we observe that the speed of the shear waves varies within different gel samples, implying a different elastic modulus.

To achieve the goal of elastic modulus measurement, one can always resort to the tracking of the wave profile during the propagation of shear waves [147, 148]. However, due to the existence of noises on video recorded with circular polariscope, a stable peak tracking can be hardly achieved. To measure the elastic modulus while reducing the influence of the noise, a local phase velocity-based imaging (LPVI) is applied to CSWR [149, 150]. The LPVI obtain shear modulus information in k-space, which is a wavenumber-frequency domain. Based on the brightness change on each pixel from the video measurement, under the assumption that shear wave propagates only in 1-D direction, a local particle motion $v(x, y, t)$ can be accomplished and transferred into k-space based on the 1D temporal and 2D spatial Fourier transform:

$$V(k_x, k_y, f) = \int_{-\infty}^{\infty}\int_{-\infty}^{\infty}\int_{-\infty}^{\infty} v(x, y, t)e^{2\pi ft - k_x x - k_y y}dxdydt, \tag{5.3}$$

Hence, $V(k_x, k_y, f)$ denotes the resultant three-dimensional k-space representation in re-

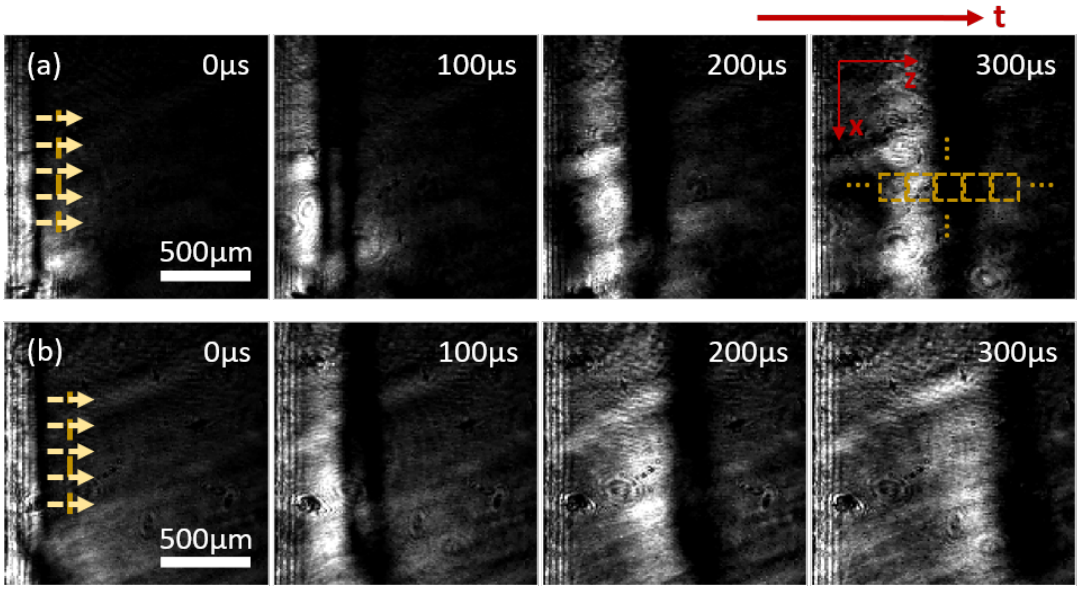

Figure 5.3: Shear wave propagation visualized by high-speed circular polariscope for gelatin gel at different temperature T : (a) 8% w/v gelatin at 22°C, (b) 8% w/v gelatin at 6°C.

lation to the frequency and wavenumber vectors. Using the acquired spectrum data $V(k_x, k_y, f)$, a wavenumber spectrum can be derived for a specific oscillation frequency f_0. $c(f_0) = \frac{2\pi f_0}{|\boldsymbol{k}|}$ is used to calculate the spatial distribution of the phase velocity of the shear wave motion for the frequency f_0, where $|\boldsymbol{k}|$ is a wavenumber magnitude corresponding to the peak value in k-space [149]. Figure 5.4 illustrates the two-dimensional shear wave phase velocity maps reconstructed from Fig. 5.3(b,c) utilizing CSWR. The mean value of the shear wave speed is 2.3 m/s in Fig. 5.4(a), and 3.4 m/s in Fig. 5.4(b). Notice that due to the cavitation is located around the lower right corner of the phase velocity map, a local maximum can always be measured.

In Fig. 5.5(a), gelatin gel with different concentration and temperature are measured at different time, where $t = 0$ is corresponding to the time when gel is poured into the cuvette. The Young's modulus increases with the gel age/gel concentration. The increasing speed gradually slows down with the time. In shorter time range, the measurement of the Young's modulus of 4% w/v gel decreases with the increasing of the temperature is given in Fig. 5.5(b). After 1 hour, the temperature of the gel fully reduced to the room temperature, so does its Young's modulus. The results here are shown with $f_0 = 5 \times 10^3 \mathrm{s}^{-1}$, and the the measurement under different strain-rates, from $O(10^3)\mathrm{s}^{-1}$ to $O(10^{-4})\mathrm{s}^{-1}$ show

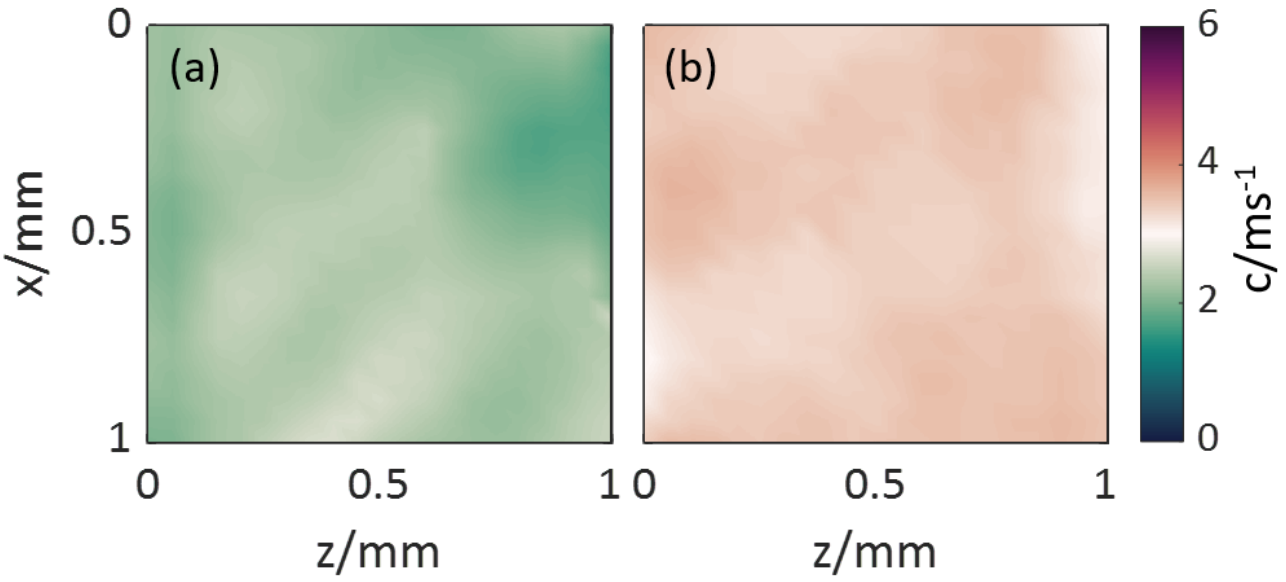

Figure 5.4: The shear wave map calculated with CSWR. (a) 8% w/v gelatin gel at 22°C is used; (b) 8% w/v gelatin gel at 6°C is used.

consistences with each other.

5.5 Conclusion

In this chapter, we introduced Cavitation Induced Shear Wave Rheometry (CSWR) for characterizing the elastic properties of soft materials, particularly TMMs. By leveraging the generation of shear waves through the non-spherical collapse of cavitation bubbles near a rigid boundary, we have demonstrated a method to measure the elasticity of these materials.

Through detailed experimental setups involving photoelastic imaging, we captured the shear wave propagation in gelatin phantoms of different concentrations and temperatures. Using high-speed cameras and a circular polariscope, we visualized the stress distributions and shear wave dynamics induced by cavitation.

The experimental results showed that shear wave speeds varied with different gelatin concentrations and temperatures, reflecting differences in the elastic modulus of the samples. We employed a Local Phase Velocity-based Imaging (LPVI) approach to obtain shear modulus information in the wavenumber-frequency domain, which allowed for accurate measurement of the shear wave speeds and the subsequent calculation of the elastic

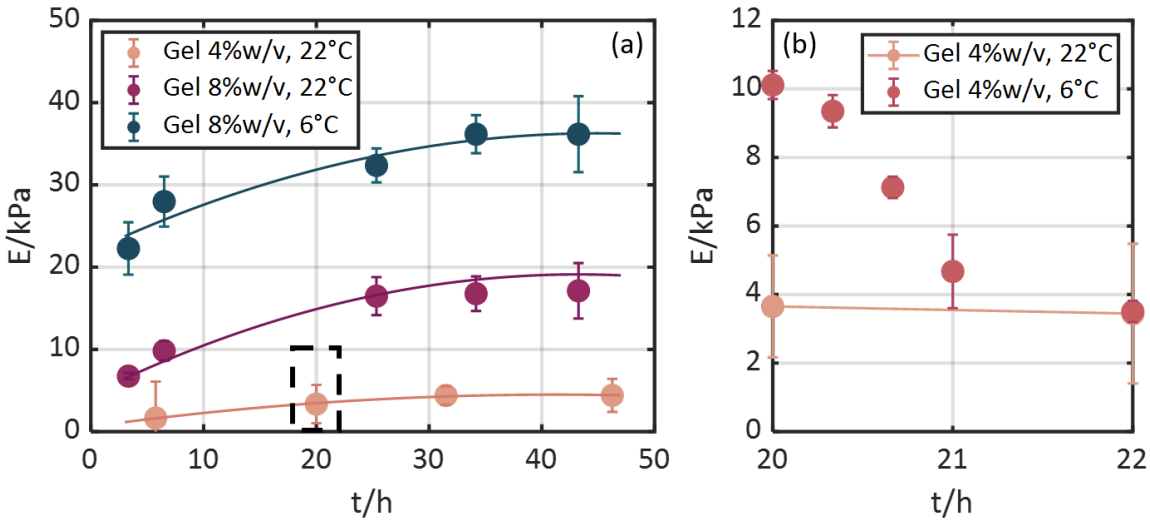

Figure 5.5: The Young's modulus in gelatin gel varies with age for (a) different concentration and temperatures, (b) for different temperature. The solid lines are corresponding to the polynomial fitting results.

modulus.

Our findings indicate that CSWR is a promising tool for non-destructive, high-resolution measurement of the mechanical properties of soft materials. The technique's ability to measure the Young's modulus over time and under different conditions underscores its potential for applications in biomedical engineering and material science. By overcoming the challenges of traditional methods, CSWR provides a robust framework for the detailed study of soft material mechanics. The presented method provides a minimally invasive method of characterizing soft materials, and can be used to measure the elastic modulus in O(1)mm surrounding the cavitation bubble at high strain-rates from $O(10^3)s^{-1}$ to $O(10^4)s^{-1}$.

Chapter 6

Conclusion and outlook

While a significant body of research focuses on cavitation in liquids, typically utilizing high-speed optical imaging, many therapeutic applications involve tissues where optical access is limited. The fundamental difference between liquids and tissues, as elastic solids, lies in the restoring force. This difference not only results in distinct cavitation bubble dynamics in soft solids compared to liquids but also permits the propagation of shear waves in these media. In this thesis, we introduce a high-speed ultrasound technique that potentially enables the capture of bubble dynamics in nontransparent materials. Furthermore, we demonstrate that the non-spherical collapse of bubbles in a soft solid generates shear waves, which can be utilized in elastography applications. In the following sections, we will first summarize the main findings of Chapters 2 to 5, followed by a discussion on potential future research directions.

6.1 Conclusions

In Chapter 2, we explore how to use plane wave ultrasound imaging to study cavitation bubble dynamics. Through careful experiments, we found that single plane wave imaging is sufficient to capture the fast dynamics of these bubbles, providing a good balance between image quality and frame rate. Our ultrasound results, benchmarked against optical

high-speed imaging in water and a transparent soft material, show that ultrasound imaging can effectively resolve bubble dynamics. Although we did not study nontransparent soft materials and soft tissue in this thesis, our findings suggest that ultrasound imaging could potentially be applied to these materials as well.

In Chapter 3, our focus shifts to optical imaging of shear waves generated by the non-spherical collapse of laser-induced cavitation bubbles in TMMs. Through precise control and observation, we explain how bubble dynamics affect shear wave propagation, highlighting the significance of the stand-off distance in influencing wave characteristics such as direction and energy. There, we introduced graphite particles to the samples and used PIV to track the shear wave propagation in the medium. This chapter sets the foundation for using these shear waves in elastography, demonstrating their potential for various medical applications, which is explored further in subsequent chapters.

In Chapter 4, we expand our research by presenting an ultrasound plane wave compounding technique to capture shear wave propagation in TMMs. We again use a transparent material to benchmark it against optical high-speed imaging. We show that using bubbles as tracers instead of graphite particles improves the ultrasound backscattered signal. As a result, single plane wave imaging can be used to capture shear wave propagation, enabling deeper tissue imaging. Although not studied in this thesis, this finding is particularly interesting for bubbly mediums, such as during thermal ablation, where numerous bubbles are generated. These bubbles themselves may act as tracers for tracking shear wave propagation.

Additionally, we demonstrate that shear waves can be generated not only by cavitation bubble collapse inside soft tissue but also by bubble jetting from a cavitation bubble in a thin layer on top of a soft solid into the soft material. This is noteworthy because, in applications where optical access to focus a laser beam inside a TMM is limited, shear waves can still be generated. The propagation of these waves can then be studied using a similar approach to what is presented in Chapter 5.

In Chapter 5, we introduce Cavitation-induced Shear Wave Rheometry (CSWR) aimed at characterizing the elastic properties of soft materials under high strain rates. By opti-

cally capturing shear wave motion induced by laser cavitation bubbles, we demonstrated the sensitivity and versatility of CSWR in assessing material elasticity. This method holds promise for various applications in biomedical engineering and material science, offering a minimally invasive approach to studying material behavior under dynamic loading conditions.

In conclusion, this thesis contributes to the development of an ultrasound technique designed for studying cavitation bubble dynamics in non-transparent TMMs. It demonstrates how both cavitation bubble collapse near a rigid boundary and bubble jetting into TMMs generate shear waves, highlighting their potential for use in shear wave elastography and rheometry techniques.

6.2 Outlook and perspectives

The research presented in this thesis opens up several promising avenues for future exploration. We have demonstrated that cavitation bubble dynamics can be captured using high-frame-rate ultrasound imaging, although this required generating the bubble close to the ultrasound transducer. A key challenge remains the limited imaging depth achievable with plane wave techniques. Future research should focus on extending the imaging depth without compromising frame rates, potentially through techniques that transmit multiple ultrasound plane waves before receiving the reflected waves. By recording all reflections within a single frame and employing source localization methods, the bubble wall could be accurately tracked over time, even at greater depths.

While this thesis successfully demonstrates the effectiveness of ultrasound imaging in studying cavitation bubble dynamics in transparent materials, further research is required to adapt these techniques for non-transparent soft materials and biological tissues. These media present additional complexities, such as heterogeneities, varying acoustic properties, and intricate structures. Developing and validating the ultrasound techniques presented here for more complex, clinically relevant environments is an essential next step.

The successful visualization of shear waves in TMMs, along with the demonstrated correlation between shear wave dynamics and tissue properties in controlled experiments,

highlights significant potential for clinical applications. Future research could explore the use of naturally occurring or intentionally generated bubbles in procedures such as thermal ablation and HIFU. These treatments involve bubble generation, and understanding cavitation dynamics in these contexts could improve real-time monitoring. We observed that different stand-off distances produce shear waves propagating in various directions, complicating wavefront visualization in clinical scenarios, where bubbles collapse at varying stand-off distances. This superposition of waves poses challenges for accurate interpretation. A critical next step would be to study shear waves generated by the collapse of multiple bubbles with different stand-off distances to better understand and address this complexity. Subsequently, measuring shear waves produced in these therapeutic applications would further refine and optimize their clinical use.

Another promising direction for future research is adapting the CSWR technique for plane wave ultrasound imaging. Integrating CSWR with high-frame-rate ultrasound imaging could allow the technique to be applied to non-transparent materials, significantly broadening its clinical and material science applications.

Additionally, combining the developed ultrasound imaging techniques with other imaging modalities could offer complementary insights and a more comprehensive understanding of cavitation bubble dynamics and shear wave propagation. For instance, integrating ultrasound with optical coherence tomography (OCT) or photoacoustic imaging could enable the simultaneous visualization of bubble dynamics and shear wave propagation in tissues with limited optical access, further enhancing diagnostic and therapeutic precision.

By addressing these future research directions, the insights gained from this thesis can be expanded, leading to a deeper understanding of cavitation bubble dynamics and their broader applications in both biomedical and material science fields, particularly in the context of non-transparent soft materials and tissues.

Bibliography

[1] G. Menzl, M. A. Gonzalez, P. Geiger, F. Caupin, J. L. Abascal, C. Valeriani, and C. Dellago. "Molecular mechanism for cavitation in water under tension". *Proceedings of the National Academy of Sciences* **113** (48), 13582–13587 (2016).

[2] J. M. Rosselló and C.-D. Ohl. "On-demand bulk nanobubble generation through pulsed laser illumination". *Physical Review Letters* **127** (4), 044502 (2021).

[3] J. J. Lyons, M. M. Haney, D. Fee, A. G. Wech, and C. F. Waythomas. "Infrasound from giant bubbles during explosive submarine eruptions". *Nature Geoscience* **12** (11), 952–958 (2019).

[4] W. M. Rohsenow. "Boiling". *Annual Review of Fluid Mechanics* **3** (1), 211–236 (1971).

[5] P. R. Gogate and A. M. Kabadi. "A review of applications of cavitation in biochemical engineering/biotechnology". *Biochemical Engineering Journal* **44** (1), 60–72 (2009). Invited Review Issue 2009.

[6] J.-P. Franc. "The Rayleigh-Plesset equation: a simple and powerful tool to understand various aspects of cavitation". Vol. 491. Springer, 2008, pp. 1–41.

[7] R. E. Arndt. "Cavitation in vortical flows". *Annual review of fluid mechanics* **34** (1), 143–175 (2002).

[8] E. Neppiras. "Acoustic cavitation". *Physics Reports* **61** (3), 159–251 (1980).

[9] M. Ashokkumar. "The characterization of acoustic cavitation bubbles – An overview". *Ultrasonics Sonochemistry* **18** (4), 864–872 (2011). European Society of Sonochemistry (ESS12).

[10] K. Yasui. “Acoustic Cavitation”. *Acoustic Cavitation and Bubble Dynamics*. Cham: Springer International Publishing, 2018, pp. 1–35. ISBN: 978-3-319-68237-2.

[11] W. Lauterborn and C.-D. Ohl. “Cavitation bubble dynamics”. *Ultrasonics Sonochemistry* **4** (2), 65–75 (1997). Fifth Meeting of the European Society of Sonochemistry.

[12] F. Reuter and C.-D. Ohl. “Chapter 2 - Nonspherical Collapse of Single Bubbles Near Boundaries and in Confined Spaces”. *Cavitation and Bubble Dynamics*. Ed. by P. Koukouvinis and M. Gavaises. Academic Press, 2021, pp. 37–72. ISBN: 978-0-12-823388-7.

[13] C. E. Brennen. *Cavitation and Bubble Dynamics*. Oxford University Press, 1995. ISBN: 0195094093.

[14] C. Ohl and R. Ikink. “Shock-wave-induced jetting of micron-size bubbles”. *Physical review letters* **90** (21), 214502 (2003).

[15] A. PHILIPP and W. LAUTERBORN. “Cavitation erosion by single laser-produced bubbles”. *Journal of Fluid Mechanics* **361**, 75–116 (1998).

[16] F. Reuter, C. Deiter, and C.-D. Ohl. “Cavitation erosion by shockwave self-focusing of a single bubble”. *Ultrasonics Sonochemistry* **90**, 106131 (2022).

[17] M. Yusvika, A. R. Prabowo, S. J. Baek, and D. D. D. Prija Tjahjana. “Achievements in Observation and Prediction of Cavitation: Effect and Damage on the Ship Propellers”. *Procedia Structural Integrity* **27**, 109–116 (2020). The 6th International E-Conference on Industrial, Mechanical, Electrical and Chemical Engineering (ICIMECE 2020) Special Symposium - Integrity of Mechanical Structure and Material.

[18] T. J. van Terwisga, M. van Rijsbergen, E. van Wijngaarden, J. Bosschers, S. Schenke, and T. Melissaris. “Chapter 3 - Cavitation Nuisance in Ship Propulsion: A Review of Developments”. *Cavitation and Bubble Dynamics*. Ed. by P. Koukouvinis and M. Gavaises. Academic Press, 2021, pp. 73–109. ISBN: 978-0-12-823388-7.

[19] X. Escaler, E. Egusquiza, M. Farhat, F. Avellan, and M. Coussirat. "Detection of cavitation in hydraulic turbines". *Mechanical Systems and Signal Processing* **20**, 983–1007 (2006).

[20] P. Kumar and R. Saini. "Study of cavitation in hydro turbines—A review". *Renewable and Sustainable Energy Reviews* **14** (1), 374–383 (2010).

[21] W. Chan. "Correlation between cavitation type and cavitation erosion in centrifugal pumps". *International Journal of Heat and Fluid Flow* **11** (3), 269–271 (1990).

[22] O. Asi. "Failure of a diesel engine injector nozzle by cavitation damage". *Engineering Failure Analysis - ENG FAIL ANAL* **13**, 1126–1133 (2006).

[23] W. Bergwerk. "Flow Pattern in Diesel Nozzle Spray Holes". *Proceedings of the Institution of Mechanical Engineers* **173** (1), 655–660 (1959).

[24] W. H. Nurick. "Orifice Cavitation and Its Effect on Spray Mixing". *Journal of Fluids Engineering* **98** (4), 681–687 (1976).

[25] R. D. Reitz and F. V. Bracco. "Mechanism of atomization of a liquid jet". *The Physics of Fluids* **25** (10), 1730–1742 (1982).

[26] Y. Pishchalnikov, O. Sapozhnikov, M. Bailey, J. Williams, R. Cleveland, T. Colonius, L. Crum, A. Evan, and J. Mcateer. "Cavitation Bubble Cluster Activity in the Breakage of Kidney Stones by Lithotripter Shock Waves". *Journal of endourology / Endourological Society* **17**, 435–46 (2003).

[27] W. G. Pitt, G. A. Husseini, and B. J. Staples. "Ultrasonic drug delivery – a general review". *Expert Opinion on Drug Delivery* **1**, 37–56 (2004).

[28] J.-C. Veilleux, K. Maeda, T. Colonius, and J. Shepherd. "Transient Cavitation in Pre-Filled Syringes During Autoinjector Actuation". 2018. ISBN: 9780791861851.

[29] C.-D. Ohl, M. Arora, R. Dijkink, V. Janve, and D. Lohse. "Surface cleaning from laser-induced cavitation bubbles". *Applied Physics Letters* **89**, 074102–074102 (2006).

[30] R. Dijkink and C.-D. Ohl. "Laser-induced cavitation based micropump". *Lab Chip* **8**, 1676–1681 (10 2008).

[31] M. Zupanc, T. Kosjek, M. Petkovšek, M. Dular, B. Kompare, B. Širok, Ž. Blažeka, and E. Heath. "Removal of pharmaceuticals from wastewater by biological processes, hydrodynamic cavitation and UV treatment". *Ultrasonics Sonochemistry* **20** (4), 1104–1112 (2013).

[32] J. Rapet. "Coupling of cavitation with transverse waves through elastic solids". PhD thesis. Nanyang Technological University, 2019.

[33] P. Cui, A.-M. Zhang, S. Wang, and B. C. Khoo. "Ice breaking by a collapsing bubble". *Journal of Fluid Mechanics* **841**, 287–309 (2018).

[34] E. Brujan, T. Ikeda, and Y. Matsumoto. "Jet formation and shock wave emission during collapse of ultrasound-induced cavitation bubbles and their role in the therapeutic applications of high-intensity focused ultrasound". *Physics in medicine and biology* **50**, 4797–809 (2005).

[35] G. Sinibaldi, A. Occhicone, F. A. Pereira, D. Caprini, L. Marino, F. Michelotti, and C. M. Casciola1. "Laser induced cavitation: Plasma generation and breakdown shockwave". *Physics of Fluids* **31** (2019).

[36] S. R. Aglyamova, A. B. Karpiouk, F. Bourgeois, A. Ben-Yakar, and S. Y. Emelianov. "Ultrasound measurements of cavitation bubble radius for femtosecond laser-induced breakdown in water". *Optics Letters* **33** (2008).

[37] S. Tiwari, A. Kazemi-Moridani, Y. Zheng, C. W. Barney, K. R. McLeod, C. E. Dougan, A. J. Crosby, G. N. Tew, S. R. Peyton, S. Cai, et al. "Seeded laser-induced cavitation for studying high-strain-rate irreversible deformation of soft materials". *Soft Matter* **16** (39), 9006–9013 (2020).

[38] C. A. Sacchi. "Laser-induced electric breakdown in water". *J. Opt. Soc. Am. B* **8** (2), 337–345 (1991).

[39] L. Martí-López, R. Ocaña, E. Piñeiro, and A. Asensio. "Laser Peening Induced Shock Waves and Cavitation Bubbles in Water Studied by Optical Schlieren Visualization". *Physics Procedia* **12**, 442–451 (2011). Lasers in Manufacturing 2011 - Proceedings of the Sixth International WLT Conference on Lasers in Manufacturing.

[40] J.-P. Franc and J.-M. Michel. *Fundamentals of cavitation*. Vol. 76. Springer science & Business media, 2006.

[41] L. Rayleigh. "VIII. On the pressure developed in a liquid during the collapse of a spherical cavity". *The London, Edinburgh, and Dublin Philosophical Magazine and Journal of Science* **34** (200), 94–98 (1917).

[42] B. Dollet, P. Marmottant, and V. Garbin. "Bubble Dynamics in Soft and Biological Matter". *Annual Review of Fluid Mechanics* **51** (2019).

[43] C. W. Barney, C. E. Dougan, K. R. McLeod, A. Kazemi-Moridani, Y. Zheng, Z. Ye, S. Tiwari, I. Sacligil, R. A. Riggleman, S. Cai, J.-H. Lee, S. R. Peyton, G. N. Tew, and A. J. Crosby. "Cavitation in soft matter". *Proceedings of the National Academy of Sciences* **117** (17), 9157–9165 (2020).

[44] J. Goeller, A. Wardlaw, D. Treichler, J. O'Bruba, and G. Weiss. "Investigation of Cavitation as a Possible Damage Mechanism in Blast-Induced Traumatic Brain Injury". *Journal of neurotrauma* **29**, 1970–81 (2012).

[45] J. Lang, R. Nathan, D. Zhou, X. Zhang, B. Li, and Q. Wu. "Cavitation causes brain injury". *Physics of Fluids* **33** (3), 031908 (2021). 031908.

[46] W. F. Busse. "Physics of Rubber as Related to the Automobile". *Journal of Applied Physics* **9**, 438–451 (1938).

[47] F. L. Yerzley. "Adhesion of Neoprene to Metal". *Industrial & Engineering Chemistry* **13**, 166–180 (1939).

[48] J. B. Estrada, C. Barajas, D. L. Henann, E. Johnsen, and C. Franck. "High strain-rate soft material characterization via inertial cavitation". *Journal of the Mechanics and Physics of Solids* **112**, 291–317 (2018).

[49] S. Buyukozturk and C. Franck. “Expanding Inertial Microcavitation Rheometry to Cover Large Material Stretches in Soft Materials”. *Dynamic Behavior of Materials, Volume 1*. Ed. by L. Lamberson, S. Mates, and V. Eliasson. Cham: Springer International Publishing, 2021, pp. 7–10. ISBN: 978-3-030-59947-8.

[50] J. S. Allen and R. A. Roy. “Dynamics of gas bubbles in viscoelastic fluids. I. Linear viscoelasticity”. *The Journal of the Acoustical Society of America* **107** (6), 3167–3178 (2000).

[51] J. S. Allen and R. A. Roy. “Dynamics of gas bubbles in viscoelastic fluids. II. Nonlinear viscoelasticity”. *The Journal of the Acoustical Society of America* **108** (4), 1640–1650 (2000).

[52] X. Yang and C. C. Church. “A model for the dynamics of gas bubbles in soft tissue”. *The Journal of the Acoustical Society of America* **118** (6), 3595–3606 (2005).

[53] C. Hua and E. Johnsen. “Nonlinear oscillations following the Rayleigh collapse of a gas bubble in a linear viscoelastic (tissue-like) medium”. *Physics of Fluids* **25** (8) (2013).

[54] R. Gaudron, M. T. Warnez, and E. Johnsen. “Bubble dynamics in a viscoelastic medium with nonlinear elasticity”. *Journal of Fluid Mechanics* **766**, 54–75 (2015).

[55] T. Cohen and A. Molinari. “Dynamic cavitation and relaxation in incompressible nonlinear viscoelastic solids”. *International Journal of Solids and Structures* **69-70**, 544–552 (2015).

[56] M. T. Warnez and E. Johnsen. “Numerical modeling of bubble dynamics in viscoelastic media with relaxation”. *Physics of Fluids* **27** (6), 063103 (2015).

[57] C. Barajas and E. Johnsen. “The effects of heat and mass diffusion on freely oscillating bubbles in a viscoelastic, tissue-like medium”. *The Journal of the Acoustical Society of America* **141** (2), 908–918 (2017).

[58] E. Zilonova, M. Solovchuk, and T. Sheu. "Bubble dynamics in viscoelastic soft tissue in high-intensity focal ultrasound thermal therapy". *Ultrasonics Sonochemistry* **40**, 900–911 (2018).

[59] D. D. Joseph. "Historical perspectives on the elasticity of liquids". *Journal of Non-Newtonian Fluid Mechanics* **19** (3), 237–249 (1986).

[60] A. Bot, I. A. van Amerongen, R. D. Groot, N. L. Hoekstra, and W. G. Agterof. "Large deformation rheology of gelatin gels". *Polymer Gels and Networks* **4** (3), 189–227 (1996).

[61] J.-L. Gennisson, T. Deffieux, M. Fink, and M. Tanter. "Ultrasound elastography: Principles and techniques". *Diagnostic and Interventional Imaging* **94** (5), 487–495 (2013). Ultrasound elastography.

[62] R. M. Sigrist, J. Liau, A. El Kaffas, M. C. Chammas, and J. K. Willmann. "Ultrasound elastography: review of techniques and clinical applications". *Theranostics* **7** (5), 1303 (2017).

[63] J. Ophir, I. Cespedes, H. Ponnekanti, Y. Yazdi, and X. Li. "Elastography: a quantitative method for imaging the elasticity of biological tissues". *Ultrasonic imaging* **13** (2), 111–134 (1991).

[64] M. S. Taljanovic, L. H. Gimber, G. W. Becker, L. D. Latt, A. S. Klauser, D. M. Melville, L. Gao, and R. S. Witte. "Shear-wave elastography: basic physics and musculoskeletal applications". *Radiographics* **37** (3), 855 (2017).

[65] A. P. Sarvazyan, O. V. Rudenko, S. D. Swanson, J. B. Fowlkes, and S. Y. Emelianov. "Shear wave elasticity imaging: a new ultrasonic technology of medical diagnostics". *Ultrasound in medicine & biology* **24** (9), 1419–1435 (1998).

[66] S. Izak Ghasemian, F. Reuter, and C. D. Ohl. "High-speed ultrasound imaging of laser-induced cavitation bubbles". *Applied Physics Letters* **119** (11), 114101 (2021).

[67] T. Sun, G. Samiotaki, S. Wang, C. Acosta, C. C. Chen, and E. E. Konofagou. "Acoustic cavitation-based monitoring of the reversibility and permeability of ultrasound-induced blood-brain barrier opening". *Physics in Medicine & Biology* **60** (23), 9079 (2015).

[68] Y. A. Pishchalnikov, O. A. Sapozhnikov, M. R. Bailey, J. C. Williams Jr, R. O. Cleveland, T. Colonius, L. A. Crum, A. P. Evan, and J. A. McAteer. "Cavitation bubble cluster activity in the breakage of kidney stones by lithotripter shockwaves". *Journal of endourology* **17** (7), 435–446 (2003).

[69] S. Hu, X. Zhang, M. Unger, I. Patties, and A. Melzer. "Focused Ultrasound-Induced Cavitation Sensitizes Cancer Cells to Radiation Therapy and Hyperthermia". *Cells* **9** (2020).

[70] K. Ramaswamy, V. Marx, D. Laser, T. Kenny, T. Chi, M. Bailey, M. D. Sorensen, R. H. Grubbs, and M. L. Stoller. "Targeted microbubbles: a novel application for the treatment of kidney stones". *BJU Int* **116** (2015).

[71] P. Zhan, W. Tan, J. Si, S. Xu, J. Tong, and X. Hou. "Optical imaging of objects in turbid media using heterodyned optical Kerr gate". *Applied Physics Letters* **104** (21), 211907 (2014).

[72] J. Bercoff. "Ultrafast Ultrasound Imaging". Vol. 37. 2011. ISBN: 978-953-307-279-1.

[73] G. Montaldo, M. Tanter, J. Bercoff, N. Benech, and M. Fink. "Coherent plane-wave compounding for very high frame rate ultrasonography and transient elastography". *IEEE Transactions on Ultrasonics, Ferroelectrics, and Frequency Control* **56** (3), 489–506 (2009).

[74] M. Tanter and M. Fink. "Ultrafast Imaging in Biomedical Ultrasound". *IEEE Transactions on Ultrasonics, Ferroelectrics, and Frequency Control* **61** (2015).

[75] G. Montaldo, M. Tanter, J. Bercoff, N. Benech, and M. Fink. "Coherent Plane-Wave Compounding for Very High Frame Rate Ultrasonography and Transient Elastography". *IEEE Transactions on Ultrasonics, Ferroelectrics, and Frequency Control* **56** (2009).

[76] M. E. G. Toulemonde. "New beamforming strategy for improved ultrasound imaging : application to biological tissues nonlinear imaging". 2014.

[77] J.-y. Lu, H. Zou, and J. F. Greenleaf. "Biomedical ultrasound beam forming". *Ultrasound in medicine & biology* **20** (5), 403–428 (1994).

[78] V. Perrot, M. Polichetti, F. Varray, and D. Garcia. "So you think you can DAS? A viewpoint on delay-and-sum beamforming". *Ultrasonics* **111**, 106309 (2021).

[79] G. Matrone, A. S. Savoia, G. Caliano, and G. Magenes. "The delay multiply and sum beamforming algorithm in ultrasound B-mode medical imaging". *IEEE transactions on medical imaging* **34** (4), 940–949 (2014).

[80] J. F. Synnevag, A. Austeng, and S. Holm. "Adaptive beamforming applied to medical ultrasound imaging". *IEEE transactions on ultrasonics, ferroelectrics, and frequency control* **54** (8), 1606–1613 (2007).

[81] C.-I. Nilsen and I. Hafizovic. "Beamspace adaptive beamforming for ultrasound imaging". *IEEE Transactions on Ultrasonics, ferroelectrics, and frequency control* **56** (10), 2187–2197 (2009).

[82] B. Luijten, R. Cohen, F. J. De Bruijn, H. A. Schmeitz, M. Mischi, Y. C. Eldar, and R. J. Van Sloun. "Adaptive ultrasound beamforming using deep learning". *IEEE Transactions on Medical Imaging* **39** (12), 3967–3978 (2020).

[83] J.-F. Synnevag, A. Austeng, and S. Holm. "Benefits of minimum-variance beamforming in medical ultrasound imaging". *IEEE transactions on ultrasonics, ferroelectrics, and frequency control* **56** (9), 1868–1879 (2009).

[84] A. Austeng, C.-I. C. Nilsen, A. C. Jensen, S. P. Näsholm, and S. Holm. "Coherent plane-wave compounding and minimum variance beamforming". *2011 IEEE International Ultrasonics Symposium*. IEEE. 2011, pp. 2448–2451.

[85] C.-C. Shen and P.-Y. Hsieh. "Ultrasound Baseband Delay-Multiply-and-Sum (BB-DMAS) nonlinear beamforming". *Ultrasonics* **96**, 165–174 (2019).

[86] Verasonics. *Vantage Sequence Programming Manual*. Version 4.3. Verasonics. 2020. 189 pp. September 12, 2020.

[87] A. Rodriguez-Molares, O. M. H. Rindal, O. Bernard, A. Nair, M. A. L. Bell, H. Liebgott, A. Austeng, and L. Lovstakken. "The UltraSound ToolBox". *2017 IEEE International Ultrasonics Symposium (IUS)* (2017).

[88] C. K. McGarry, L. J. Grattan, A. M. Ivory, and F. Leek. "Tissue mimicking materials for imaging and therapy phantoms: a review". *Physics in Medicine & Biology* **65** (2020).

[89] W. Kang, A. Adnan, T. O'Shaughnessy, and A. Bagchi. "Cavitation nucleation in gelatin: Experiment and mechanism". *Acta Biomaterialia* **67** (2018).

[90] R. Oguri and K. Ando. "Cavitation bubble nucleation induced by shock-bubble interaction in a gelatin gel". *Physics of Fluids* **30** (2018).

[91] T. Hopfes, Z. Wang, M. Giglmaier, and N. A. Adams. "Collapse dynamics of bubble pairs in gelatinous fluids". *Experimental Thermal and Fluid Science* **108** (2019).

[92] K. Ando and E. Shirota. "Quasistatic growth of bubbles in a gelatin gel under dissolved-gas supersaturation". *Physics of Fluids* **31** (11), 111701 (2019).

[93] L. Mancia, J. Yang, J.-S. Spratt, J. R. Sukovich, Z. Xu, T. Colonius, C. Franck, and E. Johnsen. "Acoustic cavitation rheometry". *Soft Matter* **17**, 2931–2941 (10 2021).

[94] T. L. Szabo. *Diagnostic Ultrasound Imaging: Inside Out*. Academic Press Series in Biomedical Engineering. 2004. ISBN: 9780080491134.

[95] S. Izak Ghasemian, F. Reuter, Y. Fan, G. Rose, and C.-D. Ohl. "Shear wave generation from non-spherical bubble collapse in a tissue phantom". *Soft matter* **19**, 9405–9412 (2023).

[96] K. Nightingale. "Acoustic radiation force impulse (ARFI) imaging: a review". *Current medical imaging* **7** (4), 328–339 (2011).

[97] H. Zhao, P. Song, D. D. Meixner, R. R. Kinnick, M. R. Callstrom, W. Sanchez, M. W. Urban, A. Manduca, J. F. Greenleaf, and S. Chen. "External Vibration Multi-Directional Ultrasound Shearwave Elastography (EVMUSE): Application in

Liver Fibrosis Staging". *IEEE Transactions on Medical Imaging* **33** (11), 2140–2148 (2014).

[98] A. T. Basford, J. R. Basford, J. Kugel, and R. L. Ehman. "Lorentz-force-induced motion in conductive media". *Magnetic Resonance Imaging* **23** (5), 647–651 (2005).

[99] S. Montalescot, B. Roger, A. Zorgani, R. Souchon, P. Grasland-Mongrain, R. Ben Haj Slama, J.-C. Bera, and S. Catheline. "Electrolysis-induced bubbling in soft solids for elastic-wave generation". *Applied Physics Letters* **108** (9), 094105 (2016).

[100] J. Rapet, Y. Tagawa, and C. D. Ohl. "Shear-wave generation from cavitation in soft solids". *Applied Physics Letters* **114** (2019).

[101] C. E. Brennen. "Cavitation in medicine". *Interface focus* **5** (5), 20150022 (2015).

[102] E.-A. Brujan, T. Ikeda, and Y. Matsumoto. "Shock wave emission from a cloud of bubbles". *Soft Matter* **8** (21), 5777–5783 (2012).

[103] K. B. Bader, K. J. Haworth, A. D. Maxwell, and C. K. Holland. "Post hoc analysis of passive cavitation imaging for classification of histotripsy-induced liquefaction in vitro". *IEEE transactions on medical imaging* **37** (1), 106–115 (2017).

[104] Y. Zhou and Y. Lei. "Cavitation histotripsy at the surface of soft material using the dual-frequency excitation". *Engineering Research Express* **2** (2), 025015 (2020).

[105] M. Li, B. Lan, G. Sankin, Y. Zhou, W. Liu, J. Xia, D. Wang, G. Trahey, P. Zhong, and J. Yao. "Simultaneous photoacoustic imaging and cavitation mapping in shockwave lithotripsy". *IEEE transactions on medical imaging* **39** (2), 468–477 (2019).

[106] N. Chang, S. Lu, D. Qin, T. Xu, M. Han, S. Wang, and M. Wan. "Efficient and controllable thermal ablation induced by short-pulsed HIFU sequence assisted with perfluorohexane nanodroplets". *Ultrasonics Sonochemistry* **45**, 57–64 (2018).

[107] M. O. Steinhauser and M. Schmidt. "Destruction of cancer cells by laser-induced shock waves: recent developments in experimental treatments and multiscale computer simulations". *Soft Matter* **10** (27), 4778–4788 (2014).

[108] G. N. Kawchuk, J. Fryer, J. L. Jaremko, H. Zeng, L. Rowe, and R. Thompson. "Real-time visualization of joint cavitation". *PloS one* **10** (4), e0119470 (2015).

[109] D. P. Chang, N. I. Abu-Lail, J. M. Coles, F. Guilak, G. D. Jay, and S. Zauscher. "Friction force microscopy of lubricin and hyaluronic acid between hydrophobic and hydrophilic surfaces". *Soft Matter* **5** (18), 3438–3445 (2009).

[110] A. Nowicki and K. Dobruch-Sobczak. "Introduction to ultrasound elastography". *Journal of ultrasonography* **16** (65), 113–124 (2016).

[111] F. Reuter, Q. Zeng, and C.-D. Ohl. "The Rayleigh prolongation factor at small bubble to wall stand-off distances". *Journal of Fluid Mechanics* **944**, A11 (2022).

[112] W. Thielicke and R. Sonntag. "Particle Image Velocimetry for MATLAB: Accuracy and enhanced algorithms in PIVlab". *Journal of Open Research Software* **9** (1), 12 (2021).

[113] W. Thielicke and E. J. Stamhuis. "PIVlab – Towards User-friendly, Affordable and Accurate Digital Particle Image Velocimetry in MATLAB". *Journal of Open Research Software* (2014).

[114] F. Reuter and C.-D. Ohl. "Supersonic needle-jet generation with single cavitation bubbles". *Applied Physics Letters* **118** (13), 134103 (2021).

[115] C. Lechner, W. Lauterborn, M. Koch, and R. Mettin. "Fast, thin jets from bubbles expanding and collapsing in extreme vicinity to a solid boundary: A numerical study". *Phys. Rev. Fluids* **4**, 021601 (2 2019).

[116] A. F. Siegel and M. R. Wagner. "Chapter 11 - Correlation and Regression: Measuring and Predicting Relationships". *Practical Business Statistics (Eighth Edition)*. Ed. by A. F. Siegel and M. R. Wagner. Eighth Edition. Academic Press, 2022, pp. 313–370. ISBN: 978-0-12-820025-4.

[117] A. Clifford. *Multivariate Error Analysis: A Handbook of Error Propagation and Calculation in Many-parameter Systems*. Raymond F. Boyer Library Collection. Applied Science Publishers, 1973. ISBN: 9780853345664.

[118] A. Bußmann, F. Riahi, B. Gökce, S. Adami, S. Barcikowski, and N. A. Adams. "Investigation of cavitation bubble dynamics near a solid wall by high-resolution numerical simulation". *Physics of Fluids* **35** (1), 016115 (2023).

[119] B. Choi, E. D. Jansen, and A. J. Welch. "Acoustic-based measurements of material absorption coefficients: relationship between laser pulse duration and stress confinement time". *Journal of applied physics* **94** (12), 7826–7831 (2003).

[120] J. Rosselló, S. Ghasemian, and C.-D. Ohl. "High-speed ultrasound imaging of bubbly flows and shear waves in soft matter". *Soft Matter* (2023).

[121] J. Brum, N. Benech, T. Gallot, and C. Negreira. "Shear Wave Elastography Based on Noise Correlation and Time Reversal". *Frontiers in Physics* **9** (2021).

[122] R. G. Dantas, E. T. Costa, and S. Leeman. "Ultrasound speckle and equivalent scatterers". *Ultrasonics* **43** (6), 405–420 (2005).

[123] C. Ziomek and P. Corredoura. "Digital I/Q demodulator". *Proceedings Particle Accelerator Conference*. Vol. 4. 1995, 2663–2665 vol.4.

[124] C. Kasai, K. Namekawa, A. Koyano, and R. Omoto. "Real-Time Two-Dimensional Blood Flow Imaging Using an Autocorrelation Technique". *IEEE Transactions on Sonics and Ultrasonics* **32** (3), 458–464 (1985).

[125] T. Loupas, J. Powers, and R. Gill. "An axial velocity estimator for ultrasound blood flow imaging, based on a full evaluation of the Doppler equation by means of a two-dimensional autocorrelation approach". *IEEE Transactions on Ultrasonics, Ferroelectrics, and Frequency Control* **42** (4), 672–688 (1995).

[126] Y. Deng, N. C. Rouze, M. L. Palmeri, and K. R. Nightingale. "Ultrasonic Shear Wave Elasticity Imaging Sequencing and Data Processing Using a Verasonics Research Scanner". *IEEE Transactions on Ultrasonics, Ferroelectrics, and Frequency Control* **64** (1), 164–176 (2017).

[127] J. M. Rosselló and C.-D. Ohl. "On-Demand Bulk Nanobubble Generation through Pulsed Laser Illumination". *Physical Review Letters* **127** (4), 044502 (2021).

[128] J. M. Rosselló and C.-D. Ohl. “Clean production and characterization of nanobubbles using laser energy deposition”. *Ultrasonics Sonochemistry* **94**, 106321 (2023).

[129] Y. Miyazaki, M. Usawa, S. Kawai, J. Yee, M. Muto, and Y. Tagawa. “Dynamic mechanical interaction between injection liquid and human tissue simulant induced by needle-free injection of a highly focused microjet”. *Scientific Reports* **11** (1), 14544 (2021).

[130] J. M. Rosselló and C. D. Ohl. “Bullet jet as a tool for soft matter piercing and needle-free liquid injection”. *Biomedical Optics Express* **13** (10), 5202 (2022).

[131] J. M. Rosselló, H. Reese, and C. D. Ohl. “Dynamics of pulsed laser-induced cavities on a liquid–gas interface: from a conical splash to a ‘bullet’ jet”. *Journal of Fluid Mechanics* **939**, A35 (2022).

[132] L. Mancia, J. Yang, J.-S. Spratt, J. R. Sukovich, Z. Xu, T. Colonius, C. Franck, and E. Johnsen. “Acoustic cavitation rheometry”. *Soft Matter* **17** (10), 2931–2941 (2021).

[133] D. Allen, W. Rule, and S. Jones. “Optimizing material strength constants numerically extracted from Taylor impact data”. *Experimental mechanics* **37**, 333–338 (1997).

[134] W. W. Chen and B. Song. *Split Hopkinson (Kolsky) bar: design, testing and applications*. Springer Science & Business Media, 2010.

[135] J. A. Zimberlin, N. Sanabria-DeLong, G. N. Tew, and A. J. Crosby. “Cavitation rheology for soft materials”. *Soft Matter* **3** (6), 763–767 (2007).

[136] J. A. Zimberlin, J. J. McManus, and A. J. Crosby. “Cavitation rheology of the vitreous: mechanical properties of biological tissue”. *Soft Matter* **6** (15), 3632–3635 (2010).

[137] S. Raayai-Ardakani, Z. Chen, D. R. Earl, and T. Cohen. “Volume-controlled cavity expansion for probing of local elastic properties in soft materials”. *Soft matter* **15** (3), 381–392 (2019).

[138] S. Yoon, S. R. Aglyamov, A. B. Karpiouk, S. Kim, and S. Y. Emelianov. "Estimation of mechanical properties of a viscoelastic medium using a laser-induced microbubble interrogated by an acoustic radiation force". *The Journal of the Acoustical Society of America* **130** (4), 2241–2248 (2011).

[139] Y. A. Ilinskii, G. D. Meegan, E. A. Zabolotskaya, and S. Y. Emelianov. "Gas bubble and solid sphere motion in elastic media in response to acoustic radiation force". *The Journal of the Acoustical Society of America* **117** (4), 2338–2346 (2005).

[140] E. Shirota and K. Ando. "Estimation of mechanical properties of gelatin using a microbubble under acoustic radiation force". *Journal of Physics: Conference Series*. Vol. 656. 1. IOP Publishing. 2015, p. 012001.

[141] J. B. Estrada, C. Barajas, D. L. Henann, E. Johnsen, and C. Franck. "High strain-rate soft material characterization via inertial cavitation". *Journal of the Mechanics and Physics of Solids* **112**, 291–317 (2018).

[142] J. Yang, H. C. Cramer III, and C. Franck. "Extracting non-linear viscoelastic material properties from violently-collapsing cavitation bubbles". *Extreme Mechanics Letters* **39**, 100839 (2020).

[143] D. Brewster. "X. on the communication of the structure of doubly refracting crystals to glass, muriate of soda, fluor spar, and other substances, by mechanical compression and dilatation. by david brewster, ll. d. f. r. s. lond. and edin. in a letter addressed to the right hon. sir joseph banks, bart. g. c. b. p. r. s". *Philosophical Transactions of the Royal Society of London* **106**, 156–178 (1816).

[144] K. Ramesh, T. Kasimayan, and B. N. Simon. "Digital photoelasticity – A comprehensive review". *The Journal of Strain Analysis for Engineering Design* **46** (4), 245–266 (2011).

[145] R. Tomlinson and Z. Taylor. "Photoelastic materials and methods for tissue biomechanics applications". *Optical Engineering* **54**, 081208 (2015).

[146] C. W. Macosko, R. G. Larson, et al. "Rheology: principles, measurements, and applications" (1994).

[147] M. L. Palmeri, M. H. Wang, J. J. Dahl, K. D. Frinkley, and K. R. Nightingale. "Quantifying hepatic shear modulus in vivo using acoustic radiation force". *Ultrasound in medicine & biology* **34** (4), 546–558 (2008).

[148] S. A. McAleavey, M. Menon, and J. Orszulak. "Shear-modulus estimation by application of spatially-modulated impulsive acoustic radiation force". *Ultrasonic imaging* **29** (2), 87–104 (2007).

[149] P. Kijanka and M. W. Urban. "Local phase velocity based imaging: A new technique used for ultrasound shear wave elastography". *IEEE transactions on medical imaging* **38** (4), 894–908 (2018).

[150] P. Kijanka and M. W. Urban. "Fast local phase velocity-based imaging: Shear wave particle velocity and displacement motion study". *IEEE transactions on ultrasonics, ferroelectrics, and frequency control* **67** (3), 526–537 (2019).

[151] S. Izak Ghasemian. *Matlab Code for Measuring Cavitation Bubble Dynamics Using Verasonics Ultrasound System*. Version v1.0.0. 2025.

Appendix A

Verasonics setup script for ultrafast ultrasound imaging

The following MATLAB script was developed to capture cavitation bubble dynamics using the Verasonics ultrasound system. It is based on Verasonics example scripts, with modifications to implement the superframe concept for efficient data acquisition and transfer. This ensures the capture of fast cavitation bubble dynamics by minimizing transfer delays. The complete code and additional details are available in the public repository, as referenced in Ref[151].

```
% Adapted from supplied examples by Verasonics and
    modified to record RF data for high-frame rate
    ultrasound imaging in a so-called Super-frame.

clear all
% Basic info:
P.soundSpeed = 1480; % in m/s for water case
P.startDepth = 5;
P.endDepth = 38; % in waveform number.
P.numFrames = 40;  % number of frames
```

```
P.sampleRate = 62.5; % in MHz.

% Specify system parameters
Resource.Parameters.numTransmit = 128;
Resource.Parameters.numRcvChannels = 64;
Resource.Parameters.speedOfSound = P.soundSpeed;
Resource.Parameters.verbose = 2;
Resource.Parameters.initializeOnly = 0;
Resource.Parameters.simulateMode = 0;

% Specify Trans structure array.
Trans.name = 'L7-4';
Trans.frequency = 5; % in MHz
Trans.units = 'wavelengths';
Trans = computeTrans(Trans);

% Specify Resource buffers.
Resource.RcvBuffer(1).datatype = 'int16';
Resource.RcvBuffer(1).rowsPerFrame = 2048*(P.numFrames);
Resource.RcvBuffer(1).colsPerFrame = ...
    Resource.Parameters.numTransmit;
Resource.RcvBuffer(1).numFrames = 1;

% Specify Transmit waveform structure.
TW(1).type = 'parametric';
TW(1).Parameters = [Trans.frequency,0.67,2,1];

% Specify TX structure array.
TX = struct('waveform', 1, ...
```

```
                    'Origin', [0.0,0.0,0.0], ...
                    'focus', 0.0, ...
                    'Steer', [0.0,0.0], ...
                    'Apod', ones(1,128), ...
                    'Delay', zeros(1,Trans.numelements));

% Specify TGC Waveform structure.
TGC(1).CntrlPts = [0,590,650,710,770,830,890,950];
TGC(1).rangeMax = P.endDepth;
TGC(1).Waveform = computeTGCWaveform(TGC);

% Specify Receive structure array
Receive = repmat(struct(...
                'Apod', [zeros(1,64),ones(1,64)], ...
                'startDepth', P.startDepth, ...
                'endDepth', P.endDepth, ...
                'TGC', 1, ...
                'mode', 0, ...
                'bufnum', 1, ...
                'framenum', 1, ...
                'acqNum', 1, ...
                'sampleMode', 'custom',...
                'decimSampleRate', P.sampleRate) ...
                ,1,P.numFrame);

%-- Set event specific Receive attributes.
for i = 1:P.numFrames
    Receive(i).acqNum = i;
end
```

```
% Specify an external processing event.
Process(1).classname = 'External';
Process(1).method = 'FastUltrasoundRF_process';
Process(1).Parameters = {'srcbuffer','receive',...
                         'srcbufnum',1,...
                         'srcframenum',-1,...
                         'dstbuffer','none'};

% Specify sequence events.
SeqControl(1).command = 'triggerIn';
SeqControl(1).condition = 'Trigger_1_Rising';
SeqControl(1).argument = 0; % time im usec
SeqControl(2).command = 'jump';
SeqControl(2).argument = 1;

k_sc = 3;
k = 1;   % start index for Events

Event(k).info = 'Waiting fot the trigger-in signal.';
Event(k).tx = 0;
Event(k).rcv = 0;
Event(k).recon = 0;
Event(k).process = 0;
Event(k).seqControl = 1;
 k = k+1;

for i = 1:P.numFrames
    Event(k).info = 'Aquisition RF';
```

```
        Event(k).tx = 1;
        Event(k).rcv = i;
        Event(k).recon = 0;
        Event(k).process = 0;
        Event(k).seqControl = 0;
         k = k+1;
    end

    Event(n-1).seqControl = [2,k_sc];
    SeqControl(k_sc).command = 'transferToHost';
    k_sc = k_sc+1;

    Event(k).info = 'Call external Processing function.';
    Event(k).tx = 0;
    Event(k).rcv = 0;
    Event(k).recon = 0;
    Event(k).process = 1;
    Event(k).seqControl = 0;
    k = k+1;

    Event(k).info = 'jump  back to event 1';
    Event(k).tx = 0;
    Event(k).rcv = 0;
    Event(k).recon = 0;
    Event(k).process = 0;
    Event(k).seqControl = 2;

    %- Create UI controls for channel selection/
    nr = Resource.Parameters.numRcvChannels;
```

```
UI(1).Control = {'UserB1','Style','VsSlider',...
                 'Label','Plot Channel',...
                 'SliderMinMaxVal',[1,128,64],...
                 'SliderStep', [1/nr,8/nr],...
                 'ValueFormat', '%3.0f'};
UI(1).Callback = {'assignin(''base'',''myPlotChnl'',...
round(UIValue));'};
EF(1).Function = vsv.seq.function.ExFunctionDef...
('FastUltrasoundRF_process',@FastUltrasoundRF);
% Save all the structures to a .mat file.
save('../../MatFiles/FastUltrasoundRF_recording');
return

function FastUltrasoundRF(RData)

    % LOADING DATA
    Receive = evalin('base','Receive');
    Trans = evalin('base','Trans');
    P = evalin('base','P');
    TX = evalin('base','TX');

    save('FastUltrasoundRF_folder/RData.mat','RData');
    save('FastUltrasoundRF_folder/Receive.mat','Receive');
    save('FastUltrasoundRF_folder/Trans.mat','Trans');
    save('FastUltrasoundRF_folder/TX.mat','TX');
    save('FastUltrasoundRF_folder/P.mat','P');

end
```

Listing A.1: Fast RF recording MATLAB Code for Verasonics